Finite Element Analysis of Embankment Dam due to Rapid Drawdown Events

by

Michael Steven Archard

B.S. Civil and Environmental Engineering (2012)
Northeastern University, Boston MA

Submitted to the Department of Civil and Environmental Engineering in partial fulfillment of the requirements for the degree of

Master of Engineering in Civil and Environmental Engineering
at the
MASSACHUSETTS INSTITUTE OF TECHNOLOGY

June 2016

Signature redacted

Signature of Author: _____
Department of Civil and Environmental Engineering
May 18, 2016

Signature redacted

Certified by: _____
Andrew J. Whittle
Edmund K. Turner Professor of Civil and Environmental Engineering
Thesis Supervisor

Signature redacted

Accepted by: _____
Heidi M. Nepf
Donald and Martha Harleman Professor of Civil and Environmental Engineering
Chair, Departmental Committee for Graduate Students

Finite Element Analysis of Embankment Dam due to Rapid Drawdown Events

by

Michael Steven Archard

Submitted to the Department of Civil and Environmental Engineering
on May 18, 2016 in Partial Fulfillment of the Requirements for the Degree of
Master of Engineering in Civil and Environmental Engineering

Abstract

The stability of large earth embankment dams is imperative for public safety and economic reasons. Among the numerous potential failure modes (which range from internal erosion to overtopping) slope instabilities can be triggered by changing boundary conditions associated with flood loading or rapid drawdown (RDD) conditions.

The assessment of slope stability under RDD conditions is difficult to estimate due to the time-dependence of pore pressures within the dam and uncertainties in the shear strength properties of compacted fills. Computational analysis tools such as non-linear finite element methods allow for more comprehensive analyses than can be accomplished by conventional steady seepage and limit equilibrium methods and enable more detailed investigations of the underlying material properties and boundary conditions affecting earth dam performance. This thesis describes the use of finite element (FE) analyses to evaluate the effects of rapid drawdown on slope stability for a large, earth embankment dam, 'CV dam', located in Central New York State that was constructed in the 1960s. Hydraulic properties of the embankment fill are evaluated by fitting measurements of pore pressures inside the dam with 2-D steady seepage using the PLAXIS 2D 2015™ finite element program. Using these calibrated properties, slope stability is computed using the same program through the method of c-phi reduction using undrained and transient pore pressure conditions for a range of reservoir drawdown events.

The results show how stability of the upstream slope can be related to the time-dependent drawdown of the reservoir. Instantaneous undrained drawdown generates the lowest factors of safety, while transient analyses provide a more realistic estimate of the operative factor of safety. The results confirm that there is adequate safety against slope stability for the full range of proposed drawdown events in the reservoir.

Thesis Supervisor: Andrew J. Whittle
Title: Edmund K. Turner Professor in Civil Engineering

Acknowledgements

First and foremost, I would like to thank my advisor, Professor Andrew J. Whittle. This thesis would not have been possible without his patient guidance and willingness to see where the road leads. I am lucky to have studied under such a knowledgeable and experienced instructor.

I would also like to thank Professor Herbert H. Einstein for his insight and wisdom throughout the year.

Thank you to Zhandos Orazalin, Eva Ieronymaki and Mauro Sottile for their assistance with Plaxis. Many hours were saved because of their willingness to help.

Thank you to Spyros Zervos, Quincy Pratt and Rafael Villamor Lora for your assistance and comradery throughout the school year.

Thank you to my coworkers and managers at GZA, especially: Bill Hover, Brad Nourse and John DeLano, for helping me obtain the necessary information for my research and answering numerous questions.

A special thanks goes to my family for their support throughout my graduate studies, especially my mother Kate and sister Jacki for their editorial expertise.

I owe a huge thanks to my dearest Rachelle, for keeping me focused through all of my deadlines and putting up with my wacky study habits. I couldn't have done this without you.

I could not conclude without thanking my grandfather, William Zoino. His charisma and predisposition to teach led me to the field of Civil Engineering and MIT. He bestowed upon me from a very early age the importance of education and hard work.

Table of Contents

List of Figures

List of Tables

1.0 Introduction

1.1 Problem Statement

Slope stability of large earth embankment dams is imperative for public safety and economic reasons. State and Federal regulations are in place that require periodic evaluation of these structures depending on size and hazard classification. Catastrophic failure of a large embankment that actively impounds water can threaten the immediate safety of those downstream, and affect populations that rely on the water supplied from the reservoir or hydro-electric power generated. In the United States, water-retaining embankments that are classified, by state and federal agencies, as "High" hazard are the highest risk to society and must be evaluated each year. Federal regulations are set forth by the U.S. Army Corps of Engineers (USACE, 2014) and U.S. Bureau of Reclamation. State agencies, such as the Massachusetts Office of Dam Safety, regulate nonfederal structures. A national group, the Association of State Dam Safety Officials (ASDSO), was formed in 1983 to educate and raise awareness with respect to safety of state and privately-owned dams (ASDSO, 2016).

Two main mechanisms that can cause slope stability failures in embankments are flood loading and rapid drawdown (see Figure 1.1). Both failure mechanisms impose a change in boundary condition on the embankment (VandenBerge et al., 2013). Slope failure due to flood loading occurs when the impounded water level increases to an elevation where the increased stresses and seepage within the dam can reduce the stability and induce failure mechanisms on the downstream slope of the dam. Rapid drawdown (RDD) failure occurs when the pool level in the reservoir is lowered, removing the stabilizing hydrostatic pressure along the slope while simultaneously decreasing stresses on the upstream slope, thereby reducing stability of the upstream slope that can potentially cause instability.

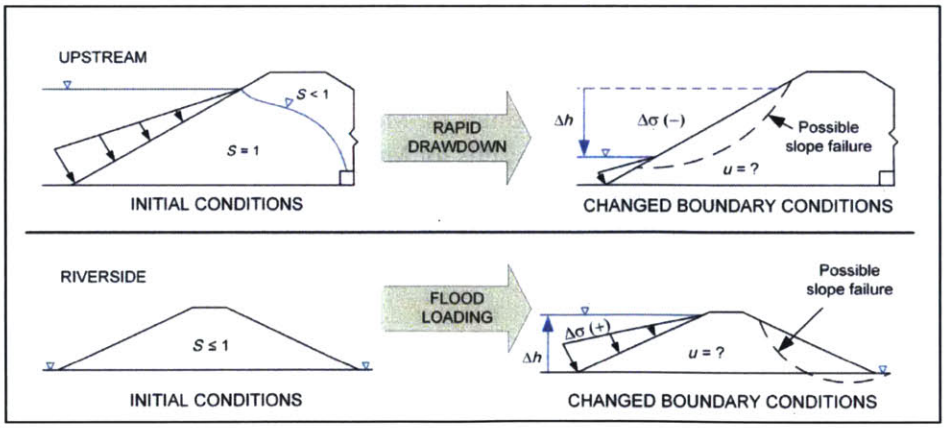

Figure 1.1: Rapid Drawdown and Flood Loading failure mechanisms (VandenBerge et al., 2015).

Stability under RDD conditions is difficult to estimate due to the time-dependence of pore pressures and effective stresses occurring within the compacted fill layers; this is further compounded by the complexities associated with partially-saturated soil behavior. Modern analysis tools such as the Finite Element (FE) method allow for more comprehensive analyses than can be accomplished by conventional limit equilibrium methods (VandenBerge et al., 2013). Finite element methods also enable more detailed investigations of the underlying material properties and boundary conditions affecting earth dam performance.

1.2 Scope and Objectives

The goal of this research is to analyze the stability of an earth embankment dam under rapid drawdown (RDD) conditions using the capabilities of a commercial finite element program, PLAXIS 2D 2015™ (Plaxis, 2015). This goal is achieved in the context of the evaluation of a large, zoned earth embankment dam, referred to as the CV dam, located in central New York state that was built in 1964. A finite element model is calibrated to the steady seepage conditions observed in the dam and is then used to investigate how stability is affected by time-dependent drawdown of the reservoir. The main tasks involved in this research are as follows:

1. Literature Review: The goal of the literature review was to learn about past RDD failures and discover how researchers and practitioners evaluate transient seepage and slope stability in the context of rapid drawdown.
2. Create a calibrated FE model for the CV dam: Using the available data, we create a finite element model of a large embankment dam and calibrate hydraulic properties for steady-state seepage conditions based on observed piezometric data within the CV dam from November 2014 to February 2016.
3. Undrained Stability Model: Using the calibrated FE model, we evaluate the effects of instantaneous drawdown to selected pool elevations on undrained stability of the embankment dam. This is achieved using shear strength reduction analyses (c-phi method; Brinkgreve and Bakker, 1991) to estimate the factor of safety for slope stability.
4. Transient Stability Model: Using the calibrated FE model, we demonstrate the time-dependent drawdown effect on slope stability, for selected reservoir pool elevations with partial drainage (transient seepage conditions). These analyses assume that the shear strength of the fill materials is controlled by effective stresses with the Mohr-Coulomb strength criteria.

5. Future Research: We provide recommendations for future research associated with the use of FE software to simulate rapid drawdown behavior of earth embankment structures.

1.3 Organization of Thesis

This thesis is separated into six chapters with additional discussion and further detail below.

Chapter 2 provides a literature review of previous rapid drawdown failures as well as a discussion of the current methods to model slope stability of embankment structures under RDD conditions.

Chapter 3 gives the background for evaluation of the proposed embankment dam. This includes a history of the dam as well as a discussion of available data to be used in the FE model. The chapter also discusses recent seepage events at the dam and corresponding data showing conditions before, during, and after completion of repairs.

Chapter 4 describes the construction of the PLAXIS 2D 2015™ (Plaxis, 2015) FE model. This includes the selection of input parameters based on the interpretation of available data and the assembly of the model, including model simplifications.

Chapter 5 discusses the results of the analysis specifically related to the steady-state model calibration, undrained analysis, and transient analysis. The discussion includes expected results and interpretations of drawdown rates to ensure stability against slope failures.

Chapter 6 summarizes the findings of the thesis and outlines recommendations for further study related to FE analysis of RDD in the context of PLAXIS 2D 2015™.

2.0 Literature Review

2.1 Rapid Drawdown Failures

Failures of embankment dams are statistically rare events but have occurred throughout history with varying levels of consequences. The ASDSO database lists 194 complete dam failures in the United States prior to 2011 and quotes several hundred "incidents" where dam failure was averted through interventions (ASDSO, 2016). Slope failures can range from local sloughing to catastrophic collapse and release of impounded water. Dam failures can be caused by various mechanisms including poor construction, inadequate spillway capacity, geologic instability, internal erosion, etc. Whitman (2000) organizes and evaluates risk associated with geotechnical engineering projects (Figure 2.1) showing dam failures as the lowest annual probability event, but among the highest consequences of failure. One of the lesser-known failure mechanisms, making up a small subset of the total historic dam failures, is that of rapid drawdown slope failure. Only one dam failure, Bouldin Dam, included in the ASDSO database is attributed to rapid drawdown (ASDSO, 2016).

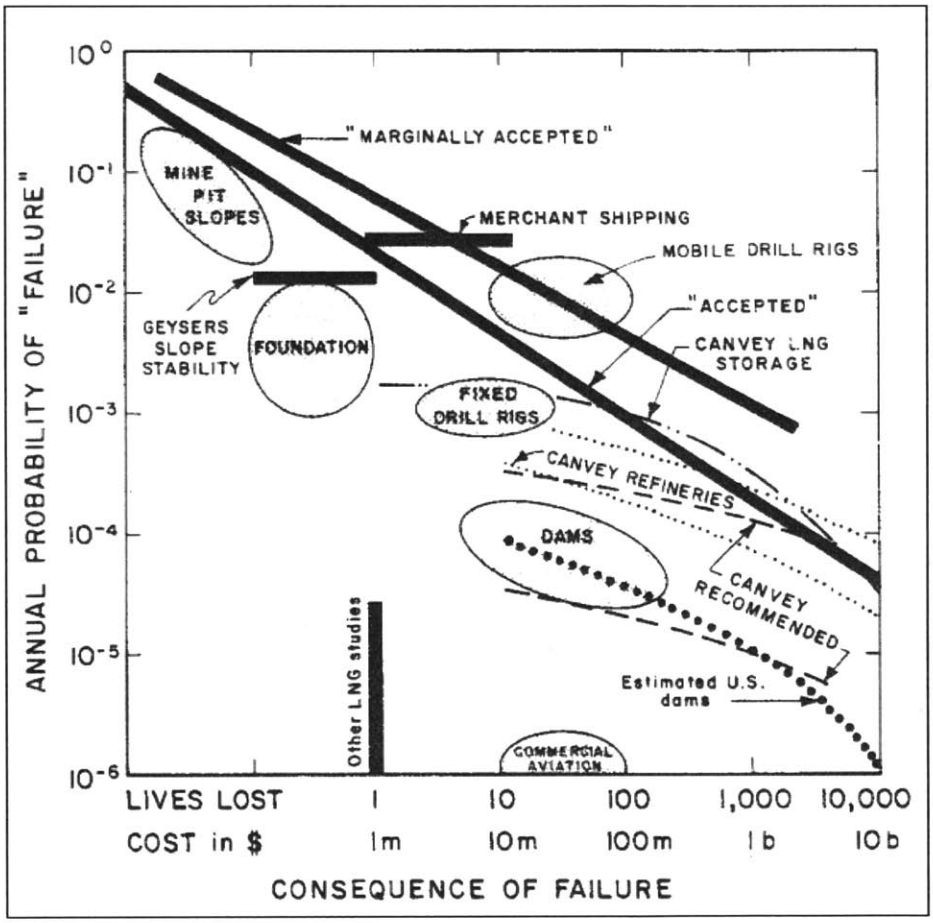

Figure 2.1: Risk for geotechnical engineering projects (Whitman, 2000).

Of the past RDD dam failures, perhaps the most studied is the 1969 slope failure of the Pilarcitos Dam. The Pilarcitos Dam, built in 1864 in California's San Francisco Peninsula, is a 78-foot high homogeneous compacted rolled earth embankment dam comprised of sandy-clay. The dam experienced a slope failure along the upstream slope a few days after the reservoir level dropped 35 feet over a period of 43 days. While this slope failure did not lead to catastrophic failure, it serves as a reminder that RDD failure can occur under normal operating and/or maintenance conditions.

VandenBerge (2014) attempts to simulate the failure of Pilarcitos Dam using finite element analyses and c-phi reduction with total stress (undrained, s_u) strength parameters. Figure 2.2 shows the approximate observed failure surface, element displacement vectors from VandenBerge (2014), and the failure surface from a study by Duncan et al. (1990). The displacement vectors from the finite element analysis show a relatively deep failure zone that intersects the base of the embankment, indicated by the red line in Figure 2.2. This modeled failure zone is much longer and deeper than what was observed.

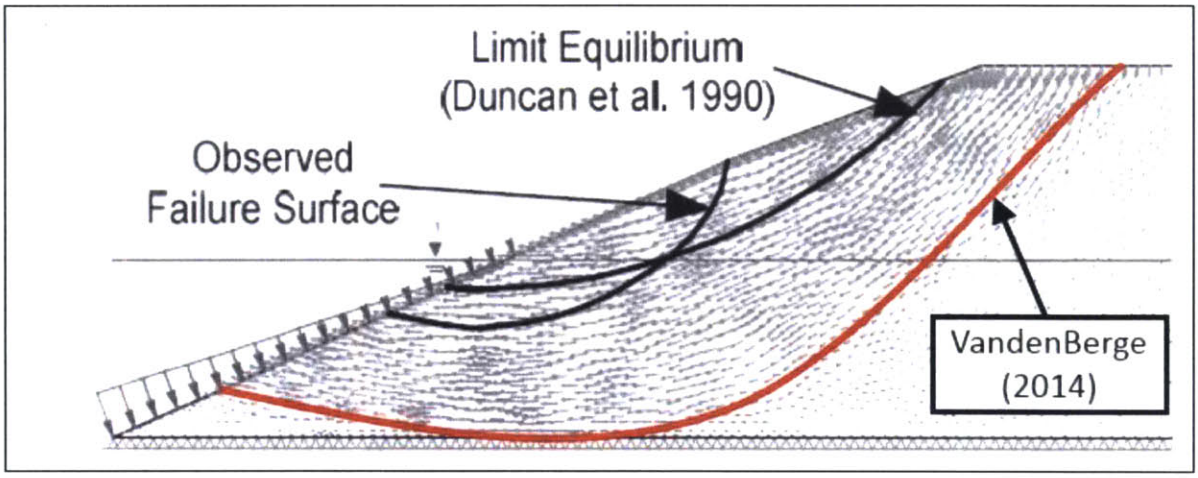

Figure 2.2: Modeled and observed failure surfaces of Pilarcitos Dam from VandenBerge (2014).

Another notable dam failure related to rapid water level decrease occurred at the Walter Bouldin Dam in 1975. Walter Bouldin Dam (Bouldin Dam) is an earth embankment hydropower dam located in Elmore County, Alabama. Bouldin Dam was built in 1967 and consists of compacted earth fill with an upstream impervious layer along the upstream slope. The dam actually experienced RDD slope failure twice in three years.

The first failure occurred after an extended period of full-load hydropower generation in 1972. The reservoir experienced a drawdown of 10 feet in seven hours, causing an upstream slope failure.

Luckily the slope failure did not result in a release of water and was repaired by hand-tamping clay and placing additional erosion protection along the failure area.

VandenBerge (2014) re-interpreted the failure of Bouldin Dam using finite element analyses and c-phi reduction with total stress (undrained, s_u) strength parameters. Figure 2.3 shows the approximate observed failure surface, element displacement vectors from VandenBerge (2014), and the failure surface from a study by Duncan et al. (1990). The failure surface from the finite element analysis, indicated by the red line in Figure 2.3, shows good agreement with Duncan et al. (1990) but is much deeper and longer than what was observed, suggesting limitations in the interpretation of soil properties, pore pressures or method of analysis.

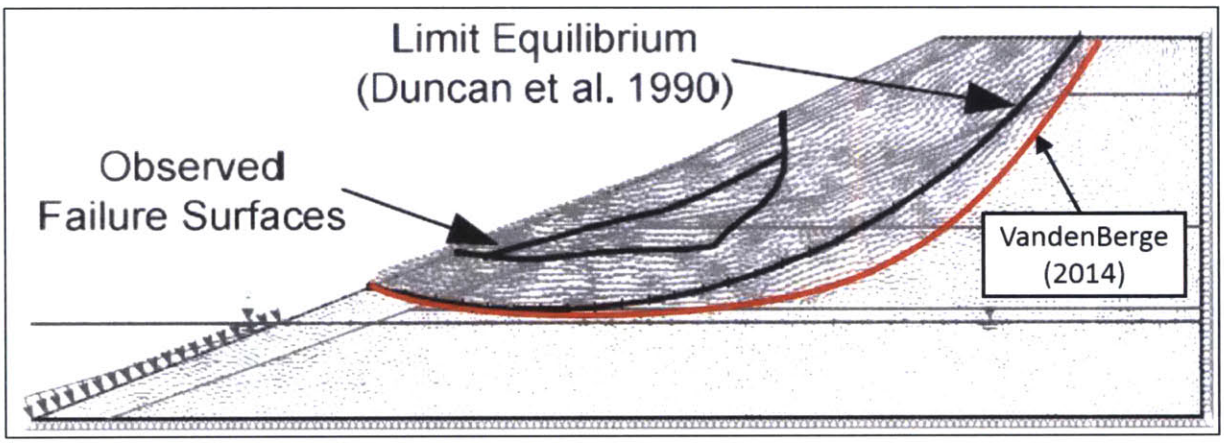

Figure 2.3: Modeled and observed failure surfaces of Bouldin Dam from VandenBerge (2014).

Three years later, a sudden dam breach failure occurred, resulting in a complete release of the almost 250,000-acre-foot (80-billion gallon) impoundment. Shortly after this catastrophic release, which caused a drawdown of 32 feet in five hours, several additional slope failures occurred including two upstream RDD failures. The United States Federal Energy Regulatory Council (FERC, 1978), owner and operator of the dam, issued a full investigation to assess the failure of the dam, and completed a full redesign and reconstruction (see Figure 2.4 below for a summary of failure areas from the FERC investigation report). The catastrophic failure in 1975 has been attributed to poor construction techniques and the improper repair of the of the 1972 slide (FERC, 1978). Bouldin Dam was reconstructed in 1979 and is still in operation today.

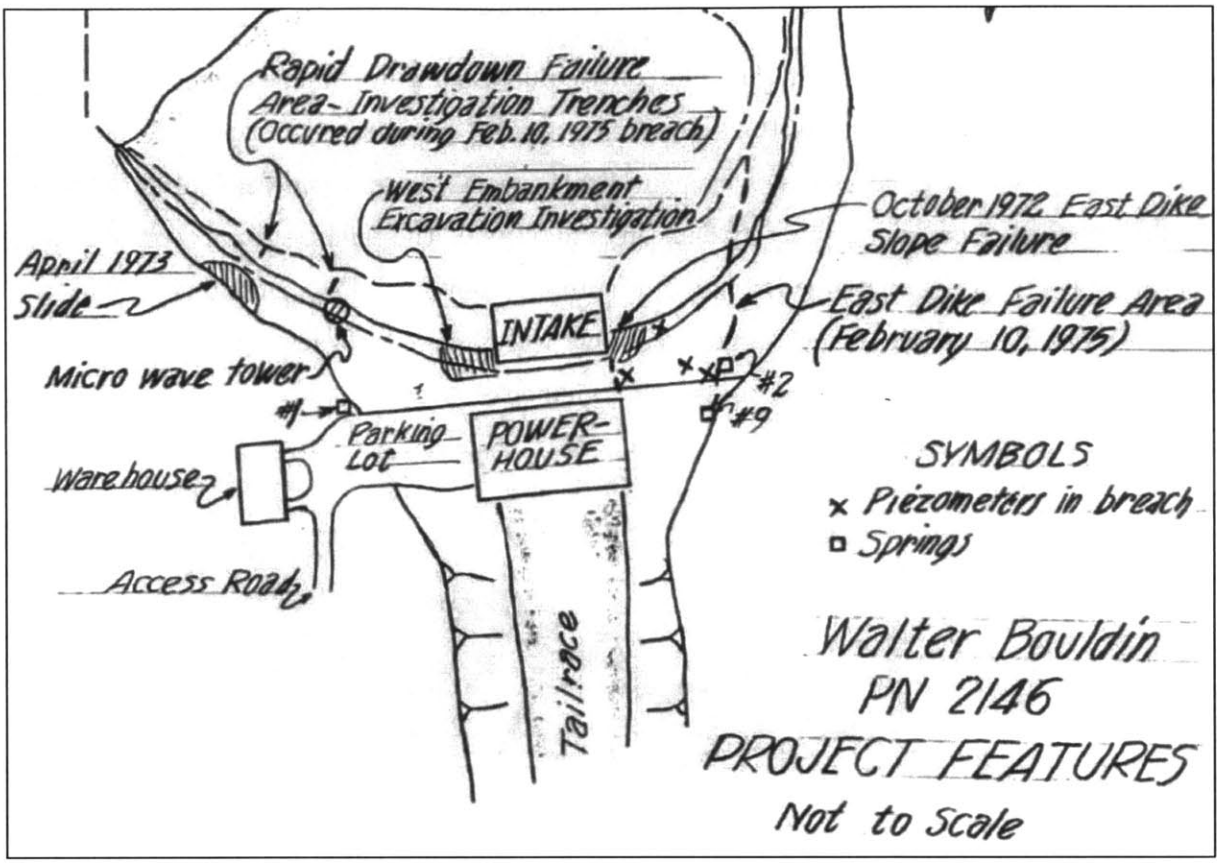

Figure 2.4: Bouldin Dam plan view sketch of failure areas (FERC, 1978).

2.2 Analysis of Slope Instability for Rapid Drawdown Conditions

Morgenstern (1963) presented stability charts for evaluating slope stability due to rapid drawdown events. The charts assume undrained conditions within the dam (effectively treating the case of instantaneous drawdown) and estimate the average excess pore pressure within the dam using the Skempton $\bar{B}$ method. A more detailed description of this methodology is included in Section 2.2.1. Also included in this paper is a detailed table compiling historic RDD dam failures from the 19th and 20th centuries. This table, shown below as Table 2.1, lists a number of slope failures attributed drawdown conditions. Note the units of c' are in pounds per square inch. With the 16 dams listed and two discussed above, RDD stability is a critical mechanism to investigate.

Table 2.1: Rapid drawdown failures prior to 1963 (Morgenstern, 1963)

Name	Height: (ft)	Upstream slope	Soil properties c' (psi)	Notes and references
Cercey	37·7	2·4 : 1	$c' = 2{\cdot}6$ per sq. in. $\phi' = 26°$	Drained shear box tests carried out many years after failure, Mayer (1936)
Wassy	54·0	1·5 : 1	$c' = 2{\cdot}8$ per sq. in. $\phi' = 23°$	do.
Grosbois	57·0	1·9 : 1	$c' = 3{\cdot}6$ per sq. in. $\phi' = 25{\cdot}7°$	do.
Charmes	55·7	1·9 : 1	$c' = 4{\cdot}1$ per sq. in. $\phi' = 26{\cdot}6°$	do.
Bear Gulch	63·0	3 : 1	—	Sherard (1953)
Belle Fourche ..	122·0	2 : 1	$c = 7{\cdot}9$ per sq. in. $\phi = 9{\cdot}7°$	Undrained direct shear tests after failure, Sherard (1953)
Brush Hollow ..	73·0	3 : 1	$c_u = 13{\cdot}5$–$28{\cdot}4$ per sq. in.	Unconfined compression tests after failure, Sherard (1953)
Mount Pisgah ..	76·0	1·5 : 1	—	Sherard (1953)
Utica	70·0	2 : 1	—	Reinius (1948)
Eildon	90·0	1·35 : 1	—	Schatz and Boesten (1936)
Aiai-ike	42·5	1 : 1–2 : 1	$c' = 1{\cdot}5$ per sq. in. $\phi' = 18°$	Consolidated undrained triaxial tests, Akai (1958)
Fruitgrower's ..	36·0	3 : 1	—	Sherard (1953)
Forsyth	65·0	2 : 1	—	Sherard (1953)
Standley Lake ..	113·0	2 : 1	—	Sherard (1953)
Willingdon	55·0	2 : 1	—	Rao (1961)
Palakmati	46·0	2 : 1–3 : 1	—	Rao (1961)

The undrained stability of an earth slope can be evaluated using either total stress (i.e., undrained shear strength, s_u) or effective stress (c', φ') strength parameters. Effective stress (drained) parameters are often used for RDD calculations as they can account directly for partial drainage (transient seepage) within the fill materials. Undrained stability is generally a more stringent stability estimate than transient analyses which consider the partial dissipation of pore pressures within the dam. In reality, drawdown of the reservoir causes time-dependent effective stresses and pore pressures, while the shear strength of the clay may also be affected by conditions at points above the steady state phreatic surface (e.g., matric suction above the water table).

Current methods to estimate changes in pore water pressure during RDD conditions can be organized into three groups:

1. $\bar{B}$ Methods
2. Uncoupled Seepage Methods
3. Coupled Seepage Methods

For the purposes of this thesis, coupled seepage methods refer to all analyses where effective stresses control soil strength coupled with the changes in hydraulic boundary conditions. Uncoupled methods are those that only consider the changes in hydraulic boundary conditions and assume total stress strength parameters.

2.2.1 $\bar{B}$ Method

Bishop (1954) applied the pore pressure parameter methods (Skempton, 1954) to estimate changes in pore pressures during RDD. This resulting $\bar{B}$ Method, relates the change in pore pressures to the change in major principal stress within an embankment. The change in major principal stress is often evaluated with the change in vertical total stress caused by the change in pool water elevation above a chosen point, Δh_w:

$$\Delta u = \bar{B}\Delta\sigma_1 \qquad (2.1)$$

$$\Delta u = -\gamma_w \Delta h_w \bar{B} \qquad (2.2)$$

The value of the pore-pressure ratio, $\bar{B}$, will affect the magnitude of pore pressure after RDD and subsequently the factor of safety of the upstream slope. The lower the value of $\bar{B}$ the lower the factor of safety. The value of $\bar{B}$ can be estimated from triaxial tests in which the reduction of the major principal stresses during drawdown is simulated (Morgenstern, 1963). The equation for $\bar{B}$, as defined by Skempton (1954), is defined below in terms of Skempton's pore pressure parameters A and B:

$$\bar{B} = B[1 - (1 - A)\left(1 - \frac{\Delta\sigma_3}{\Delta\sigma_1}\right)] \qquad (2.3)$$

Where B = 1 for saturated soils, while A varies with stress history and shear strain level. This simplified analysis does not consider time-dependency associated with RDD, rather the drawdown is assumed to be instantaneous with undrained shear conditions in the embankment fill. This method is intended to be a conservative upper bound method for estimating changes in pore pressure due to RDD and neglects the shear strength gained above the phreatic surface from matric suction (i.e., capillarity) and the partial drainage that would occur due to time-dependent drawdown (VandenBerge et al., 2015).

Morgenstern (1963) constructed stability charts to aid in the process of estimating stability under RDD conditions. Morgenstern utilized the $\bar{B}$ Method to estimate the changes in pore pressure prior to estimating stability using the Bishop Method for various slope inclinations and cohesion values.

In his analysis, Morgenstern assumes the steady-state water level is at the top of the dam and undergoes instantaneous drawdown with $\bar{B} = 1$ as illustrated in Figure 2.5.

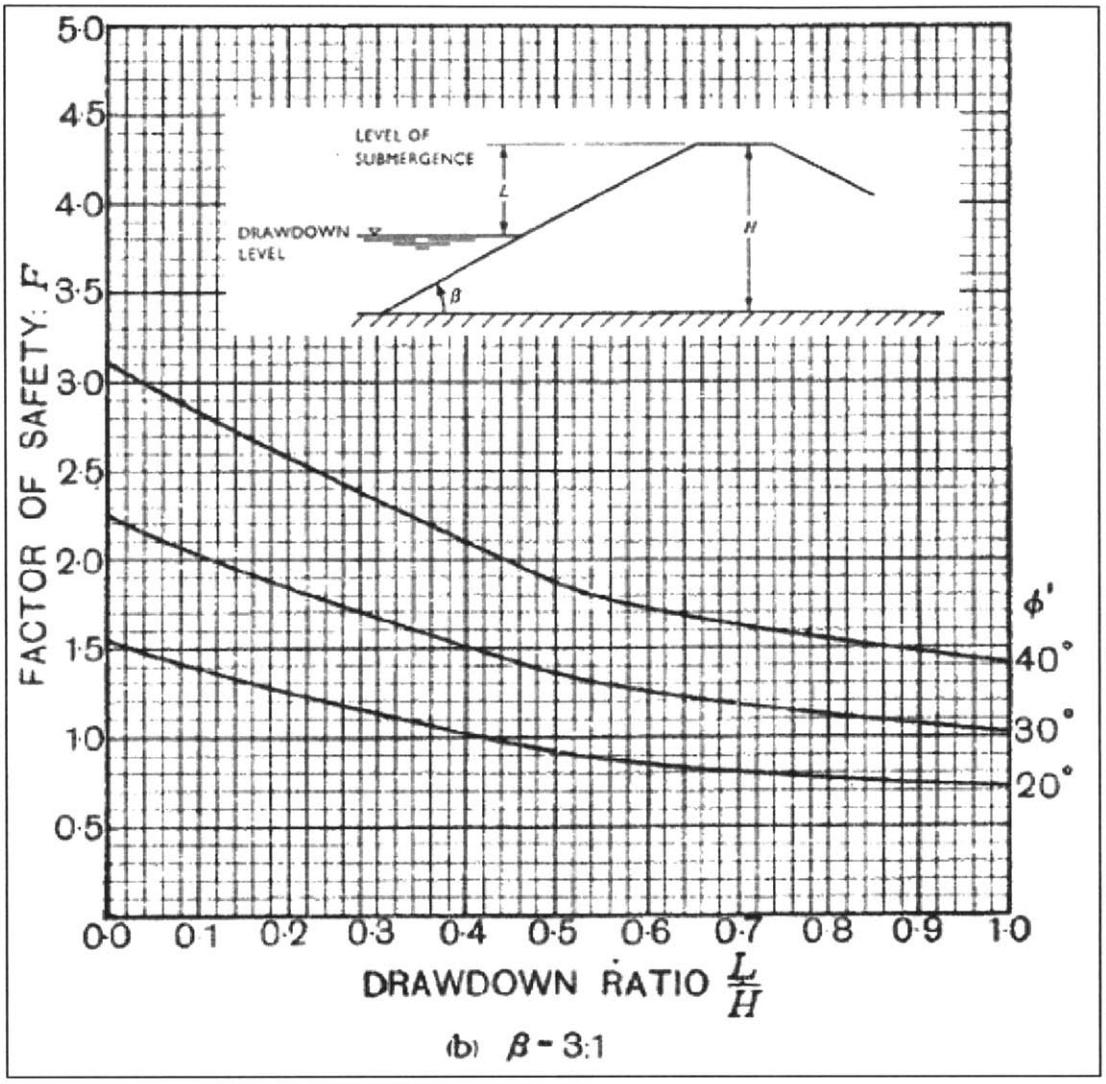

Figure 2.5: Stability chart for 3H:1V slope and $c'/\gamma h = 0.0125$ (Morgenstern, 1963).

2.2.2 Uncoupled Analyses

Today, a common approach to evaluate stability under RDD conditions utilizes uncoupled pore pressure response. This approach, which can use either total stress (undrained) or effective stress (drained) strength parameters, is considered uncoupled as it only considers the changes in pore pressures associated with the change in hydraulic boundary conditions from the removed water load on the slope. Current state of practice in engineering consulting utilizes software packages that use uncoupled seepage analyses and Limit Equilibrium Methods (LEM) to assess the factor

of safety for slope stability resulting from RDD. Government agencies, such as the USBR advocate the use of such software to analyze slope stability following RDD (VandenBerge et al., 2015).

2.2.3 Coupled Analyses

The coupled approach is the most representative of real conditions, yet is the most complex to model. In order to model the coupled behavior between the changes in pore pressure to the changes in total stress and soil compressibility, one has to simulate effective stress changes within the compacted earth fill. Models of the constitutive behavior may require numerous input parameters which are not always available in practice. Similar to uncoupled analyses, coupled analyses also utilize LEM to estimate the factor of safety for slope stability using the method of slices with procedures proposed by Bishop (1955) and Spencer (1967). Research by Berilgen (2007) and Pinyol et al. (2008) conclude that this coupled approach has dramatic effects on the calculated pore pressure response during RDD (VandenBerge et al., 2015).

Pinyol et al. (2008) analyzed an embankment dam, Shira Dam, using multiple coupled and uncoupled methods to estimate pore pressures during drawdown. Pore pressures were estimated at piezometer locations and compared to observed data (Figure 2.6). Results show that uncoupled analyses led to faster dissipation of pore pressures (thus higher factors of safety). Coupled methods gave a more realistic estimation of pore pressures during RDD events than uncoupled methods, however still be lead to faster pore pressure dissipation compared to observed data.

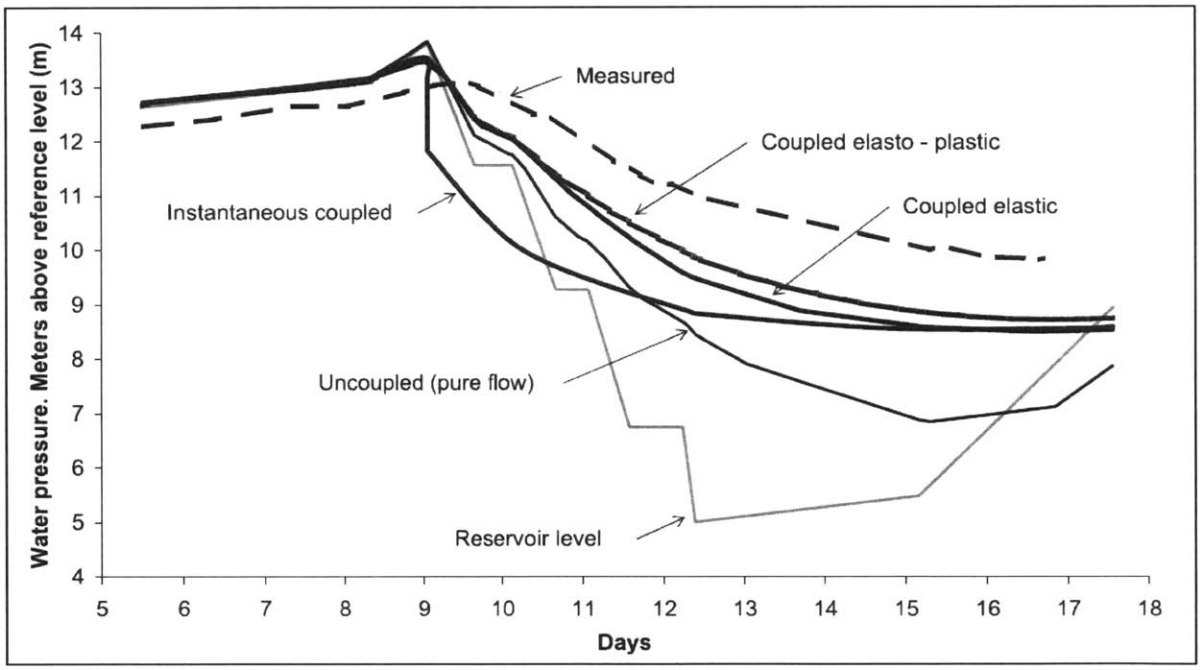

Figure 2.6: Calculated pore pressures vs time for coupled and uncoupled methods (Pinyol et al., 2008).

Berilgen (2007) analyzed a simple submerged slope with various coupled and uncoupled methods to estimate factors of safety during RDD events. Fully coupled methods included the use of various consolidation and deformation models to couple the pore pressure response with the changing stresses within the slope. Figure 2.7 shows the results of "only seepage pressure" (i.e., uncoupled) methods compared to the "seepage and stress induced pore pressure" (i.e., coupled) methods, for various levels of consolidation, T. Results show that the uncoupled methods consistently led to a higher safety factor compared to coupled methods. This is due to the faster dissipation of pore pressures that result from not coupling changes in pore pressures with changes in stress within the slope.

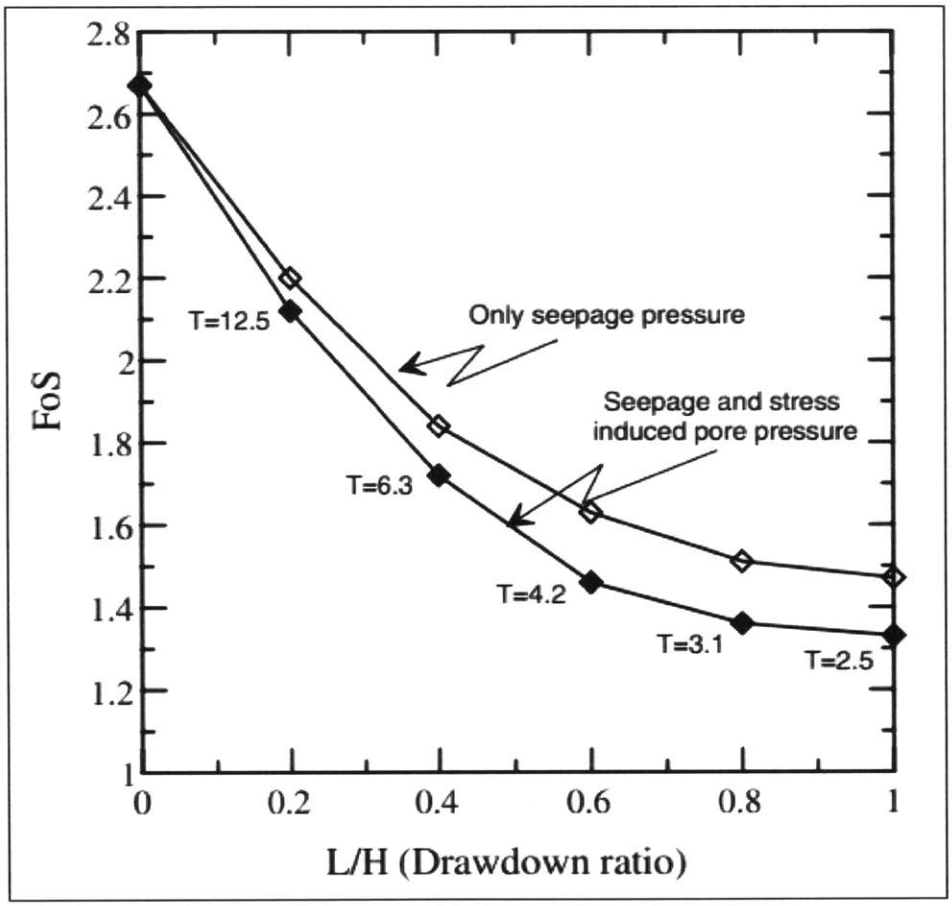

Note: $T = c_v t / (h_d)^2$

Figure 2.7: Estimated factors of safety for coupled and uncoupled methods (Berilgen, 2007).

3.0 Background

3.1 Site History

This chapter describes the geometry, fill properties and monitored performance of "CV dam" in New York State[1]. Most of the project-specific information included in this report was provided by GZA GeoEnvironmental, Inc. (GZA), the Dam owner's private consultant.

The CV dam was completed in 1964 and is a part of a system of dams and reservoirs in Central New York that supply almost 60% of the drinking water to the New York metropolitan area. It is a 175-ft high, 2,800-ft long, zoned earth embankment impounding approximately 300,000 acre-feet (95B gal.) of raw drinking water. Based on dam safety regulations set by New York Department of Environmental Conservation and guidelines set by the United States Army Corps of Engineers, CV dam is categorized by both agencies as a large, high hazard dam (GZA, 2005).

The CV dam, shown in Figure 3.1, features side slopes varying from 2H:1V to 3H:1V with benches at certain elevations along the downstream slope (Figure 3.2 and Figure 3.3). The embankment is comprised of an upstream "impervious" zone and a downstream "semi-pervious" zone of compacted fill. Riprap surface treatment is located along the upstream slope for protection against wave erosion and animal burrowing. Hydraulic controls include a stone masonry spillway structure consisting of an upper broad-crested weir and a lower ogee type weir providing a total discharge capacity of 250,000 ft^3/sec. The low-level outlet of the dam is located 151 feet below the spillway pool depth and represents the base of the reservoir, El. 999 ft NGVD. To divert water to a downstream reservoir, an intake chamber is located approximately 4 miles upstream of the dam and regulates flow into an 11 ft diameter, 44-mile-long concrete-lined, pressure tunnel with an approximate maximum capacity of 500MGD (GZA, 2005).

The performance of the dam is monitored through a system of instrumentation consisting of 12 vibrating wire piezometers and 16 groundwater observation wells within the embankment. Piezometric head values and reservoir elevation data are continuously monitored over time to aid in the evaluation of seepage and slope stability.

[1] Since 2001, the United States Department of Homeland Security has heightened its security measures on "Critical Infrastructure" by prohibiting detailed engineering information to be released for public infrastructure. In the United States, critical infrastructure is divided into 16 sectors, including energy, communications, transportation, dams, etc., and a national policy is established to identify and prioritize critical infrastructure and key resources and to protect them from terrorist attacks (Bush, 2003).

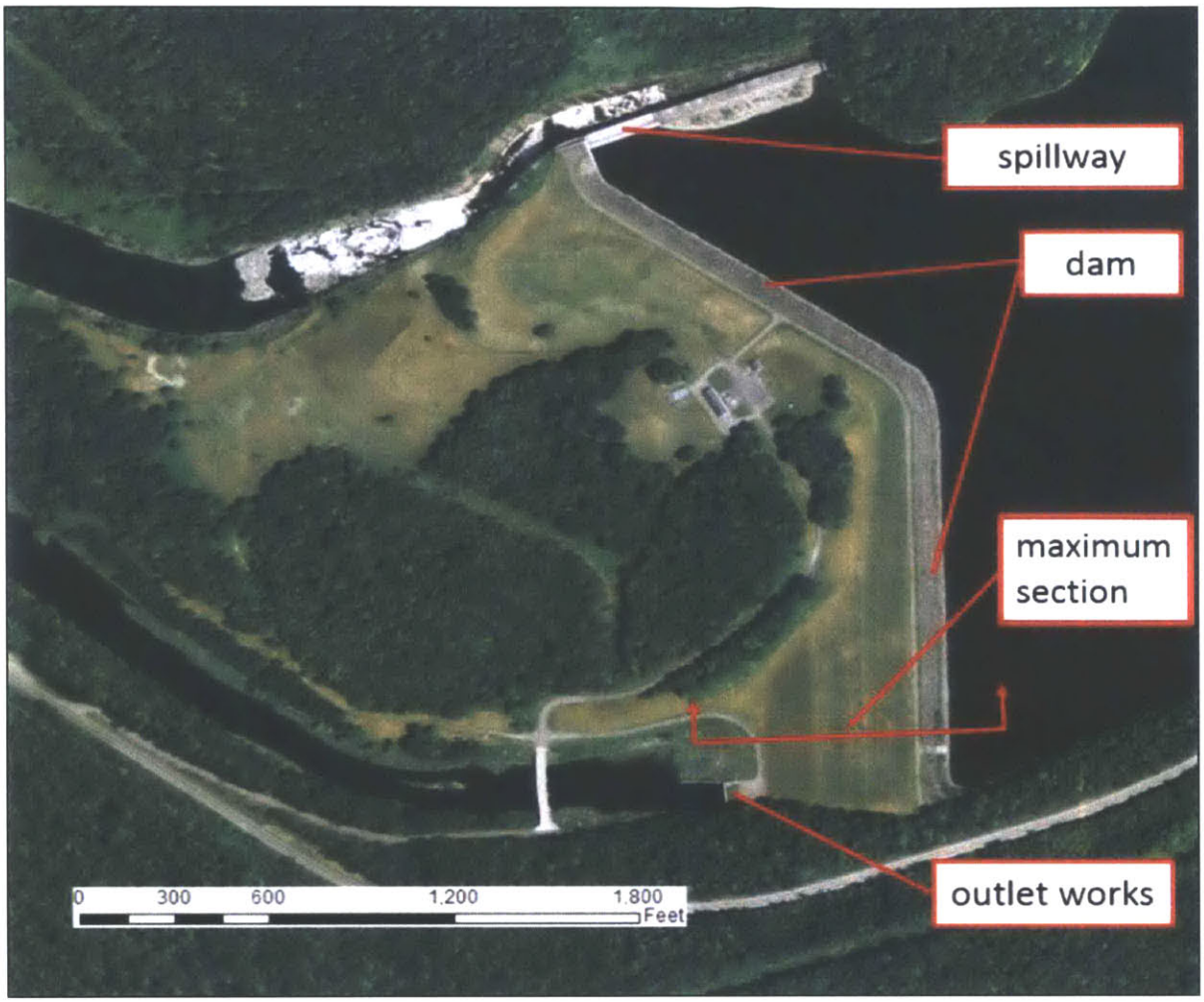

Figure 3.1: Aerial photo of CV dam and hydraulic structures.

3.2 Previous Investigations

In 1978, a Phase I Inspection Report was prepared by Robert L. Kimball and Associates under the National Dam Safety Program (NDSP) [2]. The report included recommendations for a review of soils and embankment stability, but the CV dam was considered to be in "excellent" condition. In 2005, GZA was hired by the owner to conduct a detailed study of the CV dam. The goal of the study was to assess its current condition and provide engineering services associated with bringing the CV dam and its facilities up to all federal and state dam safety recommendations and guidelines. The 2005 study included:

[2] President Carter established the NDSP in 1978 and appointed Frank E. Perkins of MIT as chairman following several tragic dam failures across the United States. The goal of the NDSP was to establish the framework to conduct periodic, nationwide inspections of non-federal High hazard dams to minimize the risk of future catastrophic dam failures.

- detailed physical inspections and records review for existing facilities;
- preparation of as-built topographic maps of CV dam site;
- geotechnical, structural, hydraulic, mechanical, and electrical engineering evaluations;
- subsurface explorations and installation of instrumentation;
- underwater inspection of associated inlet/outlet works;
- hydrologic/hydraulic evaluation of spillway capacities under the extreme events;
- reservoir dredging feasibility studies; and
- emergency action plans, CV dam breach modeling studies and inundation mapping.

Overall, based on the 2005 report, the CV dam was considered to be in "Good" condition and passed all recommended factors of safety related to slope stability (GZA, 2005). Specific details and results from the study relevant to this thesis are discussed in subsequent sections. GZA is currently working on an updated study of the CV dam to be finalized in 2016.

A review of geotechnical information was conducted based on the detailed study report completed for the CV dam, as well as other data obtained from the local consultant. This data included plan and profile information for the CV dam, geophysical data, instrumentation readings, soil properties including test data, boring logs etc.

Topographic and dimensional survey data is available for the CV dam. Topographic data was collected with a total station utilizing standard surveying practices. All referenced elevations correspond to the National Geodetic Vertical Datum of 1929 (NGVD 29). Figure 3.2 and Figure 3.3 show a local plan and section view of the CV dam at the maximum section reported by GZA (2005).

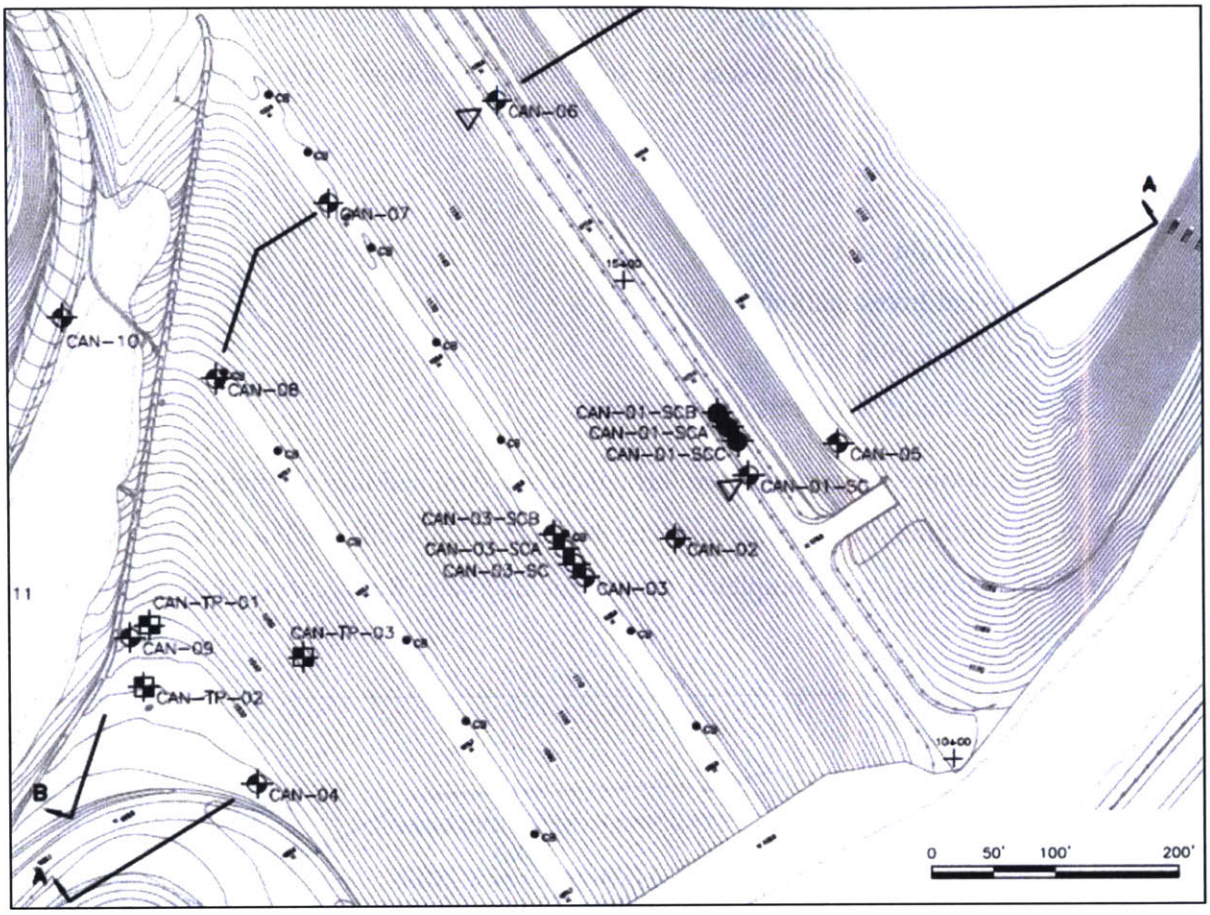

Figure 3.2: Plan view of CV dam at maximum section (A-A') showing boring locations (GZA, 2005).

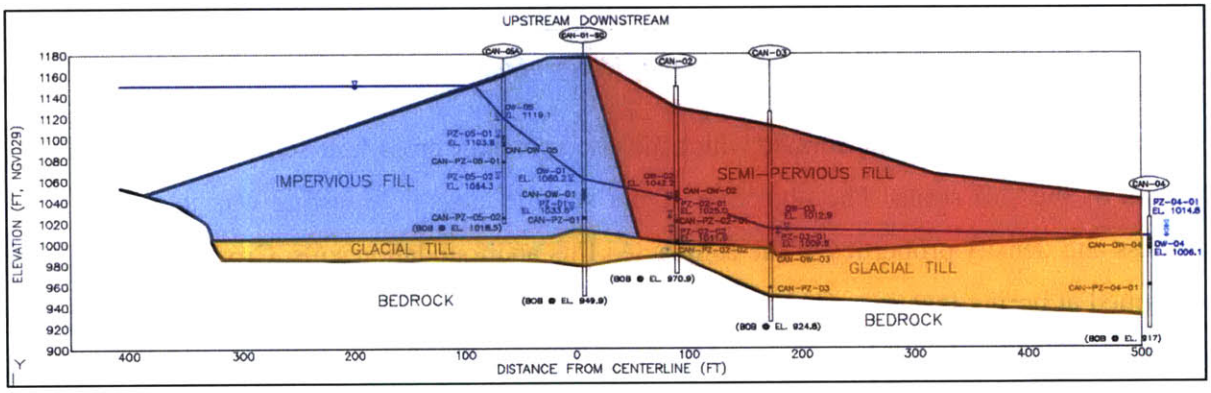

Figure 3.3: Maximum cross section of CV dam showing soil units and instrumentation.

3.2.1 Site Description and Materials

The CV dam was constructed in a narrow valley with dense, impervious glacial deposits and lake sediment deposits that overlay shale and quartz conglomerate bedrock, see Figure 3.4. The impervious upstream layer of the dam is keyed approximately 20 feet into the natural till layer (GZA, 2005).

During the 2005 detailed study of the CV dam, GZA conducted a subsurface exploration program to collect geotechnical data and assess the subsurface conditions. The exploration program included:

1. Test Borings
2. Instrumentation
3. Geophysical Investigations
4. In-Situ Permeability Testing
5. Dynamic Energy Transmission Testing

Twenty-three test borings were completed throughout the dam and instrumentation was installed consisting of 12 vibrating-wire piezometers and 16 observation wells. SPT tests were conducted and split-spoon sampling was completed at 10-foot intervals. Rock coring was conducted at selected borings.

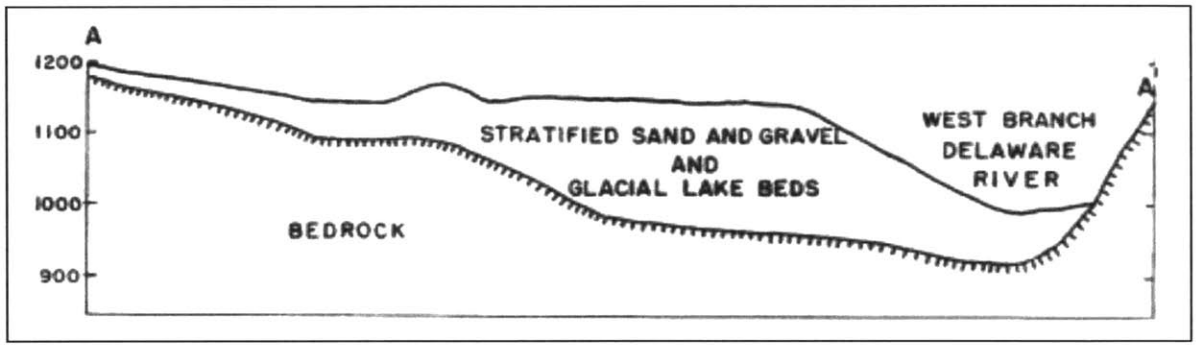

Figure 3.4: Local geology in the vicinity of the CV dam (USGS, 1963).

Geophysical surveys were performed which included borehole cross-hole seismic tests and camera surveys of the soil strata. The objective of the seismic cross-hole testing was to estimate the stiffness and density properties of the compacted fills and foundation soils. Cross-hole tests were performed at boring locations CAN-03 and CAN-01, shown on Figure 3.2. At each location, two test boreholes were located 15 feet and 30 feet, respectively, from the source borehole. Wave velocities were determined and are shown in comparison to SPT values in Figure 3.5 below (GZA, 2005).

Both soil penetration test (SPT) and shear wave velocity (v_s) data were measured and represent measurements of soil stiffness. Data for SPT is measured in blows per foot (N), a dynamic measurement that is loosely correlated to the shear strength. Figure 3.3 shows the shear wave

velocity and SPT-N values encountered in the upstream impervious fill material at boring CAN-01. Shear wave velocity is related to elastic shear modulus:

$$G = \rho v_s^2 \qquad (3.1)$$

The data show that SPT-N and v_s exhibit trends with depth from 0 to 150 feet before jumping to a constant value at a depth of 200 feet, when glacial till and bedrock is encountered. The data suggests SPT-N and v_s are approximately constant in the compacted fill and hence, the stiffness of the embankment fills are approximately constant with depth.

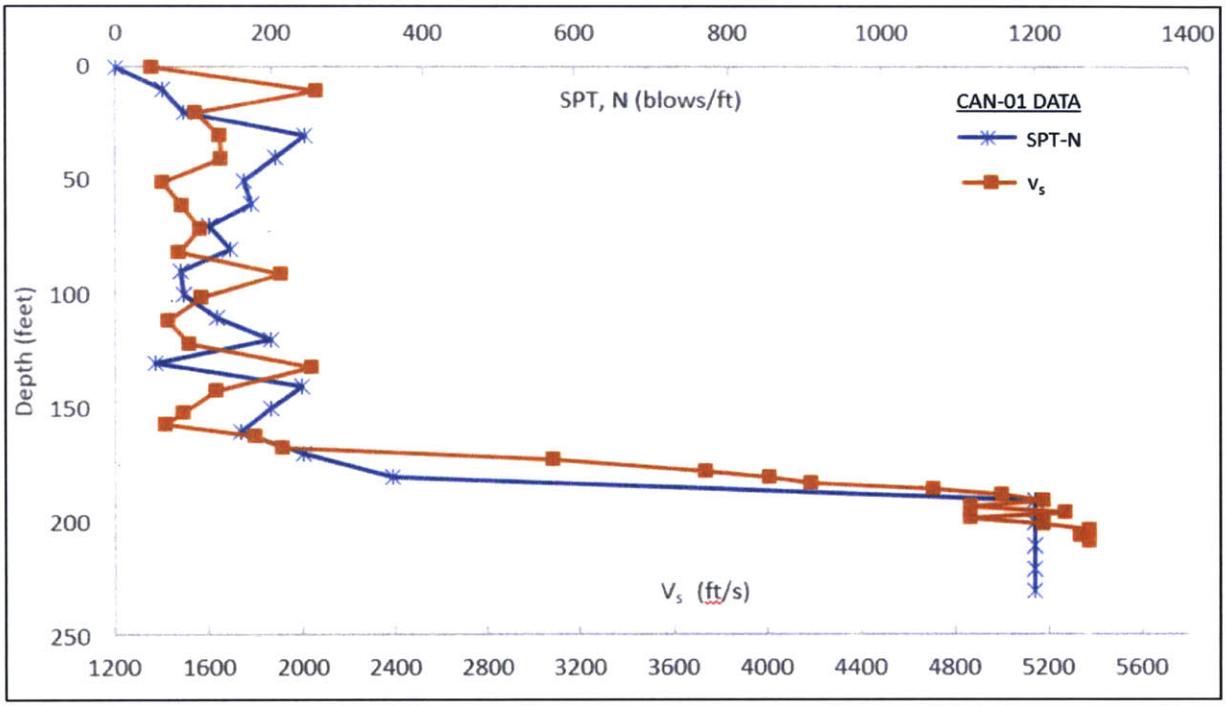

Figure 3.5: SPT-N and v_s versus depth at boring CAN-01.

In-situ permeability testing was conducted to estimate the hydraulic conductivity of the bedrock glacial till below the embankment soils and (Figure 3.3). No in-situ permeability testing was done for the impervious or semi-pervious fills. Three out of the five bedrock packer tests produced no flow. The results of the falling head permeability test for the glacial till are shown as Figure 3.6 below.

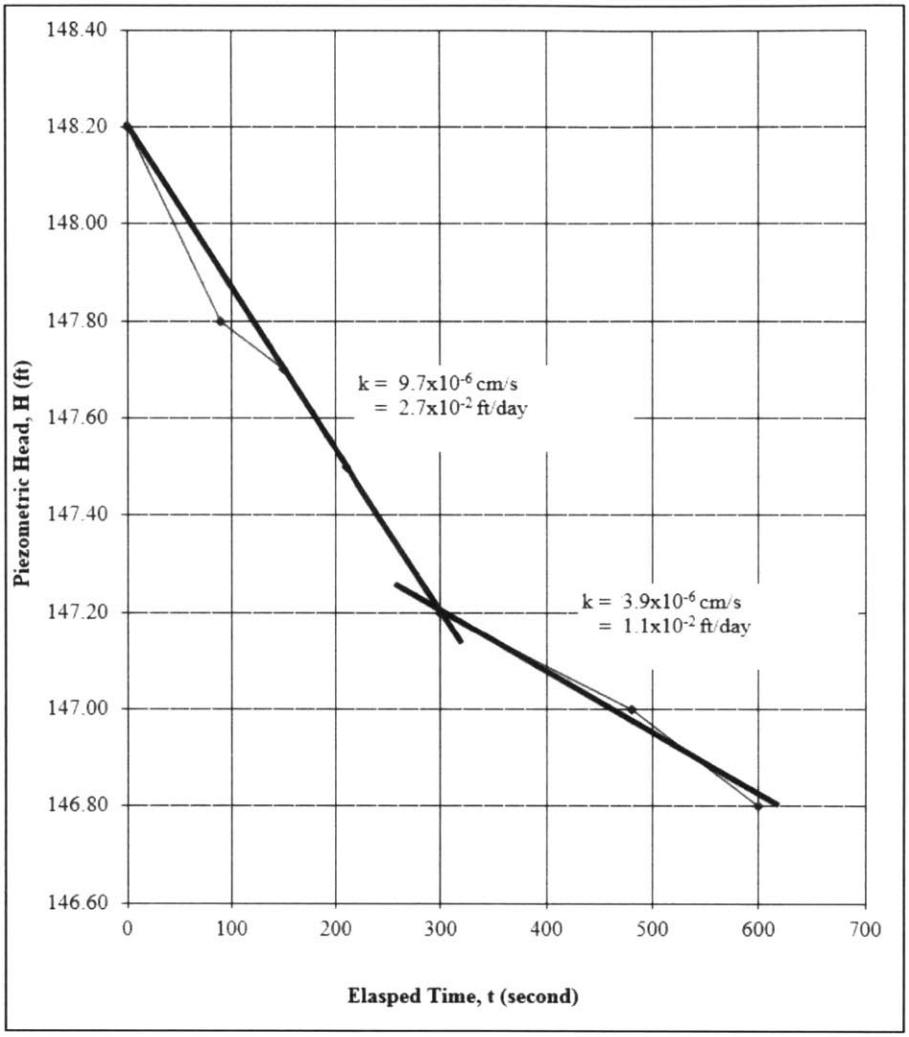

Figure 3.6: Falling head permeability test at boring CAN-06 (GZA, 2005).

A program of laboratory tests was conducted by GZA (2005) including gradation analyses, water contents, Atterberg Limits and triaxial compression tests. Eight natural water contents performed on individual embankment samples and five on foundation samples. Thirteen gradation analyses with hydrometer measurements were performed on individual samples. Five samples consisted of foundation soils with the remainder embankment soils. Gradation analyses with hydrometer measurements were also performed on three composite samples. Atterberg Limits were performed on eight individual embankment samples, five individual foundation samples, and three composite samples. Three anisotropically consolidated, undrained triaxial compression tests with pore pressure measures were performed on 4-inch diameter, reconstituted specimens. For each soil composite pairs of specimens were reconstituted and were run at different confining pressures (GZA, 2005). The results of the laboratory testing are summarized in Table 3.1.

Table 3.1: Laboratory testing data (GZA, 2005).

Soil Type	Impervious Fill	Semi-pervious Fill	Foundation Soil
Description	silt and clay, some fine sand, some fine to coarse gravel, cobbles	medium to fine sand, some gravel, some silt, cobbles	v. dense glacial till (clayey silt; sand; cobbles)
Moisture Content (%)	10-15	10-15	11-26
Plastic Limit Range (%)	14-16	14-16	13-20
Liquid Limit Range (%)	16-25	16-25	21-33
Plasticity Index Range	2-11	2-11	4-14
ϕ' (deg.)	34	35	32
c' (psf)	200	0	200
γ_{total} (pcf)	135	137	133
γ_{dry} (pcf)	121	122	112
Poisson's Ratio, v	0.27	0.27	0.27
V_s (ft/s)	2774	2774	2622
E (psf)	7.3E+07	7.4E+07	6.1E+07
$k_{average}$ (ft/day)	-	-	0.019

Note: $\rho = \frac{\gamma_{total}}{g}$ and $E' = 2(1 + v')G$

The impervious fill typically consists of silt and clay with some fine sand and some fine to coarse gravel. In-situ moisture contents ranged from w = 10 to 15%, with plastic limits w_p = 14 to 16%, and liquid limit w_L =16 to 25%, hence the plasticity index I_p = 2 to 11%. The measured internal friction angle, $\varphi' = 34°$ with an apparent cohesion, c' = 200 psf. The total and dry unit weights were calculated to be 135 and 121 pcf, respectively. Poisson's ratio and average shear wave velocity were calculated via cross-hole testing and estimated to be, v' = 0.27 and v_s =2774 ft/s, respectively. Based on in-situ and laboratory data, the average Young's modulus, E = 7.3E+07 psf. No hydraulic conductivity data was obtained for the impervious fill.

The semi-pervious fill typically consists of medium to fine sand with some gravel and some silt. Laboratory test ranges were similar to the impervious fill, with in-situ moisture contents from w = 10 to 15%, with plastic limits w_p = 14 to 16%, and liquid limit w_L =16 to 25%, hence the plasticity index I_p = 2 to 11%. The measured internal friction angle, $\varphi' = 35°$ with an apparent cohesion, c' = 0. The total and dry unit weights were calculated to be 137 and 122 pcf, respectively. Poisson's ratio and average shear wave velocity were assumed to be the same as the impervious fill. Based

on in-situ and laboratory data, the average Young's modulus, E = 7.4E+07 psf. No hydraulic conductivity data was obtained for the semi-pervious fill.

The foundation soils typically consisted of very dense glacial till deposits. The glacial deposits consisted typically of clayey silt with little sand and occasional cobbles and boulders. In some localized areas the till grades to a silt and sand. Index property data show in-situ moisture contents from w = 11 to 26%, with plastic limits w_p = 13 to 20%, liquid limit w_L =21 to 33% and I_p = 4 to 14%. The measured internal friction angle, $\varphi' = 32°$ with an apparent cohesion, c' = 200 psf. The total and dry unit weights were calculated to be 137 and 122 pcf, respectively. Poisson's ratio and average shear wave velocity were calculated via cross-hole testing and estimated to be 0.27 and 2622 ft/s, respectively. Based on in-situ and laboratory data, the average Young's modulus, E = 6.1E+07 psf. The average hydraulic conductivity for the till was estimated to be, k = 0.02 ft/day, see Figure 3.6.

Piezometer data versus reservoir elevation is periodically collected for the dam via an automated data acquisition system, see Figure 3.7 below for piezometric data and reservoir elevation over time for piezometers located through the maximum section of the dam. All elevation values reference NGVD29. Note the erratic piezometer data in the summer of 2015 will be discussed in Section 3.3 (GZA, 2005).

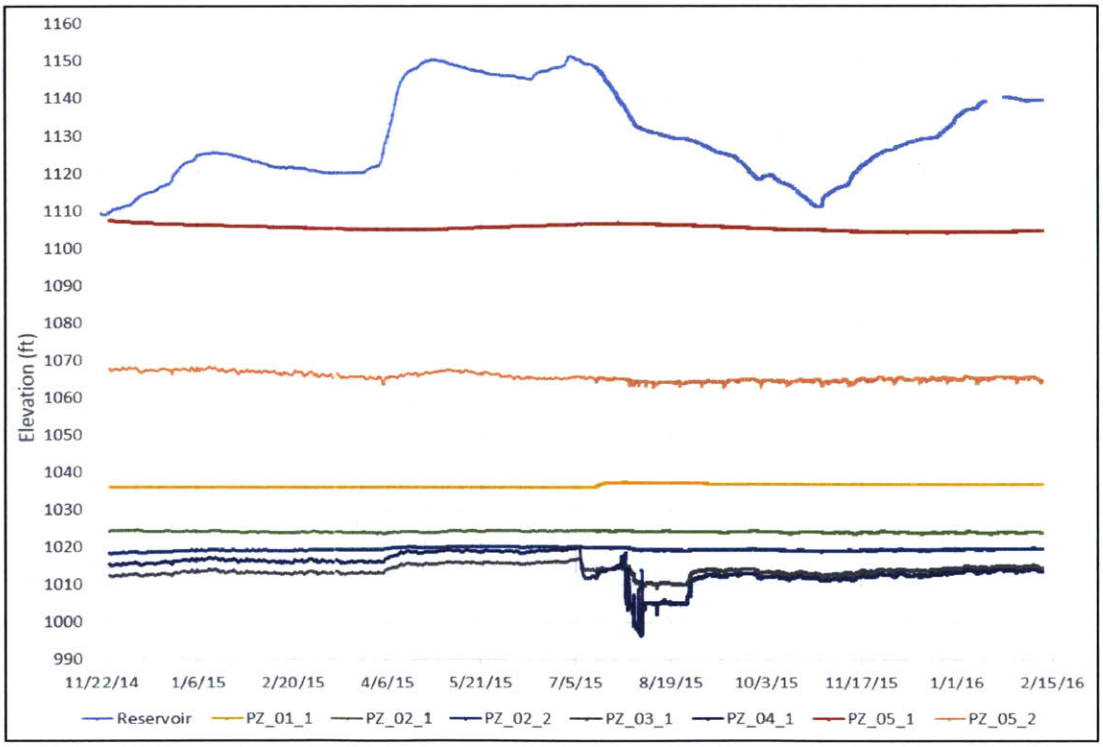

Figure 3.7: Piezometer and reservoir data versus time at the maximum section (Hover, 2016).

As discussed in further detail in Section 4.1, piezometer data for the CV dam was used to calibrate the finite element model to steady flow conditions. The piezometer readings are generally stable throughout the period of record; thus steady flow conditions can be inferred.

3.3 Major Seepage Event and Piezometer Response

During the summer of 2015, uncontrolled seepage occurred downstream of the CV dam near the existing outlet works (Figure 3.1). During a test boring program initiated to gather information for future hydropower development at the dam, it appears that a borehole near the downstream toe of the dam was not properly backfilled with bentonite after partial cave-in (Hover, 2016). The insufficiently sealed borehole created a preferential seepage pathway for groundwater and led to a significant amount of fine-grained particles to be released into the river downstream of the dam (Figure 3.8). This release of fines caused abnormally high turbidity levels downstream, which triggered 24/7 monitoring and a full investigation and repair plan. This precaution was taken as increased turbidity downstream of an embankment dam can be an indicator of internal erosion (i.e., active failure) of the embankment (Hover, 2016).

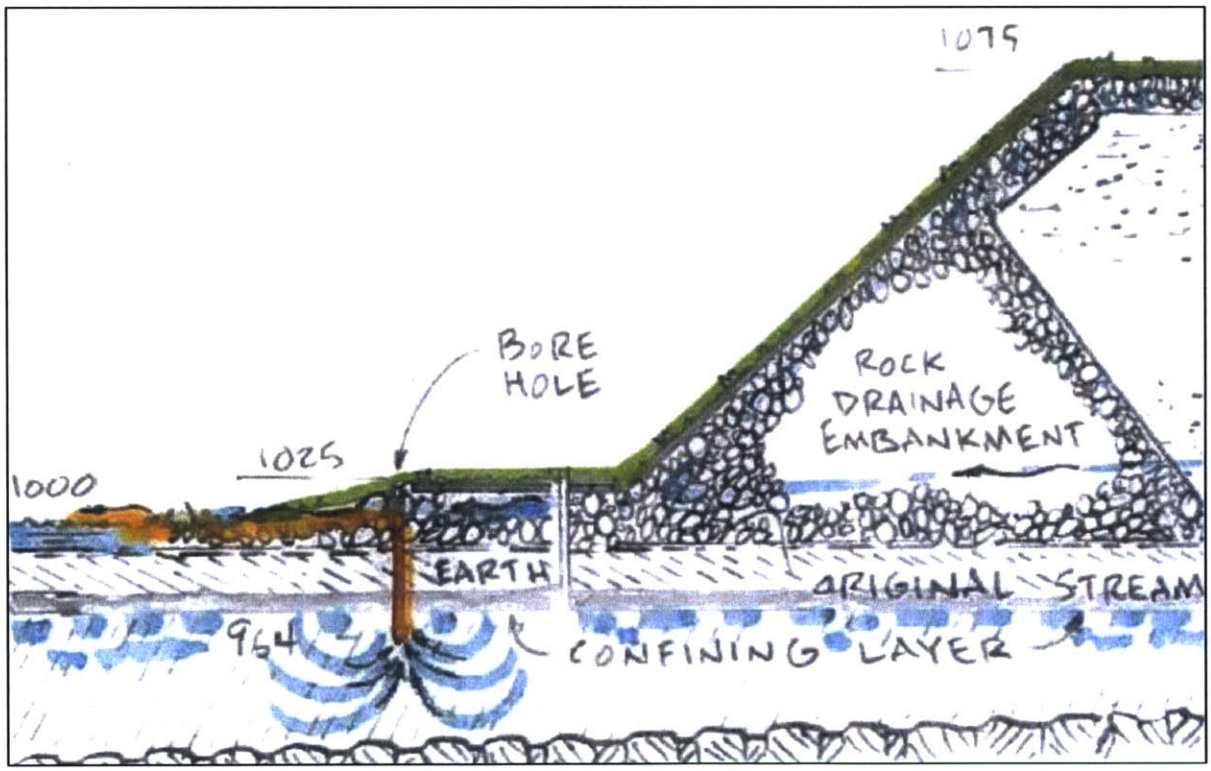

Figure 3.8: Sketch of section through CV dam showing the seepage from borehole (Rush, 2015).

What makes this event noteworthy is that the groundwater pressure response within the dam can be seen in the collected piezometer data. One week after the test borings started, elevated turbidity levels were noted at the downstream water treatment facility. A preferential seepage pathway had opened up on the downstream side of the dam causing piezometric pressures within the dam to quickly decrease. Relief wells were installed in the surrounding area which further decreased piezometric pressures before reaching a steady-flow condition. Shortly after water pressures within the embankment had stabilized, injection grouting was used along the downstream slope and toe to seal seepage pathways. Piezometric pressures immediately returned to a normal operating level after grouting was completed. Figure 3.9 below shows piezometer data and significant dates corresponding to the seepage event.

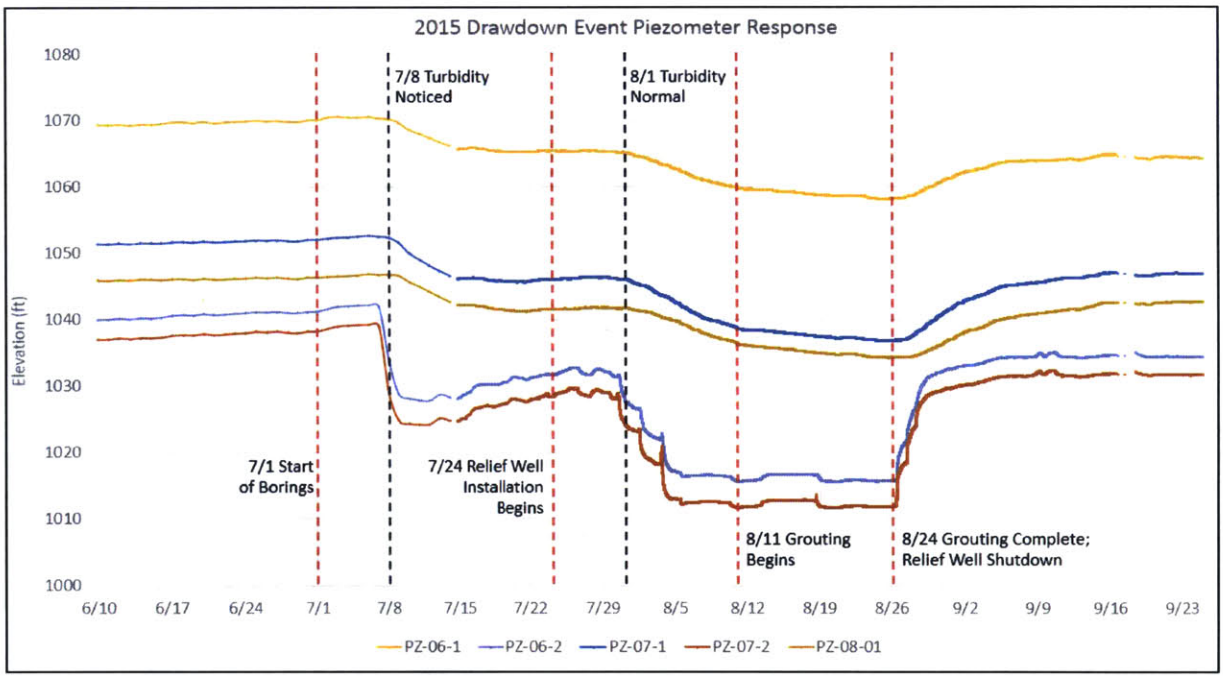

Figure 3.9: Piezometer readings and timeline corresponding to 2015 uncontrolled seepage event.

4.0 Methodology

This chapter describes the assumptions and interpretation of available data used to construct a numerical finite element (FE) model using the commercial 2-D FE program, PLAXIS 2D 2015™ (Plaxis, 2015). The goal is to analyze the stability of the CV dam under rapid drawdown (RDD) conditions, evaluating both instantaneous and time-dependent drawdown conditions. An FE model is calibrated to the steady seepage conditions observed in the CV dam and is then used to investigate how stability is affected by instantaneous and time-dependent drawdown of the reservoir. The analyses focus on conditions at the maximum section of the dam (Section A-A', Figure 3.2), due to the availability of geometric information and measured data. All elevations reference NGVD29. Results of the studies are presented in Section 5.0.

4.1 Steady Flow Model

Using the available data from GZA, a finite element model was created for the CV dam and the steady-state seepage behavior of the model was calibrated based on observed piezometric data from Hover (2016). See Section 3.2.1 for discussion on material properties and Table 3.1 for soil parameters used.

Since hydraulic conductivity properties of the "impervious" and "semi-pervious" fill materials are unknown, a search was conducted within expected orders of magnitude[3] to find the best fit parameters by comparing the computed and observed piezometric heads at five piezometer locations within the embankment (Points K-O; Figure 4.1). Table 4.1 summarizes the piezometric head conditions for these piezometers. Optimal values for hydraulic conductivity are selected based on the minimum lease squared error approach. Figure 4.1 shows the soil strata and constructed mesh used in the model.

Boundary conditions were applied to the geometric model and included zero vertical and horizontal displacement constraints for the base of the model and zero horizontal displacement constraints at the left and right vertical boundaries (Figure 4.1). Hydraulic boundary conditions for the steady flow FE model at normal pool El. 1150 ft are shown on Figure 4.2. Downstream constant head boundaries were established from piezometer data at boring CAN-04. Figure 4.3 shows the total vertical stress (σ_v) distribution estimated for the steady flow FE model. Figure 4.4 shows the steady-state pore pressure distribution. Note these steady flow FE models utilize the "groundwater

[3] Expected range based on typical values of hydraulic conductivity published in VandenBerge et al. (2013).

flow only" calculation type which does not consider soil deformation. This calculation type is used for pure groundwater flow calculations under saturated and unsaturated flow conditions (Plaxis, 2015).

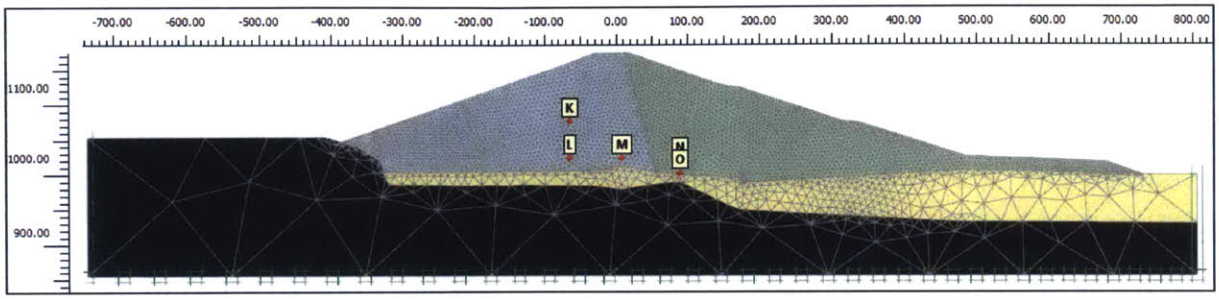

Figure 4.1: FE steady flow model soil strata, mesh and piezometer locations.

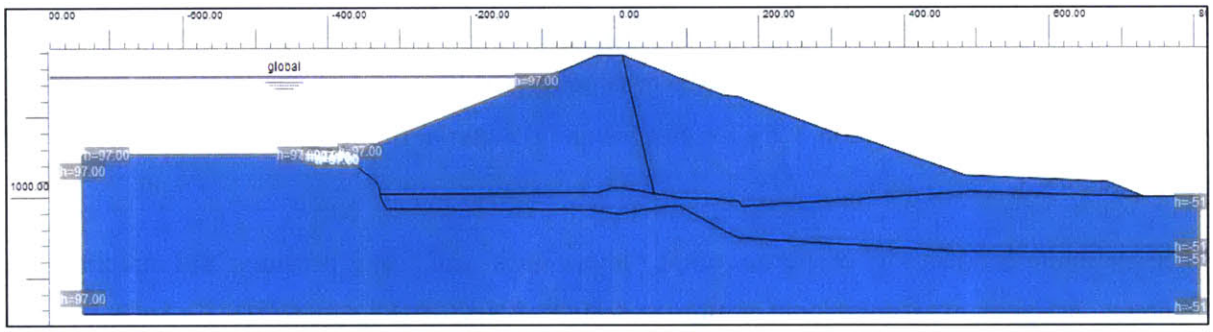

Figure 4.2: FE steady flow model hydraulic boundary conditions.

Table 4.1: Piezometer measurements of steady-state piezometric heads (GZA, 2005).

Label	Boring ID	PZ No.	Stratum	Elevation Head, H_e (ft)	Steady Piezometric Head, H_{ss} (ft)
K	CAN-05	PZ-01	IMPERVIOUS	1076.0	1103.8
L	CAN-05	PZ-02	IMPERVIOUS	1023.0	1064.3
M	CAN-01	PZ-01	IMPERVIOUS	1023.0	1033.5
N	CAN-02	PZ-01	SEMI-PERVIOUS	1019.0	1025.0
O	CAN-02	PZ-02	SEMI-PERVIOUS	1001.0	1011.9

Note: All elevations reference NGVG29 datum.

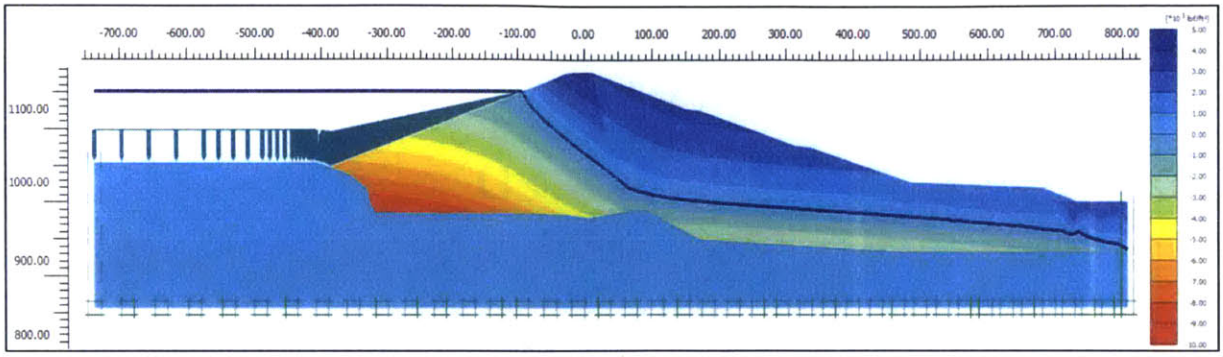

Figure 4.3: FE steady flow model vertical Cartesian total stress (σ_v) distribution.

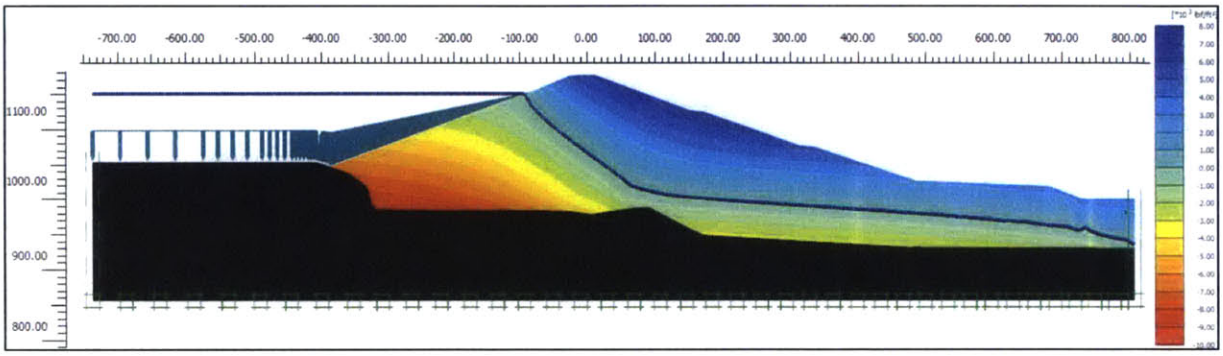

Figure 4.4: FE steady flow model steady-state pore pressure distribution.

4.2 Staged Construction

Using the calibrated hydraulic conductivity parameters, staged construction was modeled to establish equilibrium effective stress conditions within the CV dam prior to simulating the RDD events and performing c-phi reduction analyses. The stress history was modeled by simulating the original stream level (El. 999 ft) before constructing the CV dam in 4 layers of (each approximately 45 ft high, Figure 4.5). Figure 4.6 shows the vertical Cartesian stress distribution after staged construction prior to the reservoir being raised to the normal reservoir level (El. 1150 ft). A final stage was modeled to establish confining stresses after raising the reservoir water level to El. 1150 ft. Figure 4.7 shows the vertical Cartesian stress distribution after the reservoir was raised to El. 1150 ft. Figure 4.8 shows the resulting pore pressure distribution after staged construction with the reservoir at El. 1150 ft. Note the difference between Figure 4.8 and Figure 4.4 due to the elasto-plastic deformation calculation type used for staged construction. These analyses assume fully drained, steady-state conditions and establish the initial stresses prior to RDD events.

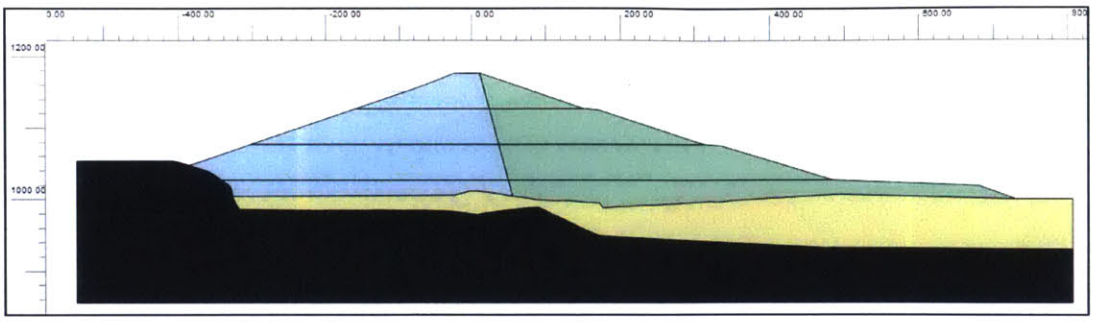

Figure 4.5: FE model showing staged construction embankment layers and foundation soils.

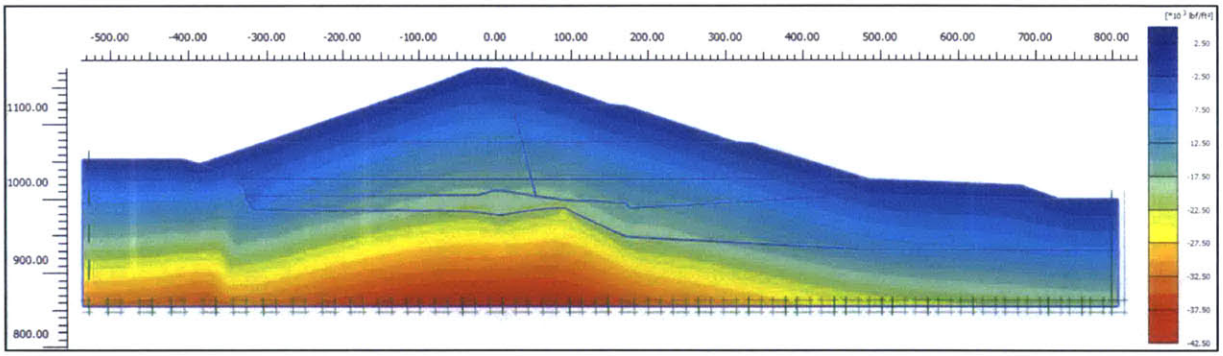

Figure 4.6: Vertical Cartesian total stresses (σ_v) after staged construction before raising the reservoir.

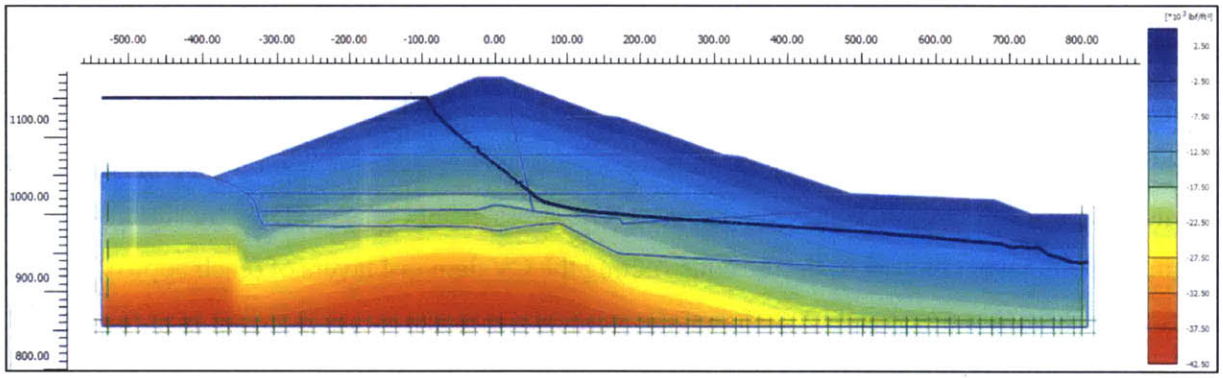

Figure 4.7: Vertical Cartesian total stresses (σ_v) after raising the reservoir to El. 1150 ft.

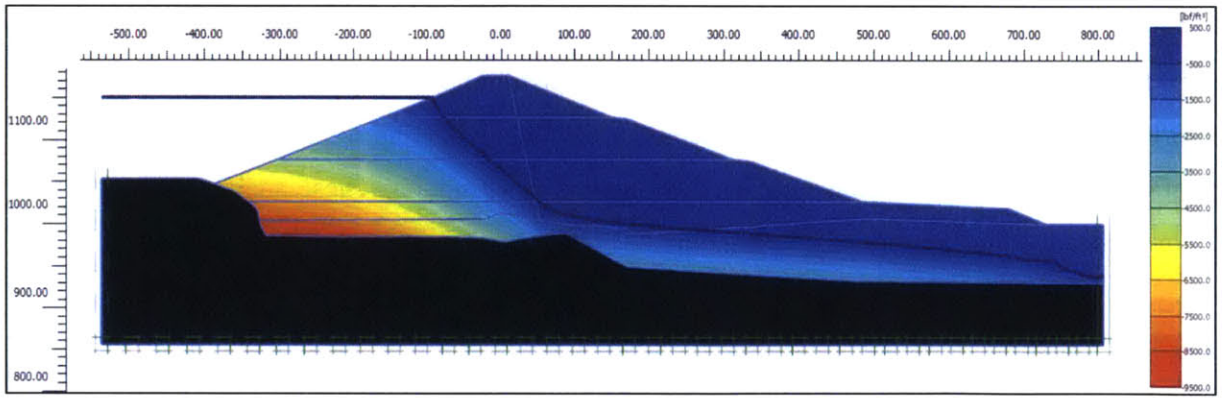

Figure 4.8: Steady-state pore pressure distribution after raising the reservoir to El. 1150 ft.

4.3 Instantaneous Drawdown

Using the calibrated FE model and established confining stresses, the effect of instantaneous drawdown was evaluated for undrained conditions in the embankment dam. This is achieved using c-phi strength reduction analyses (Brinkgreve and Bakker, 1991) based on drained effective stress parameters (c', φ') to estimate the factor of safety for slope stability after simulating the changed boundary conditions associated with the instantaneous removal of water load on the slope. The fill layers are modeled as Mohr-Coulomb materials with effective stress strength parameters (c', φ'). The equivalent undrained shear strength can be found from:

$$s_u = c'cos\varphi' + \frac{1}{2}(\sigma_1' + \sigma_3')sin\varphi' \qquad (4.1)$$

In order to evaluate the effect of instantaneous drawdown, changes in total stresses inside the dam are obtained by simulating the change in boundary pressures on the upstream slope resulting from the lowered reservoir pool level. This was accomplished by running each undrained analysis with the steady flow reservoir level (El. 1150 ft) adding a distributed load perpendicular to the upstream slope between El. 1150 ft and each selected drawdown level, to simulate an instantaneous drop in reservoir level. The added load is comprised of two parts: a linear distributed load to negate the hydrostatic force between the drawdown level and El. 1150 ft and, a uniform distributed load to decrease the hydrostatic load below the drawdown level to that which would result from that new reservoir level. Figure 4.9 illustrates the upstream boundary condition with distributed load to mimic instantaneous drawdown. Table 4.2 shows the calculation of water pressures used in the undrained analyses. Model results of slope stability of the CV dam for instantaneous drawdown are discussed in Section 5.2 of this report.

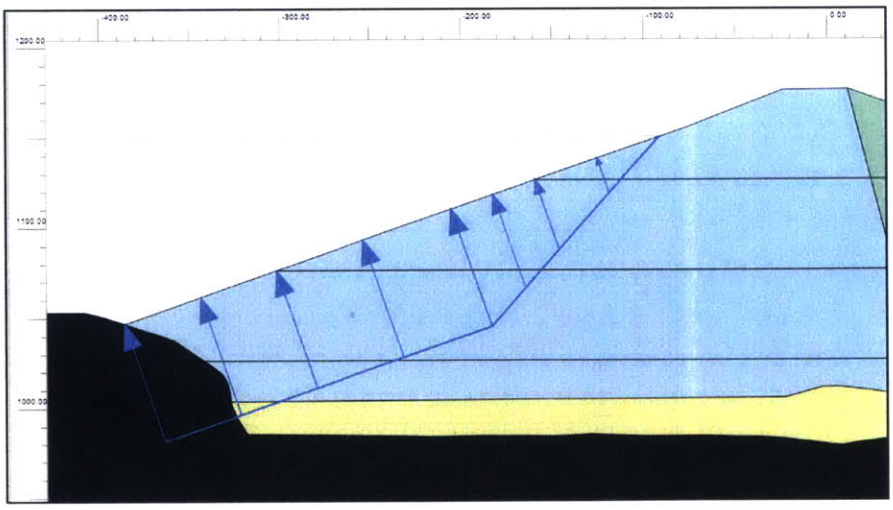

Figure 4.9: Upstream slope of FE model with distributed load to mimic instantaneous drawdown.

Table 4.2: Water pressure calculation for each instantaneous drawdown level.

Drawdown Condition	Depth of Reservoir (ft)	WSEL (ft, NGVD29)	P_{bottom} (psf)	Difference (psf)
Normal Pool	97	1150	6175	0
Minus 20'	77	1130	4902	-1273
Minus 40'	57	1110	3629	-2546
Minus 60'	37	1090	2355	-3820
Minus 80'	17	1070	1082	-5093
Minus 97' (empty)	0	1053	0	-6175

4.4 Time-Dependent Drawdown

Using the calibrated FE model, the time-dependent drawdown effect on slope stability was evaluated, for selected reservoir pool elevations with partial drainage (transient seepage conditions) and strength reduction analyses. Within PLAXIS 2D, transient seepage conditions were modeled using the "fully-coupled flow deformation (consolidation)" calculation type, with the option to include suction in the analyses (Plaxis, 2015). As mentioned previously, the reducing phreatic surface within the dam lags above the drawdown of the reservoir and can produce an area of capillarity (i.e., matric suction) above the phreatic surface affecting the soil shear strength in this zone. The current analyses assume that the shear strength of the fill materials is controlled by effective stresses with the Mohr-Coulomb strength criteria.

Figure 4.10 illustrates the control of drawdown in the reservoir (this case represents 40 feet of drawdown occurring in 10 days). Model results of slope stability for time-dependent drawdown are discussed in Section 5.3 of this report.

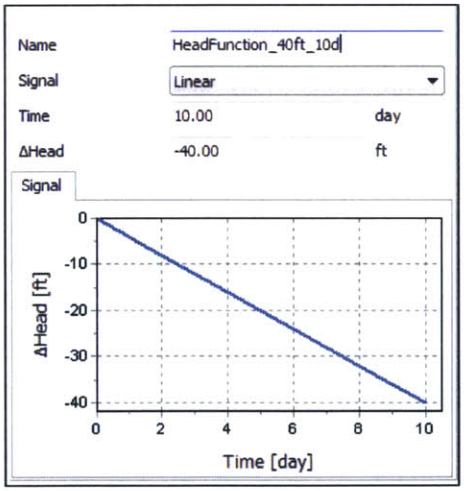

Figure 4.10: Example linear drawdown function for 40 feet of drawdown over 10 days.

5.0 Results of Numerical Analysis

This chapter describes the results of the 2-D finite element (FE) analyses using PLAXIS 2D 2015™ (Plaxis, 2015) for evaluating slope stability of a large embankment dam (CV dam) under rapid drawdown (RDD) conditions. The FE analyses use Mohr-Coulomb Criteria to describe the stress-strain strength properties of the embankment fill materials (Figure 3.3). The previous chapter describes construction and calibration of these models based on available data (GZA, 2005). These analyses subdivide the CV dam into "impervious" fill, "semi-pervious" fill, glacial till and bedrock soil units, see Table 3.1 for material parameters.

5.1 Steady Flow Model

A search was conducted to find the best fit hydraulic conductivity parameters for the impervious and semi-pervious fill materials to compare modeled piezometric heads with observed values for the steady flow condition. Piezometric heads were compared at five piezometer locations within the embankment fill at the maximum section (Points K-O; Figure 4.1). Optimal values for hydraulic conductivity were selected based on the minimum lease squared error approach. See Figure 4.1 for soil strata and constructed mesh used in the model.

Figure 5.1 shows the results for the steady flow least squared errors (LSE) analyses plotted with contours of log(LSE). Contours were generated using cubic interpolation within MATLAB R2016a (MathWorks, 2016). See Appendix A for complete tabular results of all LSE analyses. The results of the LSE analyses show that the smallest errors (i.e., best agreement) between modeled and observed piezometric heads, occur when hydraulic conductivity of the impervious fill, k_{imp} = 3E-3 ft/day (shown by the white vertical band on Figure 5.1). The best agreement occurs at the point when the hydraulic conductivity, k = 3E-3 ft/day, for both impervious and semi-pervious fills. These best fit hydraulic conductivity parameters represent the calibrated FE steady flow model to be used in subsequent RDD analyses (this is Model No. 41 in Appendix A).

Figure 5.2 shows the calibrated steady flow phreatic surface (blue) and estimated groundwater head distribution, as well as the observed phreatic surface (red) from GZA (2005). Most of the discrepancy between the observed and modeled phreatic surface occurs at the interface between the two zones of impervious and semi-pervious fill materials (which appears to have similar k). The actual dam may have graduation in material properties in this area. In general, upstream pore pressures are in good agreement with pore pressures in the impervious fill, which is the most critical for subsequent RDD analyses. Total vertical Cartesian stresses and calculated pore

pressures for the calibrated FE steady flow model are shown below in Figure 5.3 and Figure 5.4, respectively.

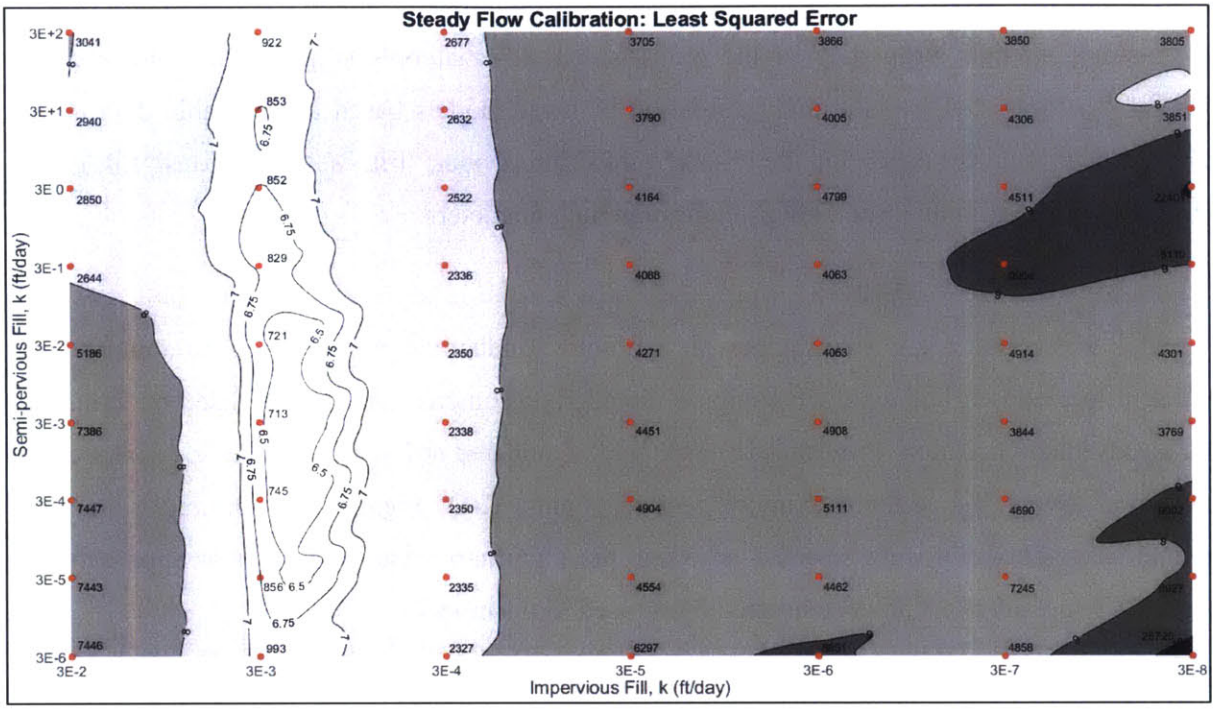

Figure 5.1: Results for steady flow LSE analyses plotted using cubic interpolation contours.

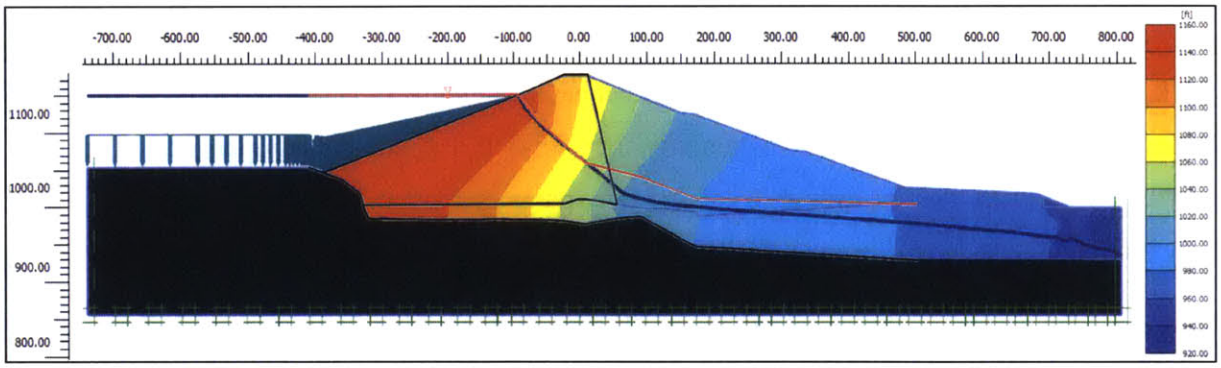

Figure 5.2: Comparison of calibrated model (blue) and GZA (2005) (red) phreatic surface.

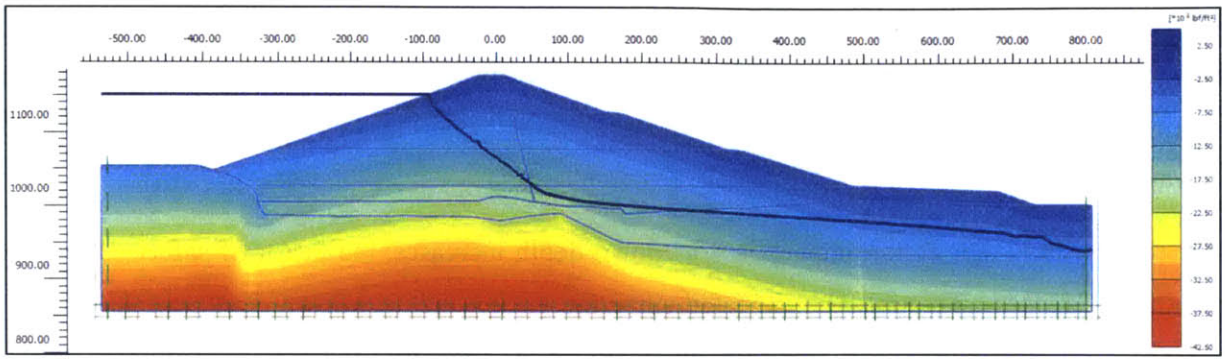

Figure 5.3: Vertical Cartesian total stress (σ_v) distribution prior to drawdown events

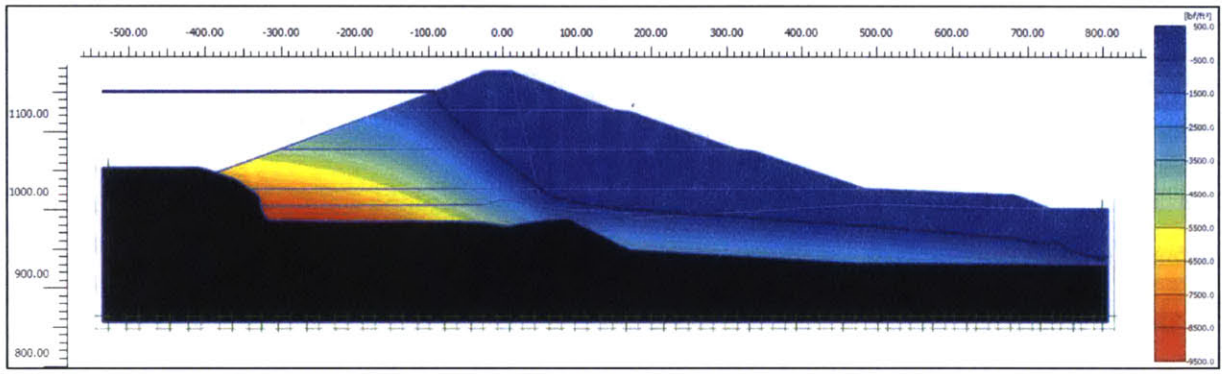

Figure 5.4: Steady-state pore pressure distribution prior to drawdown events.

5.2 Instantaneous Drawdown

The effect of instantaneous drawdown was evaluated for undrained conditions in the CV dam. This was achieved using c-phi strength reduction analyses (Brinkgreve and Bakker, 1991) based on drained effective stress parameters (c', φ') to estimate factors of safety for slope stability after simulating the changed boundary conditions associated with the instantaneous removal of water load on the slope. As discussed in Section 4.3, undrained conditions were evaluated by running each model with the steady flow reservoir level (El. 1150 ft) and adding a distributed load perpendicular to the upstream slope between El. 1150 ft and the drawdown level, to simulate an instantaneous drop in reservoir level.

Figure 5.5 shows the resulting factors of safety from c-phi reduction analysis of the CV dam after instantaneous drawdown to selected reservoir levels. Figure 5.6 through Figure 5.11 show the total displacements (i.e., failure mechanisms for slope instability) associated with each strength reduction analysis after each undrained deformation (instantaneous drawdown) analysis. Included as Appendix B are active pore pressure distributions corresponding to each instantaneous drawdown analysis.

For small drawdown conditions (Δh_w = 48 ft; Figure 5.7) the slope failure is very shallow with back scarp at approximate El. 1130 ft. For larger drawdowns, the failure mechanism extends deeper into the dam while the back scarp is largely unaffected but the instantaneous drawdown elevation.

The results show that as instantaneous drawdown depth increases, the factor of safety for slope stability decreases. This is to be expected since the greater the drawdown depth, the larger the zone of exposed saturated soil along the upstream slope. The larger the exposed saturated zone, the larger the influence of the removed stabilizing hydrostatic force, hence a lower factor of safety. All failure mechanisms occur along the upstream slope, except for the normal reservoir (i.e., zero drawdown) model which occurs along the downstream slope. The critical instantaneous drawdown level corresponding to a factor of safety, FS = 1 is approximately Δh_w = 48 ft, as per Figure 5.5.

For the purposes of this thesis, it is assumed that the undrained slope stability analysis simulating instantaneous drawdown uses a conservative estimate of FS in estimating slope stability during RDD conditions.

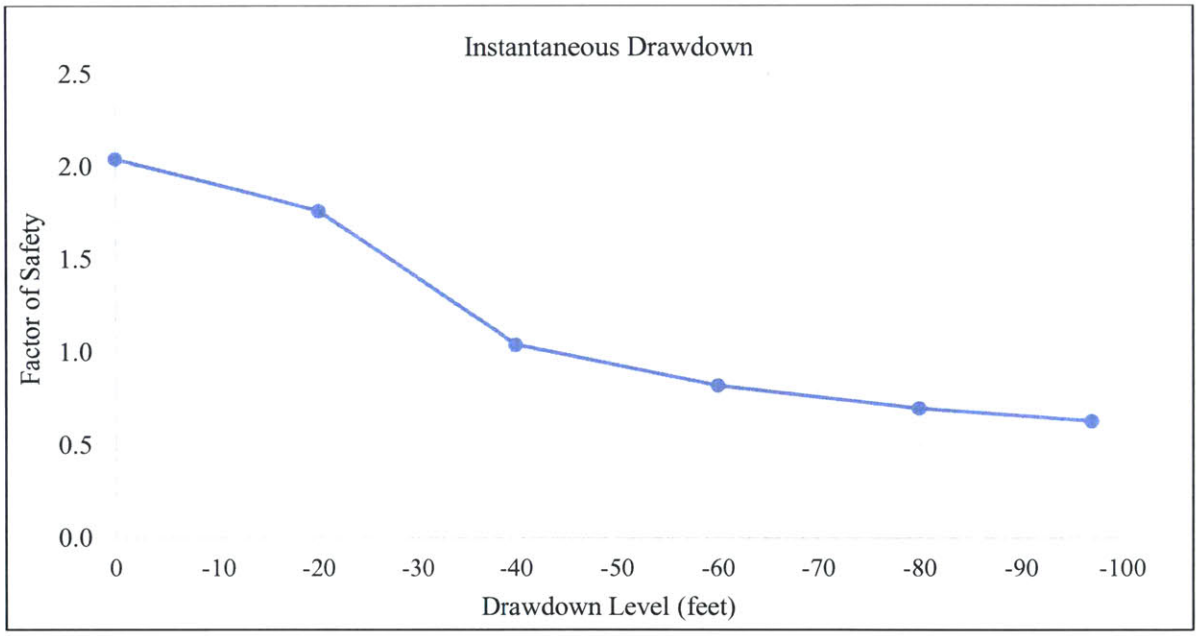

Figure 5.5: Factors of safety for various instantaneous drawdown levels.

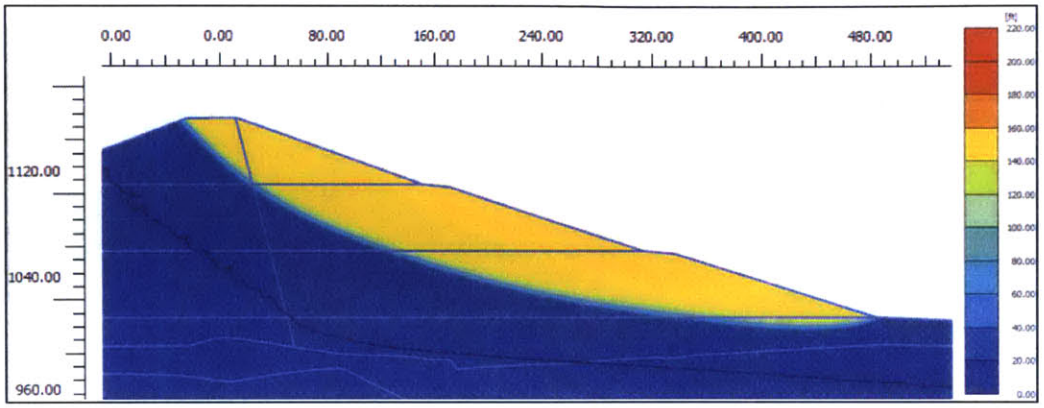

Figure 5.6: Strength reduction failure mechanism for normal reservoir pool, El. 1150 ft.

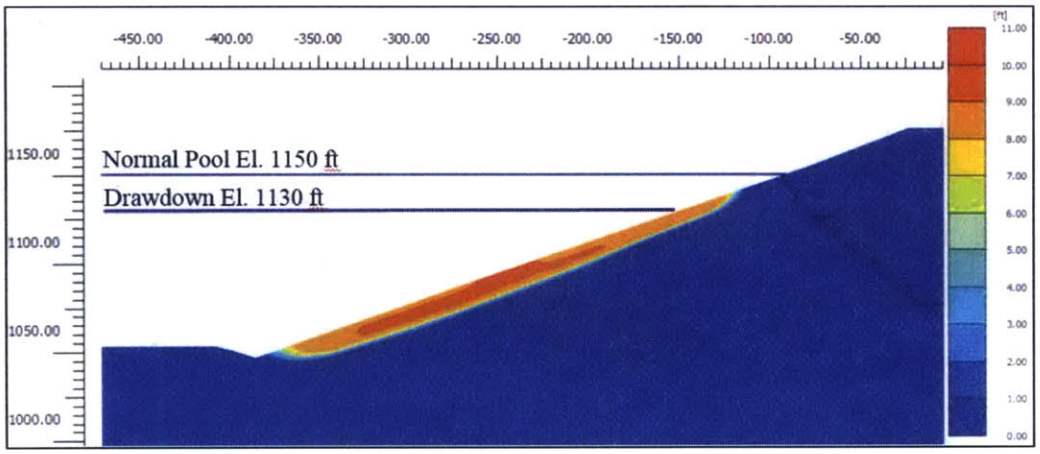

Figure 5.7: Strength reduction failure mechanism for 20 ft instantaneous drawdown to El. 1130 ft.

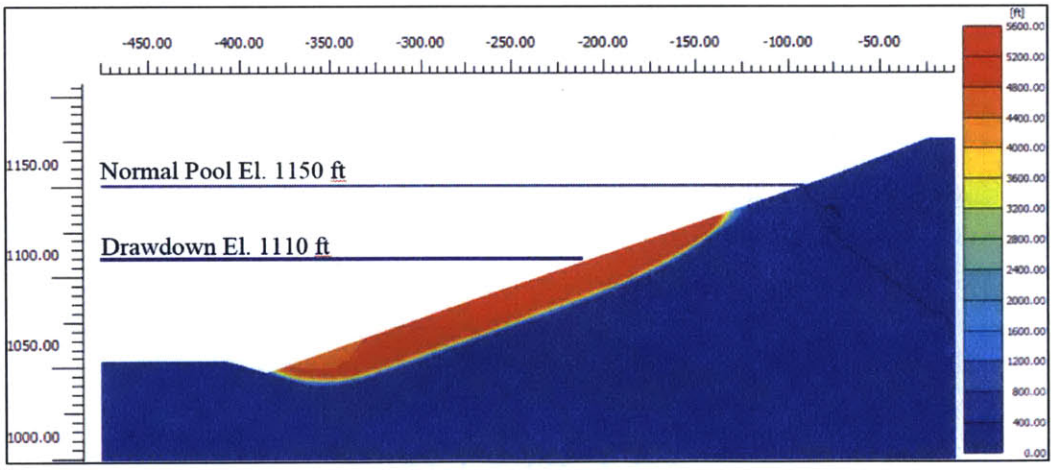

Figure 5.8: Strength reduction failure mechanism for 40 ft instantaneous drawdown to El. 1110 ft.

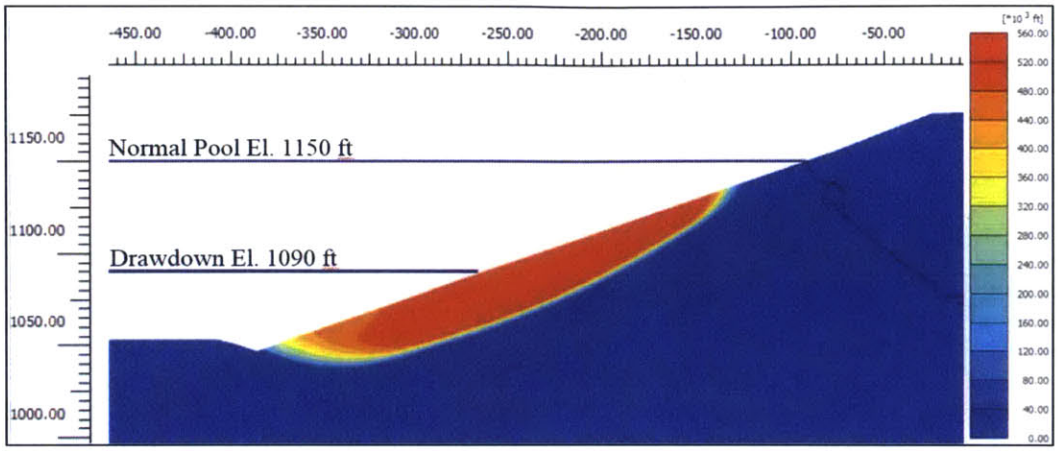

Figure 5.9: Strength reduction failure mechanism for 60 ft instantaneous drawdown to El. 1090 ft.

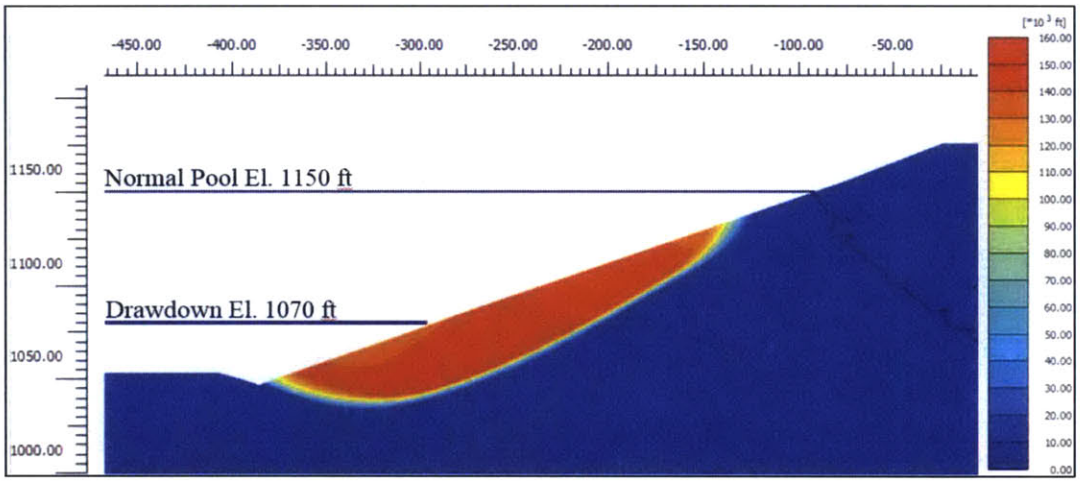

Figure 5.10: Strength reduction failure mechanism for 80 ft instantaneous drawdown to El. 1070 ft.

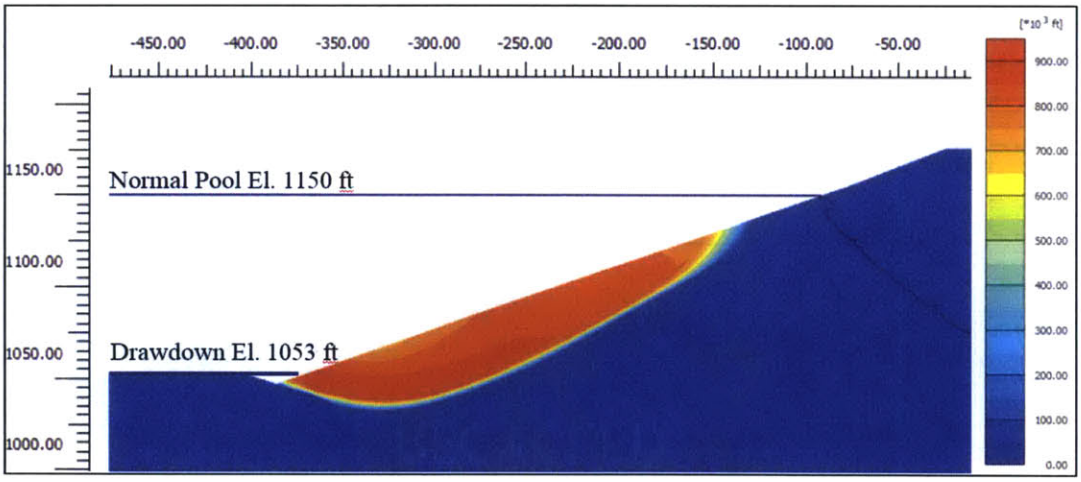

Figure 5.11: Strength reduction failure mechanism for 97 ft instantaneous drawdown to El. 1053 ft.

5.3 Time-Dependent Drawdown

The time-dependent drawdown effect on slope stability was evaluated, for the same selected drawdown levels, with partial drainage (transient seepage conditions) and strength reduction analyses. Drawdown behavior was controlled using linear functions within Plaxis 2D by specifying drawdown level and duration, see Figure 4.10. Suction was not ignored for these analyses.

Figure 5.12 shows the resulting factors of safety for slope stability for the FE strength reduction analyses after time-dependent drawdown. Included as Appendix C are total displacements (i.e., failure mechanisms for slope instability) associated with each strength reduction analysis and active pore pressure distributions corresponding to each time-dependent drawdown analysis.

The results show that for a given drawdown level, as drawdown time decreases, so does the factor of safety for slope stability. This is to be expected as the partial saturation and decreasing phreatic surface within the dam will move toward steady flow equilibrium as time passes. These results also show that the analyses for instantaneous drawdown do in fact bound the time-dependent analyses, as the time dependent factors of safety for slope stability are generally higher than those for instantaneous drawdown.

Based on information provided in GZA (2005), the maximum hydraulic discharge capacity of the CV dam is 2,400 MGD, which equates to a maximum operational drawdown rate of 1.7 feet per day (GZA, 2005). This maximum drawdown rate is based on the combined outlet works and intake structure discharge capacities and reflects the fastest drawdown of reservoir level that can be obtained by fully opening all outlet valves and removing all stoplogs from the intake structure overflow weirs. Based on this maximum drawdown rate, the minimum drawdown time was calculated for each Δh_w, shown in

Table 5.1 and indicated on Figure 5.12. The factors of safety to the left of the dashed line reflect drawdown rates which exceed the maximum rate and could only occur under severe circumstances such as a dam breach or malfunction of the outlet works / intake structure. As discussed for the Bouldin Dam failure in Section 2.2, RDD slope failures can occur as a secondary failure mechanism during a dam breach event. Factors of safety to the right of the dashed line represent drawdown rates that are less than the maximum rate, thus can be achieved through manual operation of the dam.

The critical factor of safety associated with full, time-dependent drawdown (Δh_w = 97 ft) at the maximum operational drawdown rate is approximately FS = 1.6, shown by a red dot on Figure 5.12.

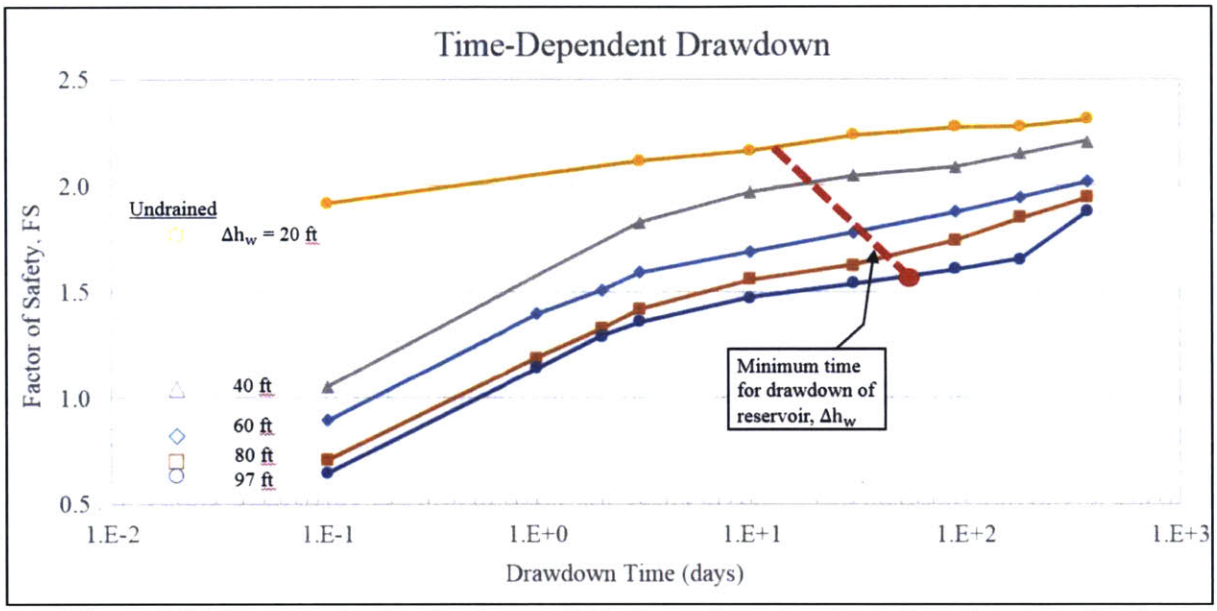

Figure 5.12: Factors of safety for slope stability for various time-dependent drawdown levels.

Table 5.1: Drawdown times for each drawdown level based on 1.7 feet per day.

Drawdown Level (ft)	Drawdown Time (days)
20	12
40	24
60	35
80	47
97	57

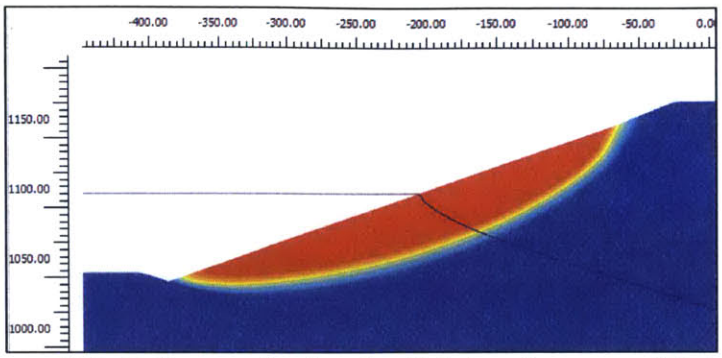

Figure 5.13: Failure mechanism for 40 ft drawdown over 365 days.

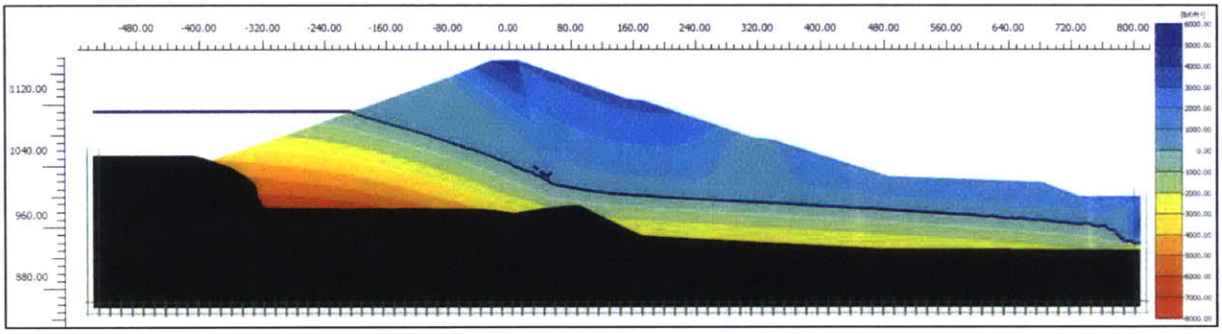

Figure 5.14: Active pore pressure distribution for 40 ft drawdown over 365 days.

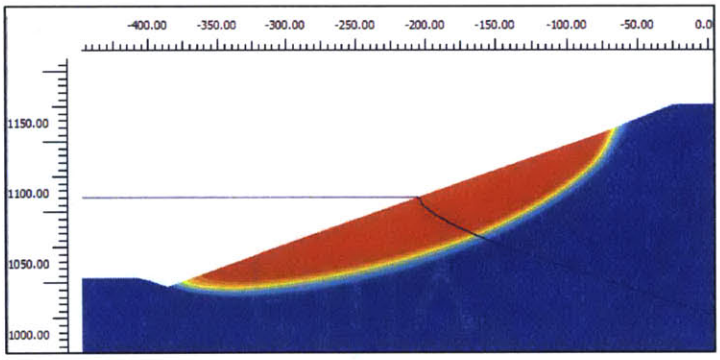

Figure 5.15: Failure mechanism for 40 ft drawdown over 180 days.

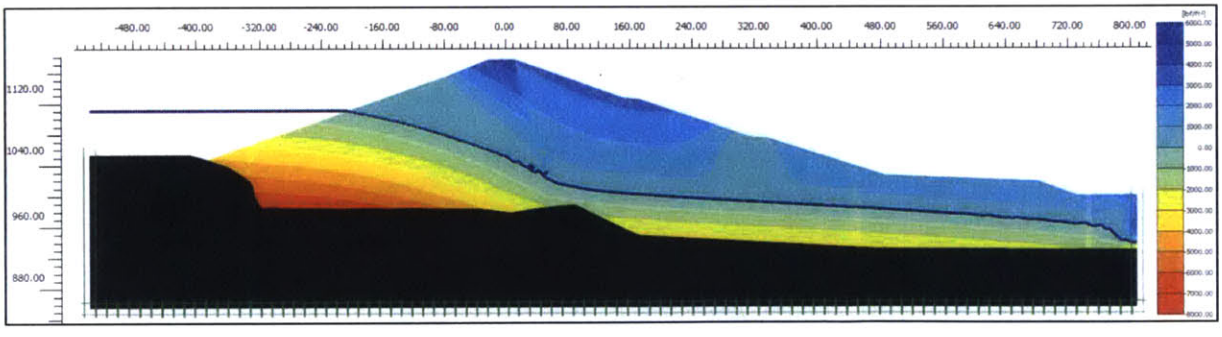

Figure 5.16: Active pore pressure distribution for 40 ft drawdown over 180 days.

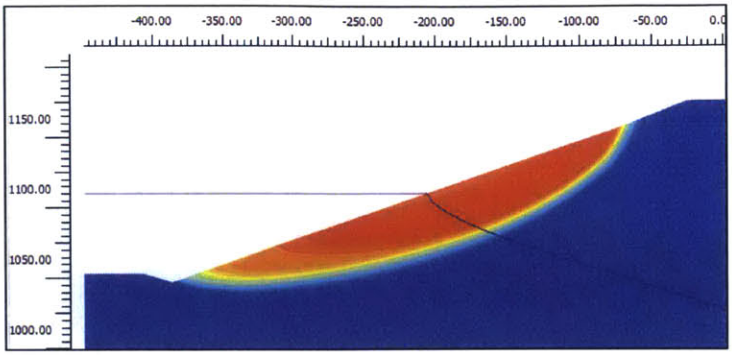

Figure 5.17: Failure mechanism for 40 ft drawdown over 90 days.

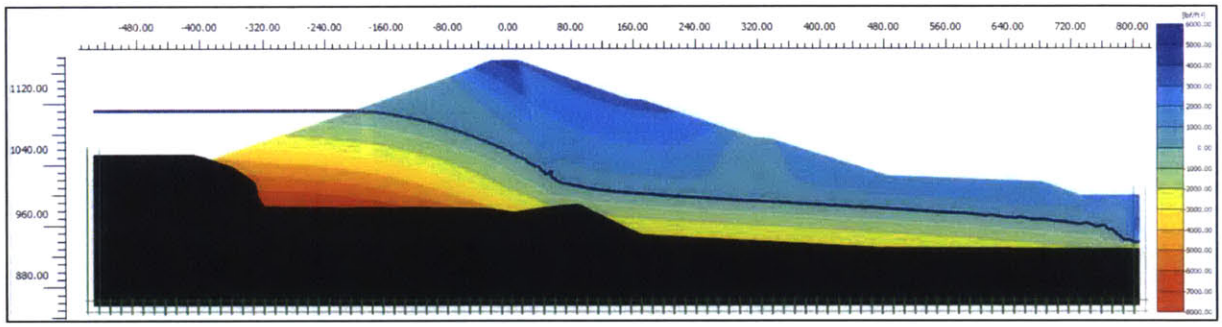

Figure 5.18: Active pore pressure distribution for 40 ft drawdown over 90 days.

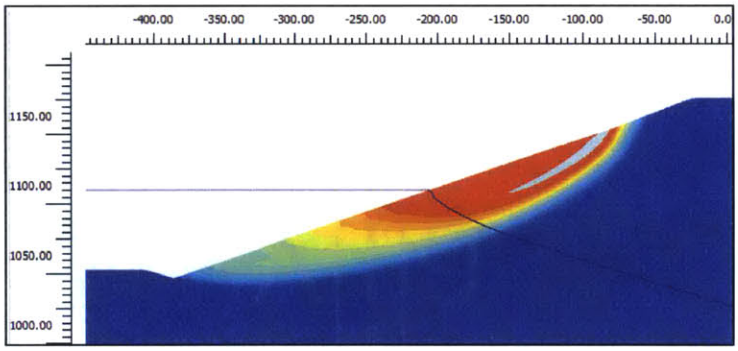

Figure 5.19: Failure mechanism for 40 ft drawdown over 30 days.

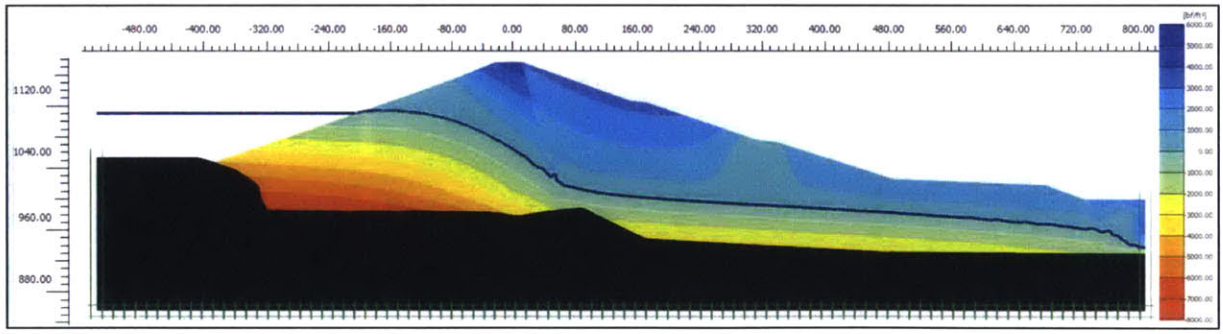

Figure 5.20: Active pore pressure distribution for 40 ft drawdown over 30 days.

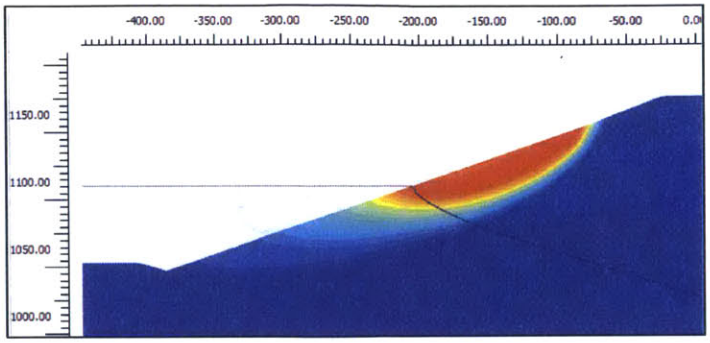

Figure 5.21: Failure mechanism for 40 ft drawdown over 10 days.

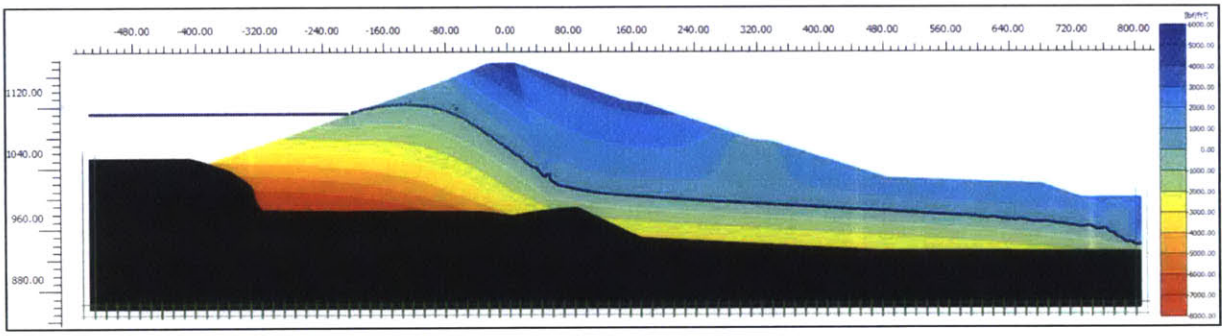

Figure 5.22: Active pore pressure distribution for 40 ft drawdown over 10 days.

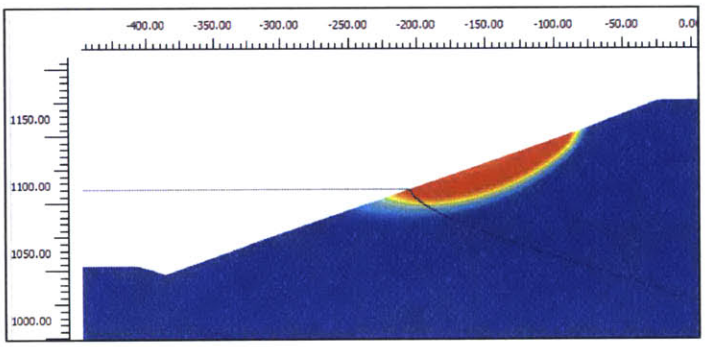

Figure 5.23: Failure mechanism for 40 ft drawdown over 3 days.

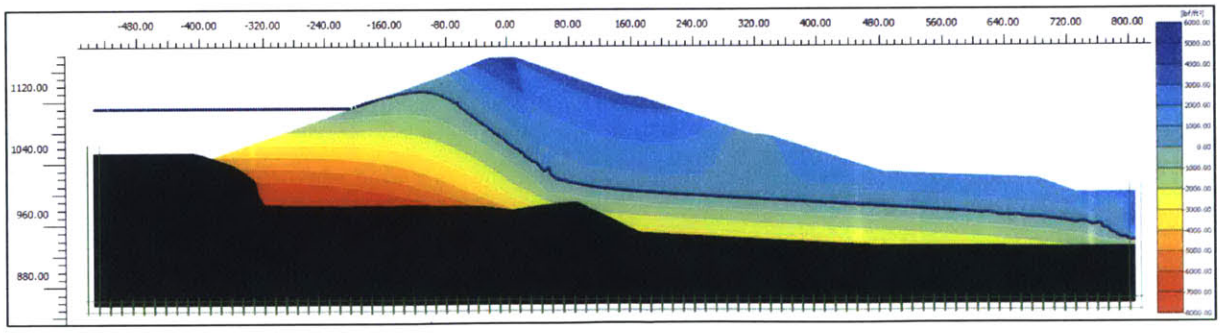

Figure 5.24: Active pore pressure distribution for 40 ft drawdown over 3 days.

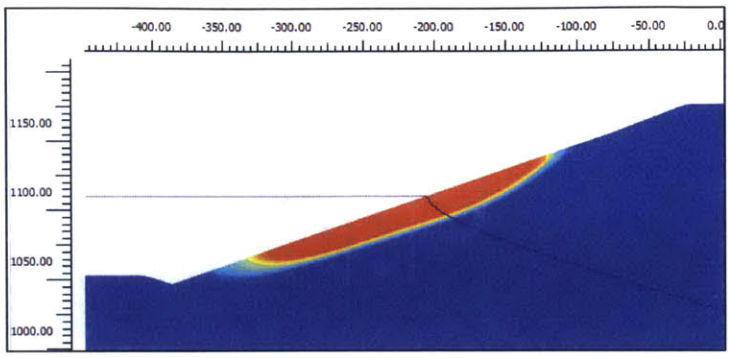

Figure 5.25: Failure mechanism for 40 ft drawdown over 0.1 days.

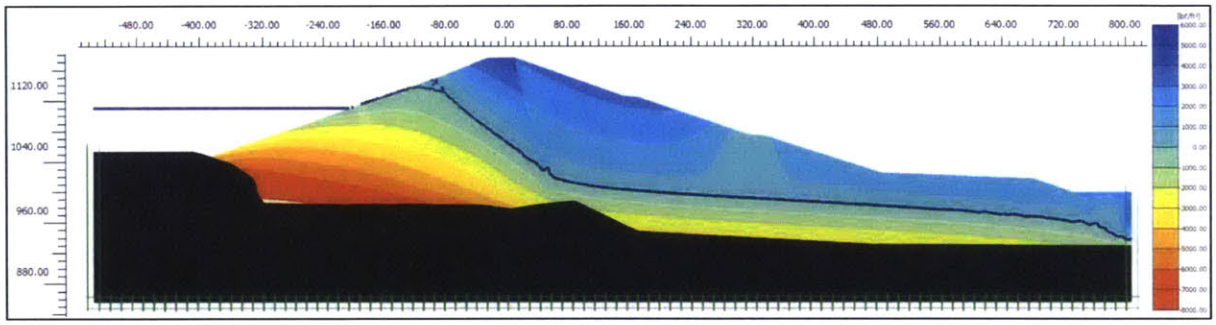

Figure 5.26: Active pore pressure distribution for 40 ft drawdown over 0.1 days.

6.0 Summary, Conclusions and Recommendations

6.1 Summary and Conclusions

This thesis evaluated the use of finite element (FE) analyses using PLAXIS 2D 2015™ as a tool for evaluating the slope stability of a large embankment dam (CV dam) subjected to rapid drawdown (RDD) conditions.

Data was made available for this thesis by GZA GeoEnvironmental, Inc. and was used to develop a numerical FE model for the maximum section of the CV dam. The FE model was calibrated to steady flow conditions using observed piezometer data. A least squared error (LSE) analysis was used to calibrate the hydraulic conductivity of each embankment fill material by minimizing the difference in piezometric head between the model and observed at five piezometer locations within the CV dam. Hydraulic conductivity was varied within expected orders of magnitude for both the impervious and semi-pervious fill materials. Hydraulic conductivity parameters were calibrated to the best fit using hydraulic conductivity, k = f 3E-3 ft/day for both fill zones (Figure 5.1).

The FE model was used to evaluate the upstream slope of the CV dam for undrained stability during instantaneous drawdown to selected reservoir pool levels. Steady flow conditions, based on the normal pool El. 1150 ft (NGVD), were modeled and the reservoir load corresponding to each instantaneous drawdown level was removed by adding a negative distributed load along the upstream slope, effectively mimicking instantaneous drawdown. The results show that as drawdown depth increases, the factor of safety for slope stability decreases. This was expected because the larger drawdown levels experience a proportional removal in the stabilizing hydrostatic force on the upstream slope, thus the larger the instantaneous drawdown, the smaller the factor of safety for slope stability. The critical instantaneous drawdown level is approximately 48 ft, where the factor of safety for slope stability is equal to one.

The model was used to evaluate the upstream slope of the CV dam for time-dependent drawdown. Identical drawdown levels to the instantaneous analyses were used, varying drawdown time for each analysis. Drawdown times ranged from 0.1 days to 365 days. The results show that as drawdown time increases, so does the factor of safety for slope stability due to transient redistribution of pore pressures in the dam. Also, as drawdown time decreases, factor of safety values approach the values obtained during the undrained drawdown analysis.

In order to validate the proposed RDD analyses for the CV dam, the time-dependent factor of safety corresponding to full (i.e., Δh_w = 97 ft) drawdown of the reservoir were compared with the

value from GZA (2005) at the maximum section of the dam. The values are in good agreement and shown in Table 6.1. Note that the results for "maximum drawdown" correspond to the maximum operational drawdown rate of 1.7 feet per day, resulting in a drawdown of 97 feet in 57 days. Lower factors of safety were obtained for the time-dependent 97 ft drawdown case (Figure 5.12) however they reside below the maximum operational drawdown rate, thus can only occur as a secondary failure mechanism.

Table 6.1: Proposed analysis results vs GZA (2005) for maximum drawdown case.

GZA (2005)	Proposed Analysis
1.7	1.6

Another comparison was made between results from the proposed time-dependent analysis and Hover (2016). Piezometer and reservoir data[4] obtained from Hover (2016) included a drawdown event of 40 feet in 114 days or 0.4 feet per day. A time-dependent analysis was conducted for a 40 ft drawdown occurring over 114 days and compared to the observed piezometer data reported by Hover (2016). Results are shown below in Figure 6.1. The difference in the starting points show that the FE model estimates a steady-state piezometric head about nine feet less than the observed data. The drawdown event produces less than a two-foot change in measured piezometric head at CAN-05-01, while the transient analysis suggests a 15 ft drop. These values suggest the k values used in the FE model are higher than in-situ and hence effects of the current coupled consolidation may underestimate results for the RDD event.

[4] It must be noted that this drawdown event was concurrent with the uncontrolled seepage event as described in Section 3.3, however piezometer CAN-05-01 was chosen for comparison as it is the most-upstream piezometer and showed negligible influence from the seepage event that the more-downstream piezometers exhibited.

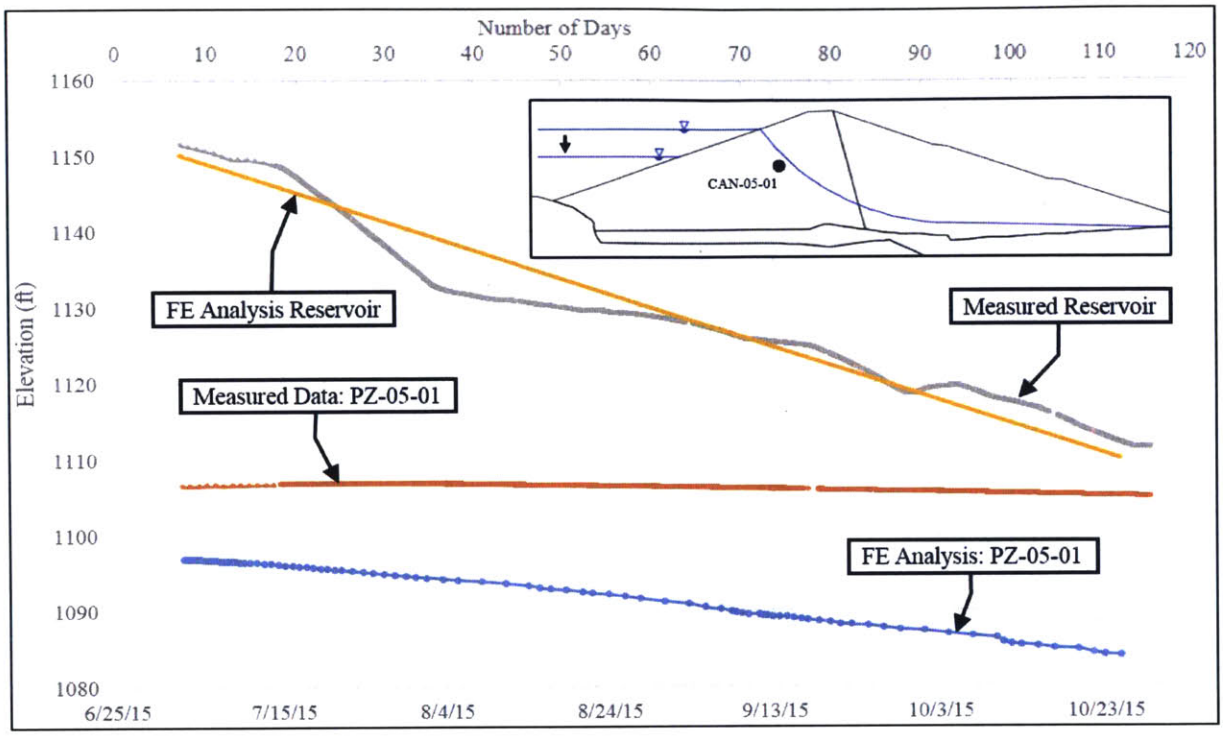

Figure 6.1: Piezometric head values at CAN-05-01 from proposed analysis and Hover (2016).

6.2 Recommendations for Future Work

This thesis considers the effects of time-dependency on slope stability after rapid drawdown (RDD) for a large embankment dam in central New York, using a commercially available finite element program, (PLAXIS 2D 2015™). Future work specific to this thesis could incorporate additional complexities within the assumed geology (i.e., adding rock fill to the slope or sub-layers within the glacial till) to evaluate a situation closer to that of real life and more realistic constitutive models of compacted fills such as those proposed by Berilgen (2007) and Pinyol et al. (2008).

References

ASDSO (2016). "Association of State Dam Safety Officials." ASDSO, 2016. 04 May 2016.

Berilgen, M. M. (2007). "Investigation of stability of slopes under drawdown conditions." *Computational Geotech.*, 34(2), 81–91. 2007.

Bishop, A. W. (1954). "The Use of Pore-pressure Coefficients in Practice." *Géotechnique*, 4(3), 148-152.

Bishop, A. W. (1955). "The Use of the Slip Circle in the Stability Analysis of Slopes." *Géotechnique*, 5(1), 7-17.

Brinkgreve R. B. J. and H. L. Bakker (1991) "Non-linear Finite Element Analysis of Safety Factors." Computer Methods and Advancements in Geomechanics. 1991.

Bush, G. W. (2003). December 17, 2003 Homeland Security Presidential Directive/Hspd-7: Critical Infrastructure Identification, Prioritization, and Protection. Washington, D.C.: White House Office of the Secretary.

Duncan, J. M., Wright, S. G., and Wong, K. S. (1990). "Slope stability during rapid drawdown," Seed Memorial Symposium Proceedings, Vol. 2, BiTech Publishers, Ltd., Vancouver, B.C., 235-272.

FERC (1978). Walter Bouldin Dam Failure and Reconstruction Report. Rep. no. DOE/FERC-0017. Washington: Federal Energy Regulatory Commission.

GZA (2005). Final Report for the [CV dam] and Reservoir. GZA GeoEnvironmental, Inc. Rep. Buffalo, NY.

Hover, W.H. (2016). Personal Communication. GZA GeoEnvironmental, Inc., Norwood, MA Feb. 2016.

MathWorks (2016). Matlab R2016b Graphics Reference Manual. 2016.

Morgenstern, N. (1963). "Stability Charts for Earth Slopes During Rapid Drawdown." *Géotechnique*, 13(2), 21-31.

Osnos, Evan. (2016). "Faust, China, and Nuclear Power," The New Yorker, Wednesday October 12, 2011. accessed: April 20, 2016.

Plaxis Bv. (2015). Plaxis 2D 2015 Reference Manual. Delft, The Netherlands., 2015.

Rush P. V. (2015). "[CV dam] Public Outreach Meetings." New York City Department of Environmental Protection. Deposit, NY. 23 July 2015. Address.

Skempton, A. W. (1954). "The Pore Pressure Coefficients A and B." *Géotechnique*, 4(4), 143-157.

Soren, J. (1963). The Ground-Water Resources of Delaware County, New York. Publication no. GW-50. Albany: USGS & NYWRC, 1963.

Spencer, E. (1967). "A Method of analysis of the Stability of Embankments Assuming Parallel Inter-Slice Forces". *Géotechnique*. 17(1), 11-26.

Pinyol, N. M., Alonso, E. E., and Olivella, S. (2008). "Rapid drawdown in slopes and embankments." Water Res. Res., 44(5), W00D03. 2008.

USGS (1963). The Ground-Water Resources of Delaware County, New York. Bulletin GW-50, U.S. Geologic Survey. Albany, N.Y. 1963.

USACE (2003). Slope Stability Engineering Manual. Washington, D.C.: Dept. of the Army, Corps of Engineers, Office of the Chief of Engineers, 2003. EM 1110-2-1902.

USACE (2014). Engineering and Design: Safety of Dams Policies and Procedures. Washington, D.C.: Dept. of the Army, Corps of Engineers, Office of the Chief of Engineers. 2014. ER 1110-2-1156.

Vandenberge, Daniel R. (2014). "Total Stress Rapid Drawdown Analysis of the Pilarcitos Dam Failure Using the Finite Element Method." Front. Struct. Civ. Eng. Frontiers of Structural and Civil Engineering 8.2 (2014): 115-23.

Vandenberge, Daniel R., J. Michael Duncan, and Thomas L. Brandon. (2015). "Limitations of Transient Seepage Analyses for Calculating Pore Pressures during External Water Level Changes." J. Geotech. Geoenviron. Eng. Journal of Geotechnical and Geoenvironmental Engineering 141.5 (2015): 04015005.

Vandenberge, Daniel R., J. Michael Duncan, and Thomas L. Brandon. (2013). "Rapid Drawdown Analysis using Strength Reduction." Proceedings of the 18th International Conference on Soil Mechanics and Geotechnical Engineering. Paris 2013.

Whitman, R. (2000). "Organizing and Evaluating Uncertainty in Geotechnical Engineering." ASCE J. Geotech. Geoenviron. Eng., 126(7), 583-593.

Appendix A: Steady Flow Calibration FE Model Output Results

Table A 1: Model identification by model number.

By Model No.		Impervious Fill, K1 (ft/day)						
		3E-2	3E-3	3E-4	3E-5	3E-6	3E-7	3E-8
Semi-pervious Fill, K2 (ft/day)	3E+2	1	6	11	16	21	26	33
	3E+1	2	7	12	17	22	27	34
	3E 0	3	8	13	18	23	28	35
	3E-1	4	9	14	19	24	29	36
	3E-2	5	10	15	20	25	30	37
	3E-3	40	41	42	43	44	31	38
	3E-4	45	46	47	48	49	32	39
	3E-5	50	51	52	53	54	55	56
	3E-6	57	58	59	60	61	62	63

Table A 2: Summary of Least Squared Error results.

By LSE Value		Impervious Fill, K1 (ft/day)						
		3E-2	3E-3	3E-4	3E-5	3E-6	3E-7	3E-8
Semi-pervious Fill K2 (ft/day)	3E+2	3041	922	2677	3705	3866	3850	3805
	3E+1	2940	853	2632	3790	4005	4306	3851
	3E 0	2850	852	2522	4164	4799	4511	22401
	3E-1	2644	829	2336	4088	4063	9904	8119
	3E-2	5186	721	2350	4271	4063	4914	4301
	3E-3	7386	713	2338	4451	4908	3844	3769
	3E-4	7447	745	2350	4904	5111	4690	9002
	3E-5	7443	856	2335	4554	4462	7245	8927
	3E-6	7446	993	2327	6297	8651	4858	26720

Table A 3: Breakdown of Least Squared Error results for Models 1 and 2.

			1			2		
Boring	**Point**	**Field Data (ft)**	**Head (ft)**	**Δ (ft)**	**Δ^2 (ft^2)**	**Head (ft)**	**Δ (ft)**	**Δ^2 (ft^2)**
CAN-05	PZ-1	1103.8	1112.1	-8.3	68.9	1111.8	-8.0	63.4
CAN-05	PZ-2	1064.3	1103.6	-39.3	1541.0	1103.1	-38.8	1505.0
CAN-01	PZ-1	1033.5	1064.2	-30.7	940.3	1063.6	-30.1	903.8
CAN-02	PZ-1	1025.0	1004.2	20.8	431.1	1004.7	20.3	410.8
CAN-02	PZ-2	1011.9	1004.2	7.7	59.7	1004.4	7.5	56.5
Sum of Squared Error					3041			2940

Table A 4: Breakdown of Least Squared Error results for Models 3 and 4.

			3			4		
Boring	**Point**	**Field Data (ft)**	**Head (ft)**	**Δ (ft)**	**Δ^2 (ft^2)**	**Head (ft)**	**Δ (ft)**	**Δ^2 (ft^2)**
CAN-05	PZ-1	1103.8	1111.8	-8.0	63.6	1111.8	-8.0	64.6
CAN-05	PZ-2	1064.3	1103.1	-38.8	1504.6	1103.2	-38.9	1515.4
CAN-01	PZ-1	1033.5	1063.2	-29.7	883.7	1063.6	-30.1	908.6
CAN-02	PZ-1	1025.0	1006.2	18.8	355.1	1012.6	12.4	154.9
CAN-02	PZ-2	1011.9	1005.3	6.6	43.0	1012.4	-0.5	0.2
Sum of Squared Error					2850			2644

Table A 5: Breakdown of Least Squared Error results for Models 5 and 6.

			5			6		
Boring	**Point**	**Field Data (ft)**	**Head (ft)**	**Δ (ft)**	**Δ^2 (ft^2)**	**Head (ft)**	**Δ (ft)**	**Δ^2 (ft^2)**
CAN-05	PZ-1	1103.8	1116.3	-12.5	155.6	1097.6	6.2	39.0
CAN-05	PZ-2	1064.3	1109.4	-45.1	2037.7	1078.6	-14.3	204.1
CAN-01	PZ-1	1033.5	1076.7	-43.2	1868.3	1043.7	-10.2	104.7
CAN-02	PZ-1	1025.0	1042.5	-17.5	305.5	1002.8	22.2	491.6
CAN-02	PZ-2	1011.9	1040.5	-28.6	819.3	1002.8	9.1	82.4
Sum of Squared Error					5186			922

Table A 6: Breakdown of Least Squared Error results for Models 7 and 8.

			7			8		
Boring	**Point**	**Field Data (ft)**	**Head (ft)**	**Δ (ft)**	**Δ^2 (ft^2)**	**Head (ft)**	**Δ (ft)**	**Δ^2 (ft^2)**
CAN-05	PZ-1	1103.8	1097.7	6.1	36.9	1097.6	6.2	37.8
CAN-05	PZ-2	1064.3	1078.8	-14.5	211.6	1078.8	-14.5	209.1
CAN-01	PZ-1	1033.5	1044.1	-10.6	112.4	1044.0	-10.5	109.6
CAN-02	PZ-1	1025.0	1004.2	20.8	432.9	1004.2	20.8	434.6
CAN-02	PZ-2	1011.9	1004.2	7.7	59.5	1004.1	7.8	60.5
Sum of Squared Error					853			852

Table A 7: Breakdown of Least Squared Error results for Models 9 and 10.

			9			10		
Boring	**Point**	**Field Data (ft)**	**Head (ft)**	**Δ (ft)**	**Δ^2 (ft^2)**	**Head (ft)**	**Δ (ft)**	**Δ^2 (ft^2)**
CAN-05	PZ-1	1103.8	1097.8	6.0	35.9	1098.4	5.4	28.8
CAN-05	PZ-2	1064.3	1079.1	-14.8	217.6	1080.1	-15.8	251.1
CAN-01	PZ-1	1033.5	1044.4	-10.9	119.7	1046.0	-12.5	157.3
CAN-02	PZ-1	1025.0	1004.9	20.1	404.8	1008.6	16.4	270.3
CAN-02	PZ-2	1011.9	1004.7	7.2	51.2	1008.3	3.6	13.1
Sum of Squared Error					829			721

Table A 8: Breakdown of Least Squared Error results for Models 11 and 12.

			11			12		
Boring	**Point**	**Field Data (ft)**	**Head (ft)**	**Δ (ft)**	**Δ^2 (ft^2)**	**Head (ft)**	**Δ (ft)**	**Δ^2 (ft^2)**
CAN-05	PZ-1	1103.8	1076.9	26.9	726.2	1077.6	26.2	684.3
CAN-05	PZ-2	1064.3	1038.0	26.3	689.1	1038.1	26.2	688.8
CAN-01	PZ-1	1033.5	1014.3	19.2	369.4	1014.1	19.4	377.8
CAN-02	PZ-1	1025.0	998.4	26.6	709.2	998.5	26.5	700.8
CAN-02	PZ-2	1011.9	998.4	13.5	183.4	998.5	13.4	180.1
Sum of Squared Error					2677			2632

Table A 9: Breakdown of Least Squared Error results for Models 13 and 14.

			13			14		
Boring	**Point**	**Field Data (ft)**	**Head (ft)**	**Δ (ft)**	**Δ^2 (ft^2)**	**Head (ft)**	**Δ (ft)**	**Δ^2 (ft^2)**
CAN-05	PZ-1	1103.8	1077.7	26.1	680.7	1077.0	26.8	717.1
CAN-05	PZ-2	1064.3	1038.2	26.1	681.4	1038.8	25.5	648.5
CAN-01	PZ-1	1033.5	1014.2	19.3	370.7	1015.0	18.5	343.3
CAN-02	PZ-1	1025.0	999.8	25.2	636.1	1002.0	23.0	528.3
CAN-02	PZ-2	1011.9	999.5	12.4	152.9	1001.9	10.0	99.3
Sum of Squared Error					2522			2336

Table A 10: Breakdown of Least Squared Error results for Models 15 and 16.

			15			16		
Boring	**Point**	**Field Data (ft)**	**Head (ft)**	**Δ (ft)**	**Δ^2 (ft^2)**	**Head (ft)**	**Δ (ft)**	**Δ^2 (ft^2)**
CAN-05	PZ-1	1103.8	1077.1	26.7	712.5	1074.1	29.7	880.0
CAN-05	PZ-2	1064.3	1039.2	25.1	631.2	1023.1	41.2	1700.4
CAN-01	PZ-1	1033.5	1015.3	18.2	330.4	1008.5	25.0	622.6
CAN-02	PZ-1	1025.0	1001.3	23.7	559.8	1004.0	21.0	439.9
CAN-02	PZ-2	1011.9	1001.1	10.8	116.3	1004.0	7.9	62.1
Sum of Squared Error					2350			3705

Table A 11: Breakdown of Least Squared Error results for Models 17 and 18.

			17			18		
Boring	**Point**	**Field Data (ft)**	**Head (ft)**	**Δ (ft)**	**Δ^2 (ft^2)**	**Head (ft)**	**Δ (ft)**	**Δ^2 (ft^2)**
CAN-05	PZ-1	1103.8	1073.5	30.3	917.6	1073.3	30.5	929.6
CAN-05	PZ-2	1064.3	1022.6	41.7	1740.6	1019.3	45.0	2029.4
CAN-01	PZ-1	1033.5	1008.5	25.0	625.9	1008.6	24.9	619.1
CAN-02	PZ-1	1025.0	1004.0	21.0	442.6	1002.6	22.4	499.7
CAN-02	PZ-2	1011.9	1004.0	7.9	63.1	1002.6	9.3	86.3
Sum of Squared Error					3790			4164

Table A 12: Breakdown of Least Squared Error results for Models 19 and 20.

			19			20		
Boring	**Point**	**Field Data (ft)**	**Head (ft)**	**Δ (ft)**	**Δ^2 (ft^2)**	**Head (ft)**	**Δ (ft)**	**Δ^2 (ft^2)**
CAN-05	PZ-1	1103.8	1074.0	29.8	886.0	1073.1	30.7	944.9
CAN-05	PZ-2	1064.3	1021.5	42.8	1830.5	1022.8	41.5	1726.3
CAN-01	PZ-1	1033.5	1007.3	26.2	686.9	1012.1	21.4	456.5
CAN-02	PZ-1	1025.0	1001.2	23.8	567.8	995.6	29.4	862.6
CAN-02	PZ-2	1011.9	1001.1	10.8	116.8	995.1	16.8	281.2
Sum of Squared Error					4088			4271

Table A 13: Breakdown of Least Squared Error results for Models 21 and 22.

			21			22		
Boring	**Point**	**Field Data (ft)**	**Head (ft)**	**Δ (ft)**	**Δ^2 (ft^2)**	**Head (ft)**	**Δ (ft)**	**Δ^2 (ft^2)**
CAN-05	PZ-1	1103.8	1073.6	30.2	914.5	1074.2	29.6	873.9
CAN-05	PZ-2	1064.3	1022.1	42.2	1784.2	1020.0	44.3	1962.9
CAN-01	PZ-1	1033.5	1007.7	25.8	665.0	1007.8	25.7	662.3
CAN-02	PZ-1	1025.0	1004.0	21.0	440.0	1004.0	21.0	442.8
CAN-02	PZ-2	1011.9	1004.0	7.9	62.1	1003.9	8.0	63.2
Sum of Squared Error					3866			4005

Table A 14: Breakdown of Least Squared Error results for Models 23 and 24.

			23			24		
Boring	**Point**	**Field Data (ft)**	**Head (ft)**	**Δ (ft)**	**Δ^2 (ft^2)**	**Head (ft)**	**Δ (ft)**	**Δ^2 (ft^2)**
CAN-05	PZ-1	1103.8	1063.8	40.0	1596.0	1074.8	29.0	840.2
CAN-05	PZ-2	1064.3	1021.1	43.2	1863.1	1023.0	41.3	1707.3
CAN-01	PZ-1	1033.5	1006.9	26.6	709.6	1008.2	25.3	640.6
CAN-02	PZ-1	1025.0	1002.0	23.0	529.9	998.7	26.3	691.2
CAN-02	PZ-2	1011.9	1001.9	10.0	99.8	998.3	13.6	183.9
Sum of Squared Error					4799			4063

Table A 15: Breakdown of Least Squared Error results for Models 25 and 26.

			25			26		
Boring	**Point**	**Field Data (ft)**	**Head (ft)**	**Δ (ft)**	**Δ^2 (ft^2)**	**Head (ft)**	**Δ (ft)**	**Δ^2 (ft^2)**
CAN-05	PZ-1	1103.8	1075.1	28.7	821.9	1073.4	30.4	927.2
CAN-05	PZ-2	1064.3	1022.7	41.6	1729.2	1022.5	41.8	1750.4
CAN-01	PZ-1	1033.5	1015.1	18.4	338.0	1007.6	25.9	670.6
CAN-02	PZ-1	1025.0	995.3	29.7	879.4	1004.0	21.0	439.9
CAN-02	PZ-2	1011.9	994.7	17.2	295.1	1004.0	7.9	62.1
Sum of Squared Error					4063			3850

Table A 16: Breakdown of Least Squared Error results for Models 27 and 28.

			27			28		
Boring	**Point**	**Field Data (ft)**	**Head (ft)**	**Δ (ft)**	**Δ^2 (ft^2)**	**Head (ft)**	**Δ (ft)**	**Δ^2 (ft^2)**
CAN-05	PZ-1	1103.8	1068.0	35.8	1282.5	1066.0	37.8	1431.4
CAN-05	PZ-2	1064.3	1021.3	43.0	1847.8	1022.9	41.4	1715.4
CAN-01	PZ-1	1033.5	1007.6	25.9	669.3	1006.5	27.0	730.8
CAN-02	PZ-1	1025.0	1003.9	21.1	443.4	1001.9	23.1	532.7
CAN-02	PZ-2	1011.9	1003.9	8.0	63.4	1001.8	10.1	101.1
Sum of Squared Error					4306			4511

Table A 17: Breakdown of Least Squared Error results for Models 29 and 30.

			29			30		
Boring	**Point**	**Field Data (ft)**	**Head (ft)**	**Δ (ft)**	**Δ^2 (ft^2)**	**Head (ft)**	**Δ (ft)**	**Δ^2 (ft^2)**
CAN-05	PZ-1	1103.8	1037.9	65.9	4342.4	1060.8	43.0	1852.0
CAN-05	PZ-2	1064.3	1001.2	63.1	3986.2	1025.3	39.0	1524.4
CAN-01	PZ-1	1033.5	1007.0	26.5	701.1	1015.1	18.4	337.2
CAN-02	PZ-1	1025.0	998.7	26.3	690.3	995.0	30.0	897.3
CAN-02	PZ-2	1011.9	998.3	13.6	184.0	994.5	17.4	302.6
Sum of Squared Error					9904			4914

Table A 18: Breakdown of Least Squared Error results for Models 31 and 32.

			31			32		
Boring	**Point**	**Field Data (ft)**	**Head (ft)**	**Δ (ft)**	**Δ^2 (ft^2)**	**Head (ft)**	**Δ (ft)**	**Δ^2 (ft^2)**
CAN-05	PZ-1	1103.8	1090.2	13.6	186.1	1083.5	20.3	413.4
CAN-05	PZ-2	1064.3	1028.1	36.2	1307.1	1034.7	29.6	876.8
CAN-01	PZ-1	1033.5	1010.5	23.0	528.3	1001.1	32.4	1051.6
CAN-02	PZ-1	1025.0	989.2	35.8	1282.8	983.6	41.4	1718.0
CAN-02	PZ-2	1011.9	988.7	23.2	539.5	986.8	25.1	630.7
Sum of Squared Error					3844			4690

Table A 19: Breakdown of Least Squared Error results for Models 33 and 34.

			33			34		
Boring	**Point**	**Field Data (ft)**	**Head (ft)**	**Δ (ft)**	**Δ^2 (ft^2)**	**Head (ft)**	**Δ (ft)**	**Δ^2 (ft^2)**
CAN-05	PZ-1	1103.8	1074.1	29.7	882.5	1073.5	30.3	919.0
CAN-05	PZ-2	1064.3	1022.6	41.7	1741.8	1022.4	41.9	1754.9
CAN-01	PZ-1	1033.5	1007.4	26.1	678.8	1007.6	25.9	670.6
CAN-02	PZ-1	1025.0	1004.0	21.0	439.9	1004.0	21.0	442.9
CAN-02	PZ-2	1011.9	1004.0	7.9	62.1	1003.9	8.0	63.2
Sum of Squared Error					3805			3851

Table A 20: Breakdown of Least Squared Error results for Models 35 and 36.

			35			36		
Boring	**Point**	**Field Data (ft)**	**Head (ft)**	**Δ (ft)**	**Δ^2 (ft^2)**	**Head (ft)**	**Δ (ft)**	**Δ^2 (ft^2)**
CAN-05	PZ-1	1103.8	1075.4	28.4	805.1	1046.8	57.0	3253.5
CAN-05	PZ-2	1064.3	1022.8	41.5	1724.8	1008.4	55.9	3119.6
CAN-01	PZ-1	1033.5	959.0	74.5	5545.0	1004.0	29.5	871.2
CAN-02	PZ-1	1025.0	934.1	90.9	8268.5	998.7	26.3	691.1
CAN-02	PZ-2	1011.9	934.1	77.8	6058.0	998.3	13.6	183.9
Sum of Squared Error					22401			8119

Table A 21: Breakdown of Least Squared Error results for Models 37 and 38.

			37			38		
Boring	**Point**	**Field Data (ft)**	**Head (ft)**	**Δ (ft)**	**Δ^2 (ft^2)**	**Head (ft)**	**Δ (ft)**	**Δ^2 (ft^2)**
CAN-05	PZ-1	1103.8	1074.6	29.2	850.5	1082.1	21.7	472.9
CAN-05	PZ-2	1064.3	1023.3	41.0	1683.3	1033.7	30.6	937.2
CAN-01	PZ-1	1033.5	1009.9	23.6	557.2	1010.7	22.8	518.5
CAN-02	PZ-1	1025.0	994.9	30.1	907.1	989.0	36.0	1299.6
CAN-02	PZ-2	1011.9	994.5	17.4	302.8	988.6	23.3	540.6
Sum of Squared Error					4301			3769

Table A 22: Breakdown of Least Squared Error results for Models 39 and 40.

			39			40		
Boring	**Point**	**Field Data (ft)**	**Head (ft)**	**Δ (ft)**	**Δ^2 (ft^2)**	**Head (ft)**	**Δ (ft)**	**Δ^2 (ft^2)**
CAN-05	PZ-1	1103.8	1073.9	29.9	896.2	1122.3	-18.5	341.8
CAN-05	PZ-2	1064.3	1023.9	40.4	1634.1	1116.7	-52.4	2743.3
CAN-01	PZ-1	1033.5	992.5	41.0	1682.7	1089.6	-56.1	3150.3
CAN-02	PZ-1	1025.0	969.2	55.8	3110.1	1046.2	-21.2	448.3
CAN-02	PZ-2	1011.9	970.9	41.0	1679.4	1038.4	-26.5	702.0
Sum of Squared Error					9002			7386

Table A 23: Breakdown of Least Squared Error results for Models 41 and 42.

			41			42		
Boring	**Point**	**Field Data (ft)**	**Head (ft)**	**Δ (ft)**	**Δ^2 (ft^2)**	**Head (ft)**	**Δ (ft)**	**Δ^2 (ft^2)**
CAN-05	PZ-1	1103.8	1099.5	4.3	18.5	1077.1	26.7	712.2
CAN-05	PZ-2	1064.3	1081.9	-17.6	308.7	1039.4	24.9	621.1
CAN-01	PZ-1	1033.5	1048.7	-15.2	231.7	1015.7	17.8	317.8
CAN-02	PZ-1	1025.0	1012.6	12.4	154.2	1001.3	23.7	563.4
CAN-02	PZ-2	1011.9	1011.5	0.4	0.1	1000.8	11.1	123.7
Sum of Squared Error					713			2338

Table A 24: Breakdown of Least Squared Error results for Models 43 and 44.

			43			44		
Boring	**Point**	**Field Data (ft)**	**Head (ft)**	**Δ (ft)**	**Δ^2 (ft^2)**	**Head (ft)**	**Δ (ft)**	**Δ^2 (ft^2)**
CAN-05	PZ-1	1103.8	1073.3	30.5	931.3	1075.3	28.5	812.0
CAN-05	PZ-2	1064.3	1022.7	41.6	1726.8	1022.6	41.7	1736.9
CAN-01	PZ-1	1033.5	1010.1	23.4	545.6	1009.0	24.5	601.9
CAN-02	PZ-1	1025.0	995.7	29.3	856.6	989.4	35.6	1265.8
CAN-02	PZ-2	1011.9	992.1	19.8	390.4	989.7	22.2	491.0
Sum of Squared Error					4451			4908

Table A 25: Breakdown of Least Squared Error results for Models 45 and 46.

			45			46		
Boring	**Point**	**Field Data (ft)**	**Head (ft)**	**Δ (ft)**	**Δ^2 (ft^2)**	**Head (ft)**	**Δ (ft)**	**Δ^2 (ft^2)**
CAN-05	PZ-1	1103.8	1123.8	-20.0	401.2	1099.9	3.9	15.5
CAN-05	PZ-2	1064.3	1118.4	-54.1	2924.9	1082.5	-18.2	330.9
CAN-01	PZ-1	1033.5	1092.4	-58.9	3468.6	1050.0	-16.5	272.1
CAN-02	PZ-1	1025.0	1042.1	-17.1	291.3	1013.8	11.2	126.1
CAN-02	PZ-2	1011.9	1030.9	-19.0	361.3	1011.2	0.7	0.5
Sum of Squared Error					7447			745

Table A 26: Breakdown of Least Squared Error results for Models 47 and 48.

			47			48		
Boring	**Point**	**Field Data (ft)**	**Head (ft)**	**Δ (ft)**	**Δ^2 (ft^2)**	**Head (ft)**	**Δ (ft)**	**Δ^2 (ft^2)**
CAN-05	PZ-1	1103.8	1076.5	27.3	744.2	1074.4	29.4	867.1
CAN-05	PZ-2	1064.3	1039.2	25.1	630.4	1022.8	41.5	1724.1
CAN-01	PZ-1	1033.5	1016.0	17.5	305.5	1003.5	30.0	902.1
CAN-02	PZ-1	1025.0	1001.6	23.4	545.7	993.2	31.8	1009.3
CAN-02	PZ-2	1011.9	1000.7	11.2	124.4	991.9	20.0	401.5
Sum of Squared Error					2350			4904

Table A 27: Breakdown of Least Squared Error results for Model 49 and 50.

			49			50		
Boring	**Point**	**Field Data (ft)**	**Head (ft)**	**Δ (ft)**	**Δ^2 (ft^2)**	**Head (ft)**	**Δ (ft)**	**Δ^2 (ft^2)**
CAN-05	PZ-1	1103.8	1075.5	28.3	798.1	1124.0	-20.2	407.9
CAN-05	PZ-2	1064.3	1022.8	41.5	1722.4	1118.6	-54.3	2944.9
CAN-01	PZ-1	1033.5	1005.1	28.4	807.3	1092.7	-59.2	3504.4
CAN-02	PZ-1	1025.0	988.2	36.8	1354.8	1041.4	-16.4	268.7
CAN-02	PZ-2	1011.9	991.2	20.7	428.3	1029.7	-17.8	317.2
Sum of Squared Error					5111			7443

Table A 28: Breakdown of Least Squared Error results for Model 51 and 52.

			51			52		
Boring	**Point**	**Field Data (ft)**	**Head (ft)**	**Δ (ft)**	**Δ^2 (ft^2)**	**Head (ft)**	**Δ (ft)**	**Δ^2 (ft^2)**
CAN-05	PZ-1	1103.8	1093.0	10.8	117.2	1076.5	27.3	746.5
CAN-05	PZ-2	1064.3	1082.6	-18.3	336.2	1039.2	25.1	630.0
CAN-01	PZ-1	1033.5	1050.3	-16.8	281.1	1016.2	17.3	298.6
CAN-02	PZ-1	1025.0	1014.0	11.0	120.6	1001.9	23.1	535.5
CAN-02	PZ-2	1011.9	1011.1	0.8	0.6	1000.8	11.1	124.1
Sum of Squared Error					856			2335

Table A 29: Breakdown of Least Squared Error results for Model 53 and 54.

			53			54		
Boring	**Point**	**Field Data (ft)**	**Head (ft)**	**Δ (ft)**	**Δ^2 (ft^2)**	**Head (ft)**	**Δ (ft)**	**Δ^2 (ft^2)**
CAN-05	PZ-1	1103.8	1074.8	29.0	843.9	1075.8	28.0	784.4
CAN-05	PZ-2	1064.3	1022.8	41.5	1723.2	1031.3	33.0	1089.5
CAN-01	PZ-1	1033.5	1004.5	29.0	843.2	998.3	35.2	1236.0
CAN-02	PZ-1	1025.0	996.5	28.5	810.5	994.2	30.8	947.2
CAN-02	PZ-2	1011.9	993.6	18.3	333.3	991.8	20.1	405.1
Sum of Squared Error					4554			4462

Table A 30: Breakdown of Least Squared Error results for Model 55 and 55.

			55			56		
Boring	**Point**	**Field Data (ft)**	**Head (ft)**	**Δ (ft)**	**Δ^2 (ft^2)**	**Head (ft)**	**Δ (ft)**	**Δ^2 (ft^2)**
CAN-05	PZ-1	1103.8	1075.1	28.7	821.0	1075.1	28.7	821.8
CAN-05	PZ-2	1064.3	1022.3	42.0	1760.3	1024.7	39.6	1566.2
CAN-01	PZ-1	1033.5	980.4	53.1	2824.8	989.9	43.6	1903.5
CAN-02	PZ-1	1025.0	990.2	34.8	1211.6	970.0	55.0	3023.9
CAN-02	PZ-2	1011.9	986.9	25.0	627.2	971.8	40.1	1611.6
Sum of Squared Error					7245			8927

Table A 31: Breakdown of Least Squared Error results for Model 57 and 58.

			57			58		
Boring	**Point**	**Field Data (ft)**	**Head (ft)**	**Δ (ft)**	**Δ^2 (ft^2)**	**Head (ft)**	**Δ (ft)**	**Δ^2 (ft^2)**
CAN-05	PZ-1	1103.8	1124.0	-20.2	409.1	1086.9	16.9	284.7
CAN-05	PZ-2	1064.3	1118.6	-54.3	2948.0	1080.6	-16.3	266.5
CAN-01	PZ-1	1033.5	1092.7	-59.2	3509.4	1051.4	-17.9	321.5
CAN-02	PZ-1	1025.0	1041.3	-16.3	266.5	1014.1	10.9	119.9
CAN-02	PZ-2	1011.9	1029.6	-17.7	312.7	1011.1	0.8	0.6
Sum of Squared Error					7446			993

Table A 32: Breakdown of Least Squared Error results for Model 59 and 60.

			59			60		
Boring	**Point**	**Field Data (ft)**	**Head (ft)**	**Δ (ft)**	**Δ^2 (ft^2)**	**Head (ft)**	**Δ (ft)**	**Δ^2 (ft^2)**
CAN-05	PZ-1	1103.8	1076.5	27.3	747.6	1074.4	29.4	861.6
CAN-05	PZ-2	1064.3	1039.2	25.1	629.6	1022.7	41.6	1734.2
CAN-01	PZ-1	1033.5	1016.3	17.2	296.4	1000.4	33.1	1097.8
CAN-02	PZ-1	1025.0	1002.0	23.0	529.2	976.0	49.0	2396.6
CAN-02	PZ-2	1011.9	1000.8	11.1	123.8	997.5	14.4	206.6
Sum of Squared Error					2327			6297

Table A 33: Breakdown of Least Squared Error results for Model 61 and 62.

			61			62		
Boring	**Point**	**Field Data (ft)**	**Head (ft)**	**Δ (ft)**	**Δ^2 (ft^2)**	**Head (ft)**	**Δ (ft)**	**Δ^2 (ft^2)**
CAN-05	PZ-1	1103.8	1074.9	28.9	835.1	1082.1	21.7	470.0
CAN-05	PZ-2	1064.3	1023.0	41.3	1709.6	1044.6	19.7	386.6
CAN-01	PZ-1	1033.5	980.0	53.5	2867.4	984.9	48.6	2362.8
CAN-02	PZ-1	1025.0	970.1	54.9	3017.4	995.1	29.9	894.9
CAN-02	PZ-2	1011.9	997.0	14.9	221.7	984.6	27.3	743.2
Sum of Squared Error					8651			4858

Table A 34: Breakdown of Least Squared Error results for Model 63.

			63		
Boring	**Point**	**Field Data (ft)**	**Head (ft)**	**Δ (ft)**	**Δ^2 (ft^2)**
CAN-05	PZ-1	1103.8	1012.8	91.0	8277.9
CAN-05	PZ-2	1064.3	971.8	92.5	8558.1
CAN-01	PZ-1	1033.5	964.1	69.4	4810.1
CAN-02	PZ-1	1025.0	966.5	58.5	3417.2
CAN-02	PZ-2	1011.9	971.2	40.7	1656.7
Sum of Squared Error					26720

Appendix B: Instantaneous Drawdown FE Model Output Results

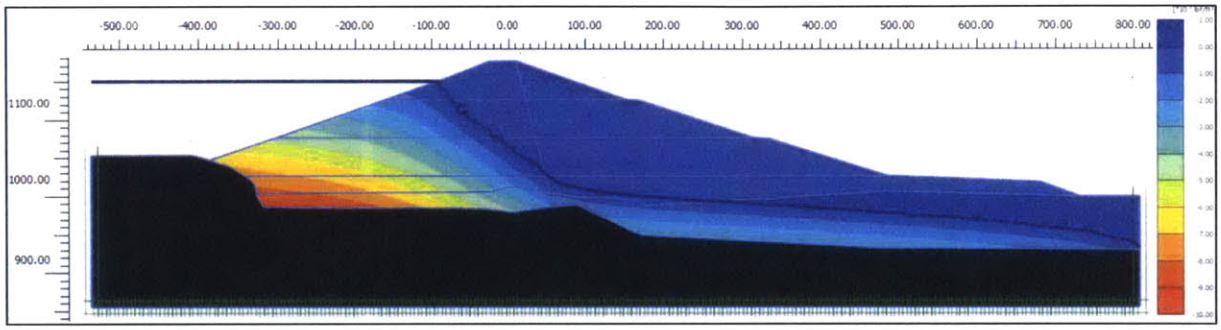

Figure B 1: Active pore pressure distribution for normal reservoir level, El. 1150 ft.

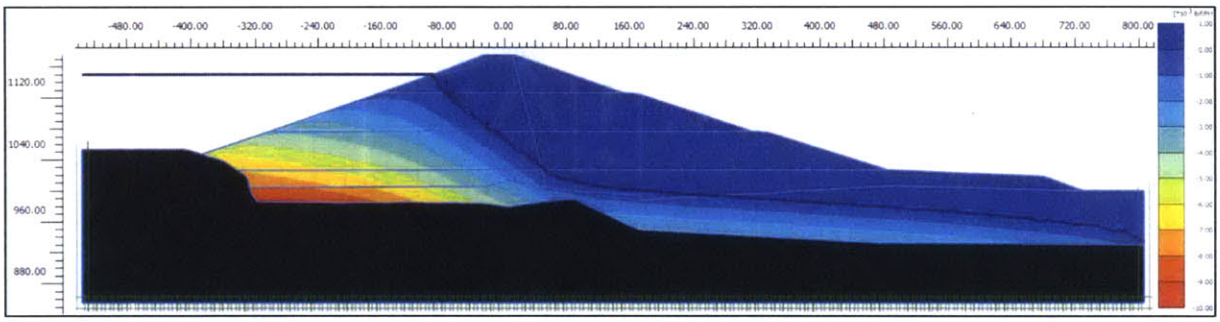

Figure B 2: Active pore pressure distribution for 20 ft instantaneous drawdown, El. 1130 ft.

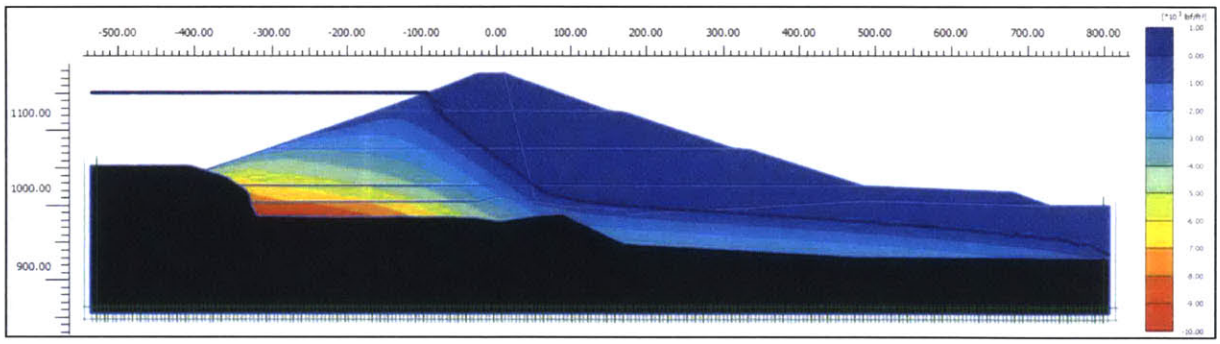

Figure B 3: Active pore pressure distribution for 40 ft instantaneous drawdown, El. 1110 ft.

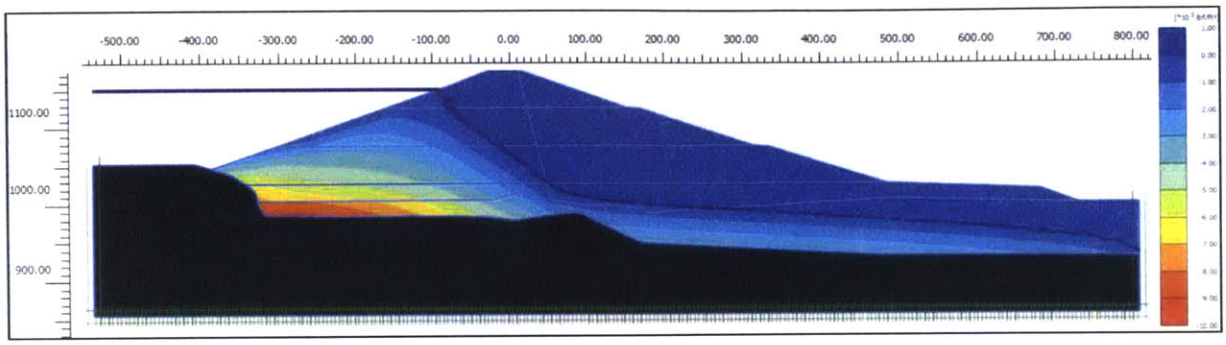

Figure B 4: Active pore pressure distribution for 60 ft instantaneous drawdown, El. 1090 ft.

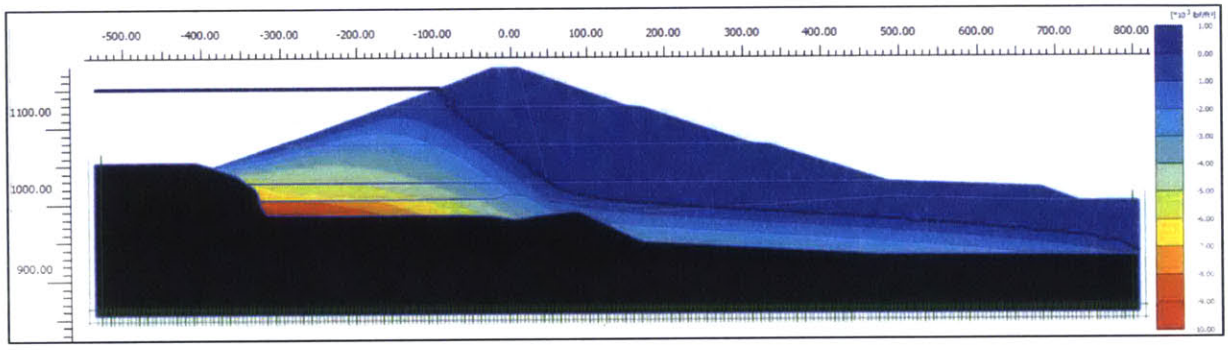

Figure B 5: Active pore pressure distribution for 80 ft instantaneous drawdown, El. 1070 ft.

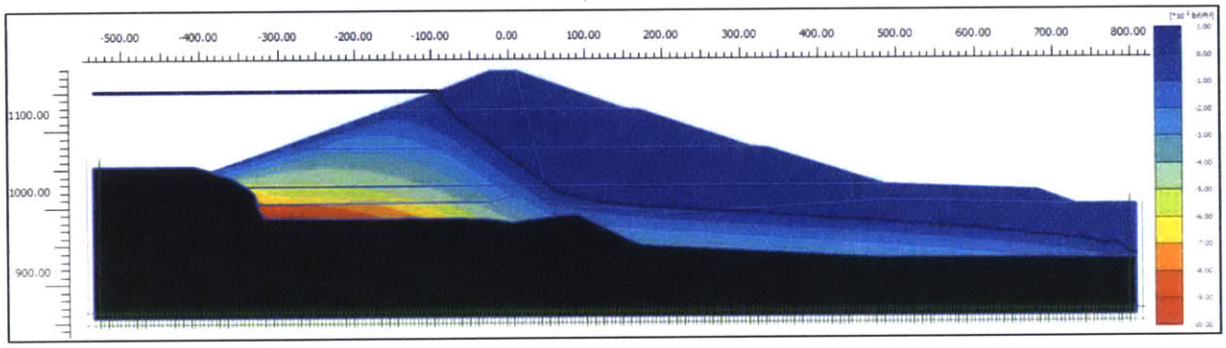

Figure B 6: Active pore pressure distribution for 97 ft instantaneous drawdown, El. 1053 ft.

Appendix C: Time-Dependent Drawdown FE Model Output Results

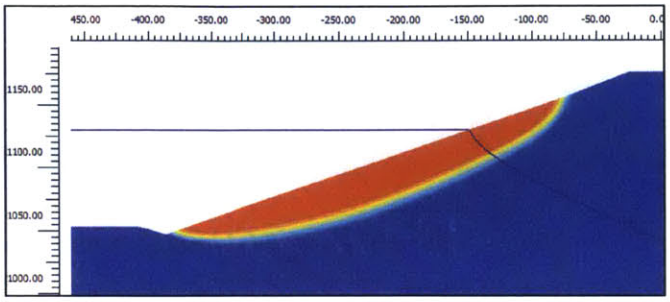

Figure C 1: Failure mechanism for 20 ft drawdown, 365 days.

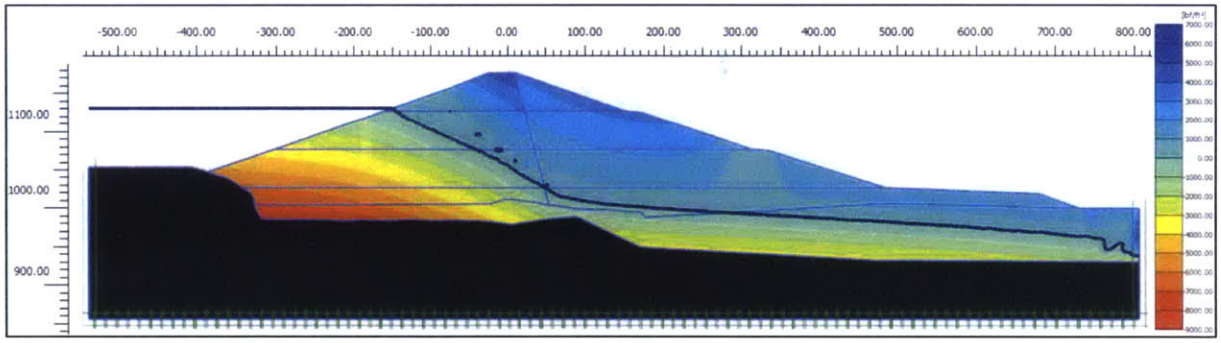

Figure C 2: Active pore pressure distribution for 20 ft drawdown, 365 days.

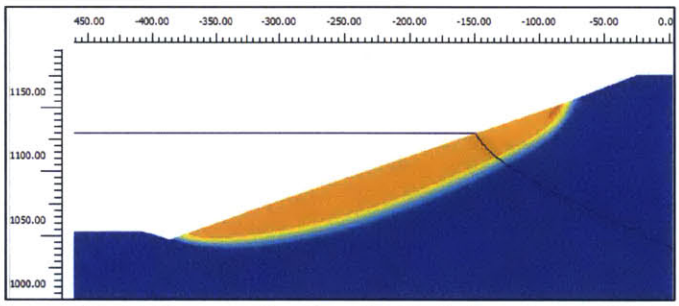

Figure C 3: Failure mechanism for 20 ft drawdown, 180 days.

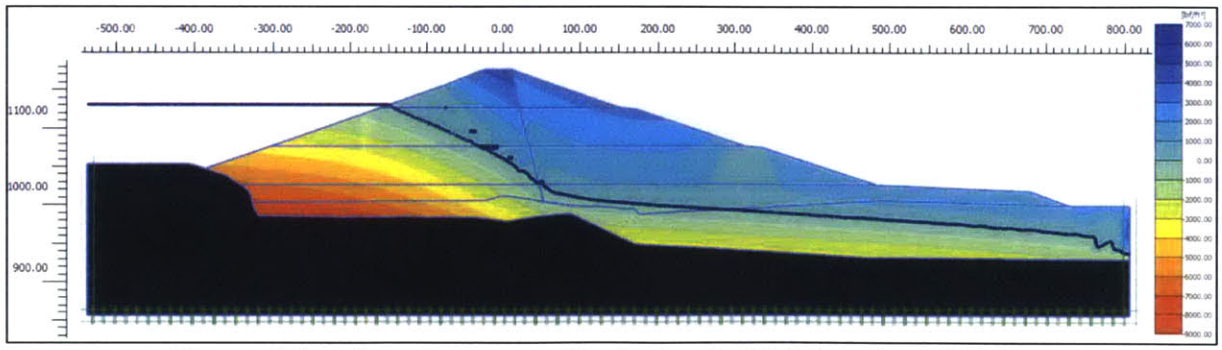

Figure C 4: Active pore pressure distribution for 20 ft drawdown, 180 days.

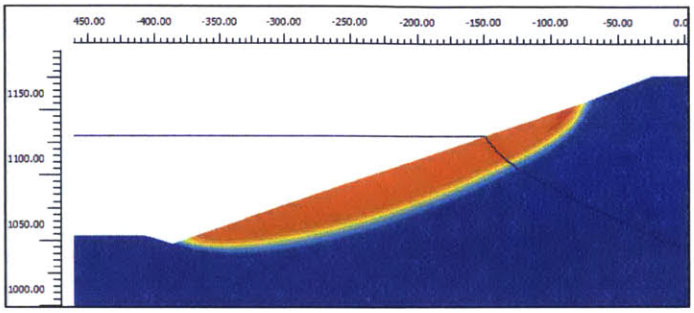

Figure C 5: Failure mechanism for 20 ft drawdown, 90 days.

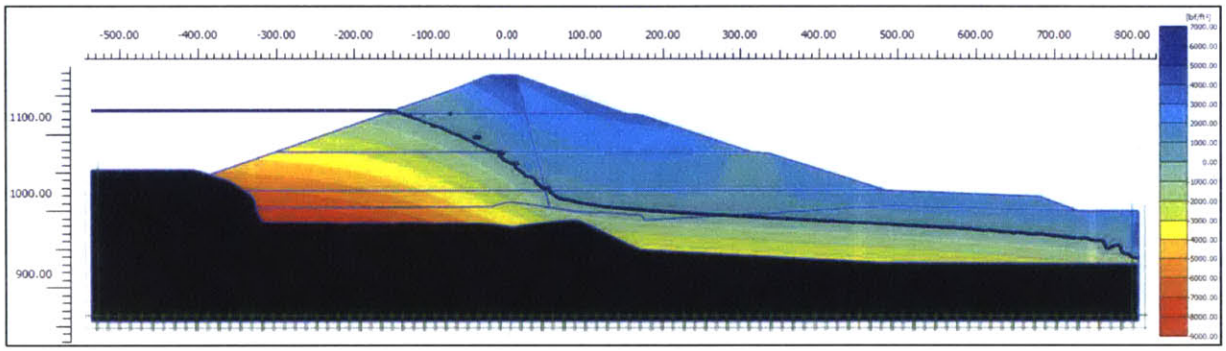

Figure C 6: Active pore pressure distribution for 20 ft drawdown, 90 days.

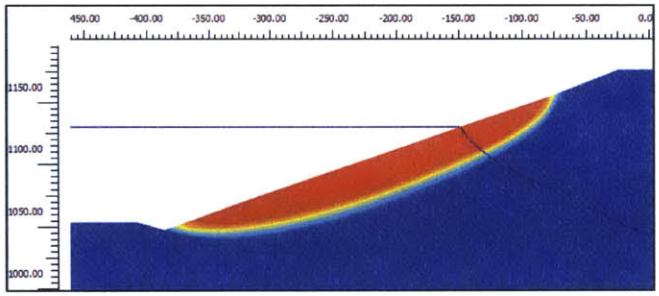

Figure C 7: Failure mechanism for 20 ft drawdown, 30 days.

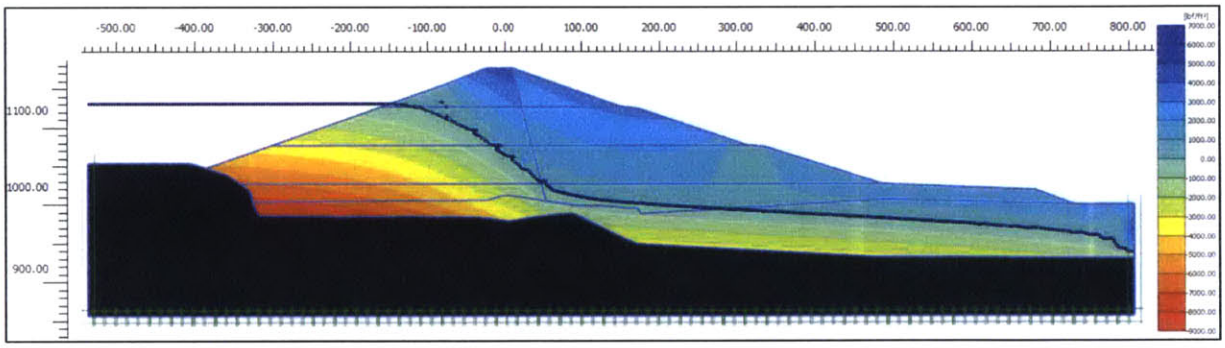

Figure C 8: Active pore pressure distribution for 20 ft drawdown, 30 days.

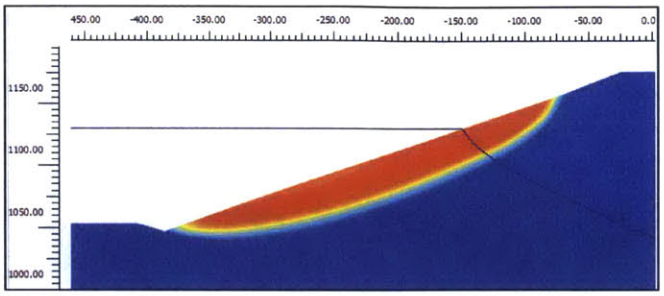

Figure C 9: Failure mechanism for 20 ft drawdown, 10 days.

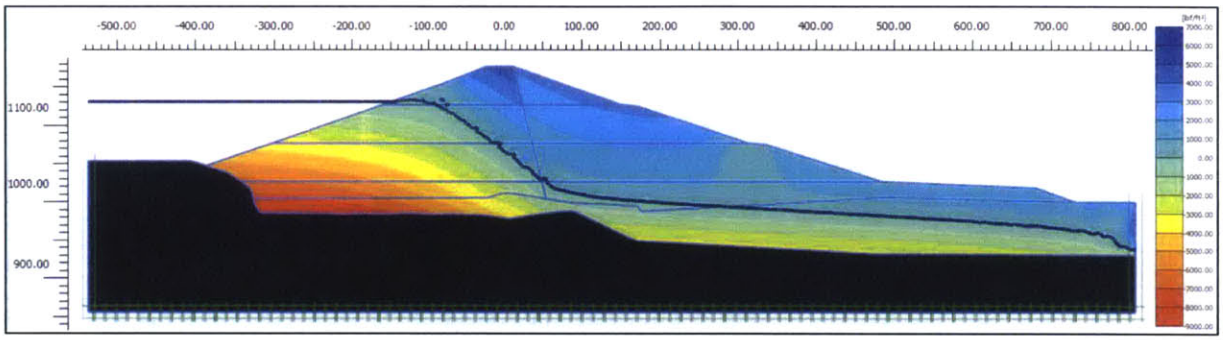

Figure C 10: Active pore pressure distribution for 20 ft drawdown, 10 days.

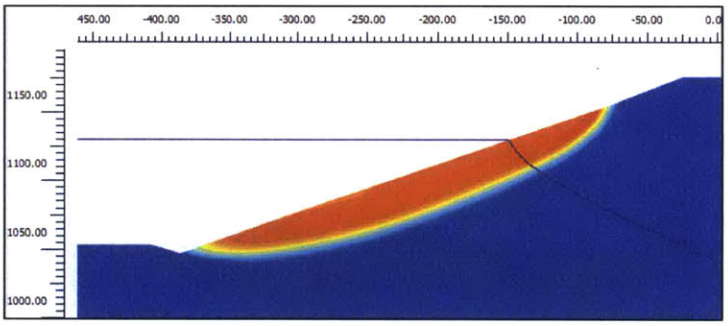

Figure C 11: Failure mechanism for 20 ft drawdown, 3 days.

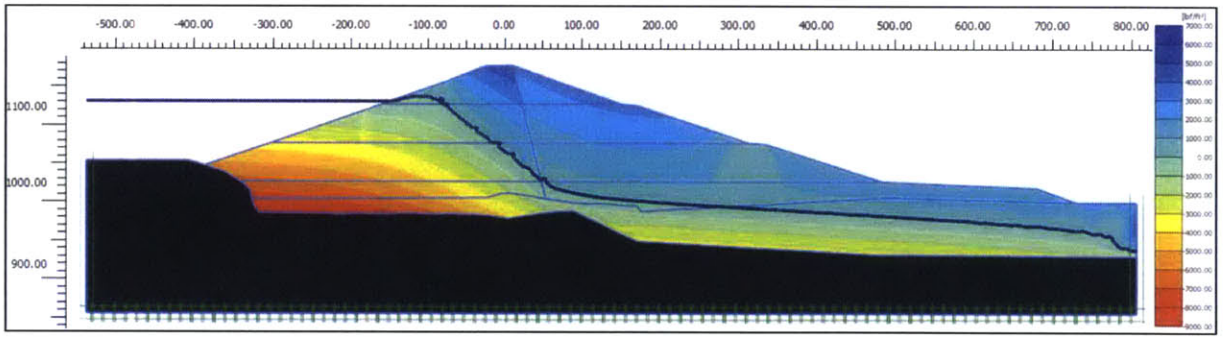

Figure C 12: Active pore pressure distribution for 20 ft drawdown, 3 days.

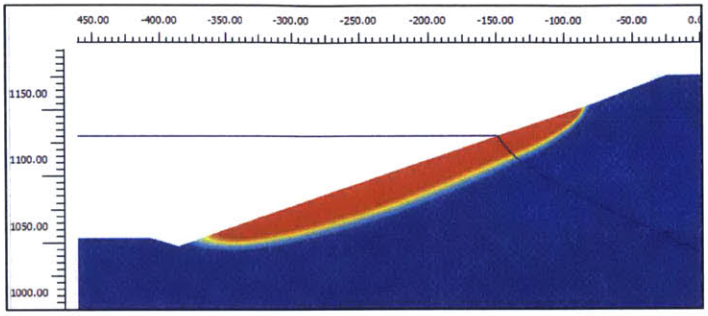

Figure C 13: Failure mechanism for 20 ft drawdown, 0.1 days.

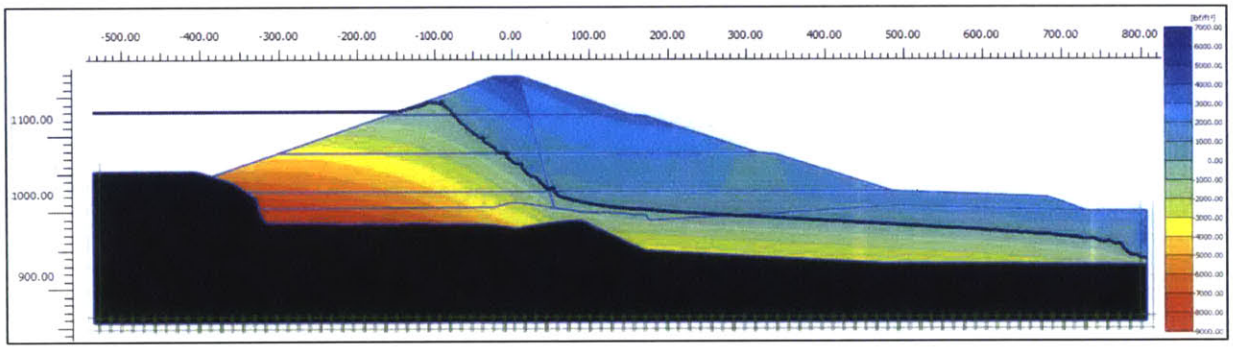

Figure C 14: Active pore pressure distribution for 20 ft drawdown, 0.1 days.

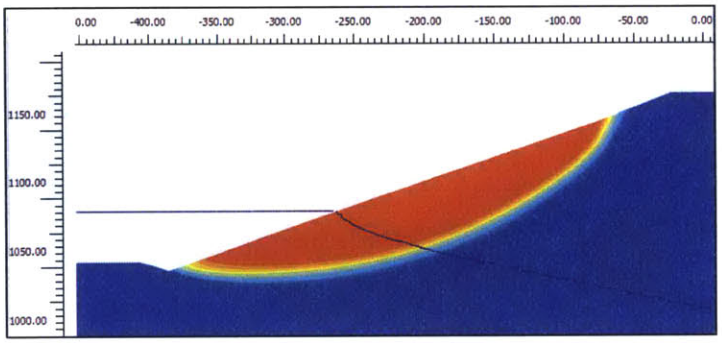

Figure C 15: Failure mechanism for 60 ft drawdown, 365 days.

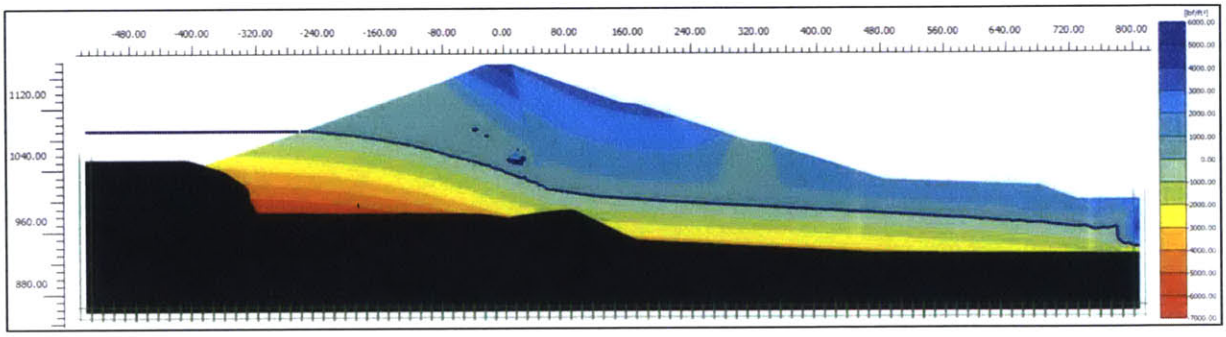

Figure C 16: Active pore pressure distribution for 60 ft drawdown, 365 days.

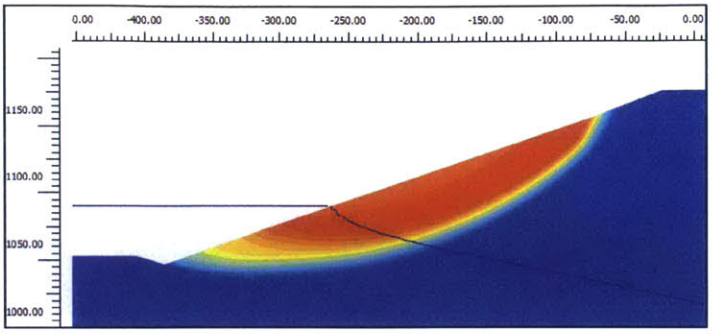

Figure C 17: Failure mechanism for 60 ft drawdown, 180 days.

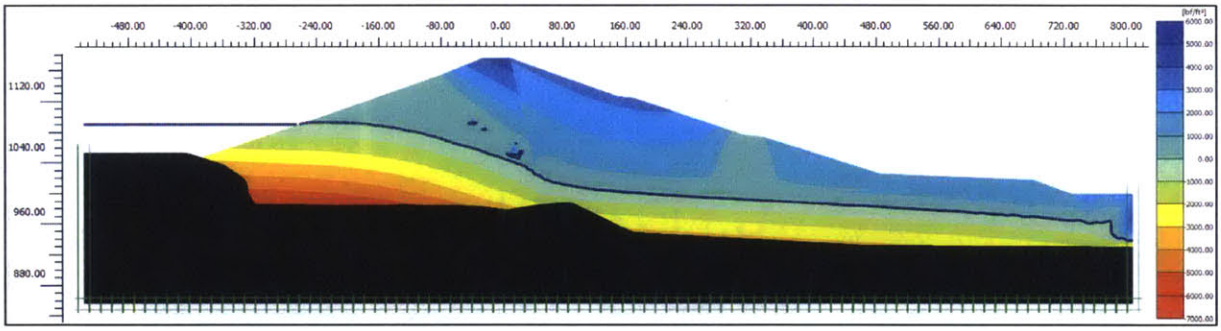

Figure C 18: Active pore pressure distribution for 60 ft drawdown, 180 days.

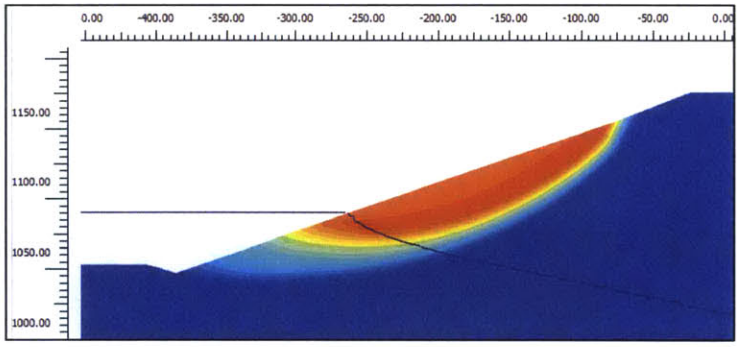

Figure C 19: Failure mechanism for 60 ft drawdown, 90 days.

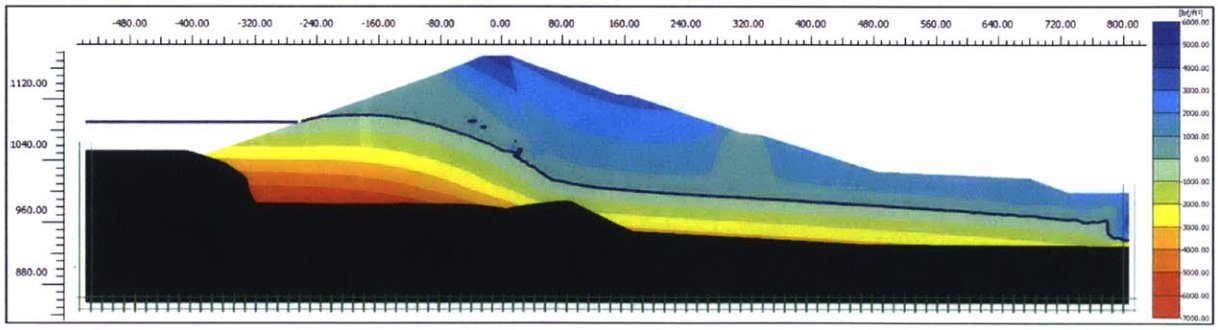

Figure C 20: Active pore pressure distribution for 60 ft drawdown, 90 days.

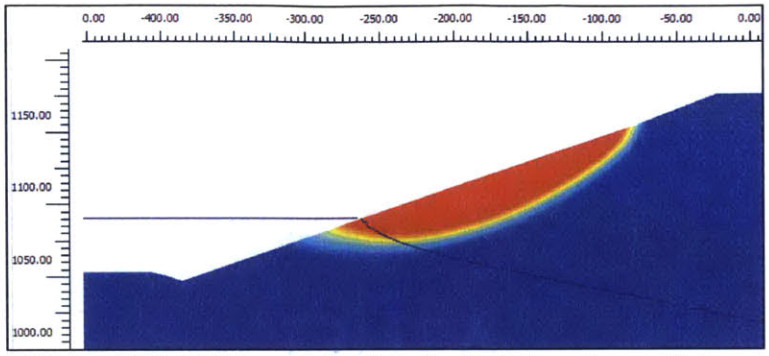

Figure C 21: Failure mechanism for 60 ft drawdown, 30 days.

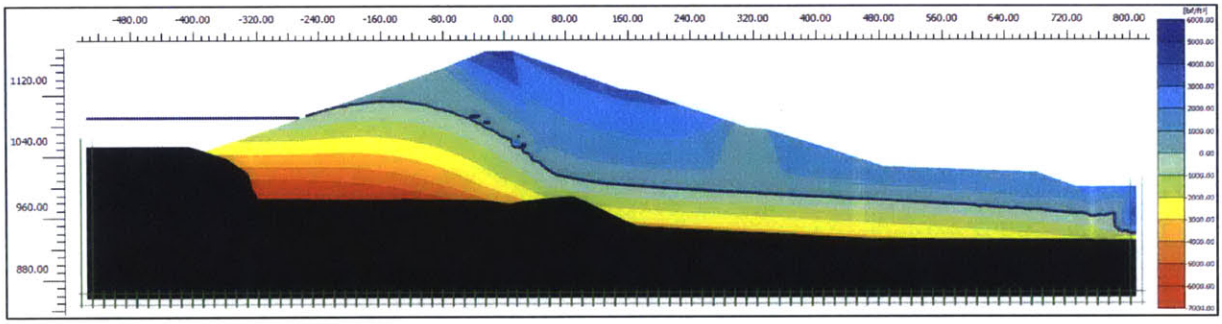

Figure C 22: Active pore pressure distribution for 60 ft drawdown, 30 days.

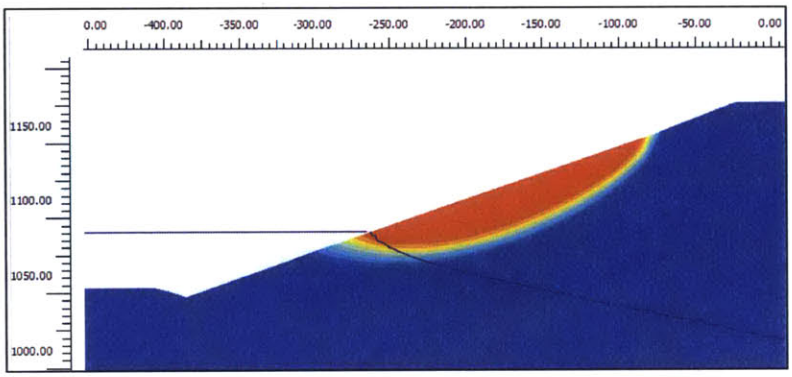

Figure C 23: Failure mechanism for 60 ft drawdown, 10 days.

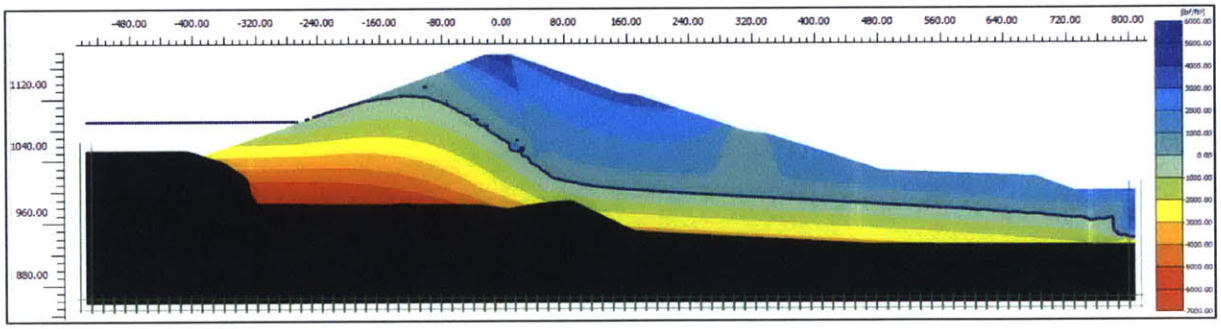

Figure C 24: Active pore pressure distribution for 60 ft drawdown, 10 days.

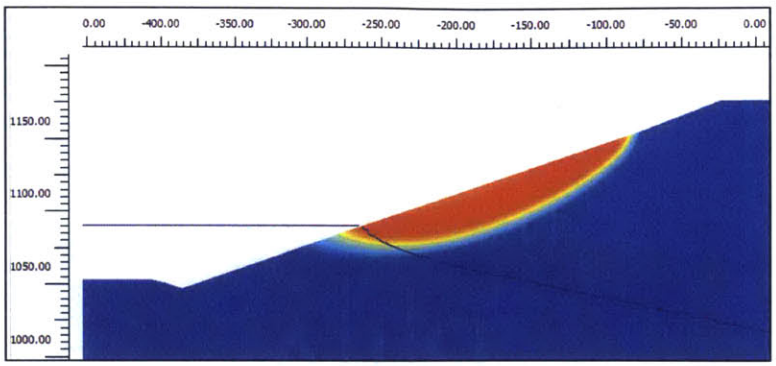

Figure C 25: Failure mechanism for 60 ft drawdown, 3 days.

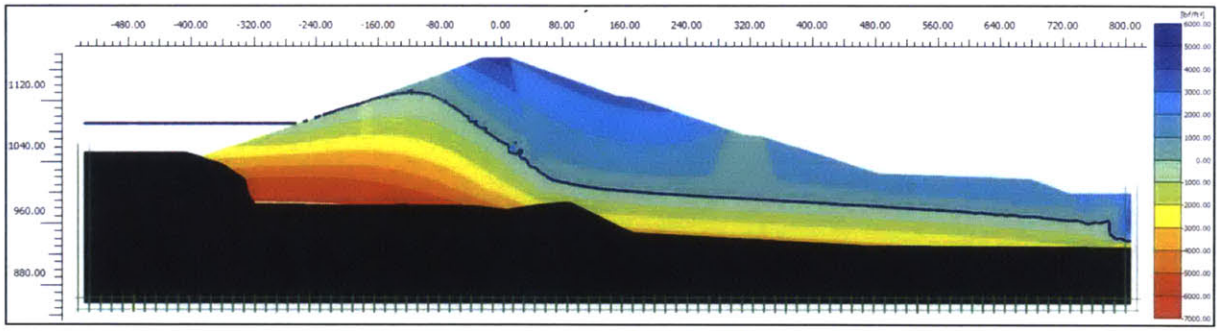

Figure C 26: Active pore pressure distribution for 60 ft drawdown, 3 days.

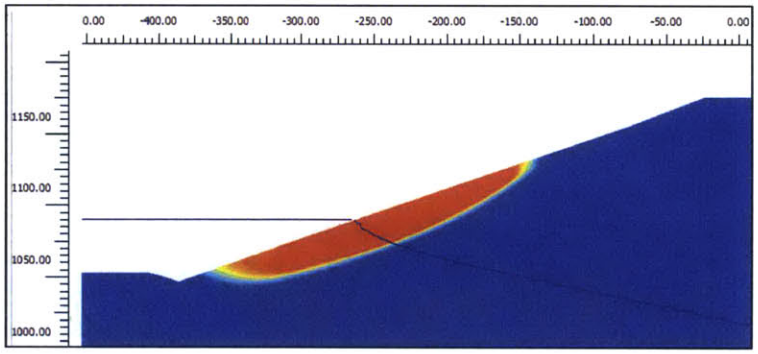

Figure C 27: Failure mechanism for 60 ft drawdown, 0.1 days.

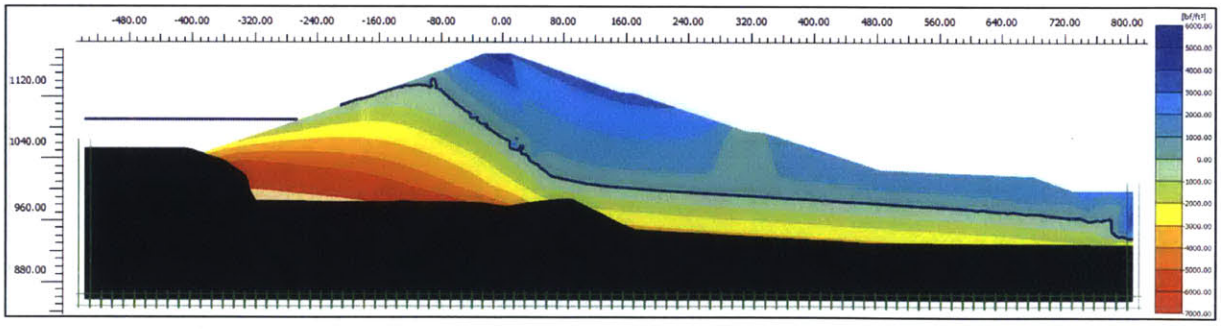

Figure C 28: Active pore pressure distribution for 60 ft drawdown, 0.1 days.

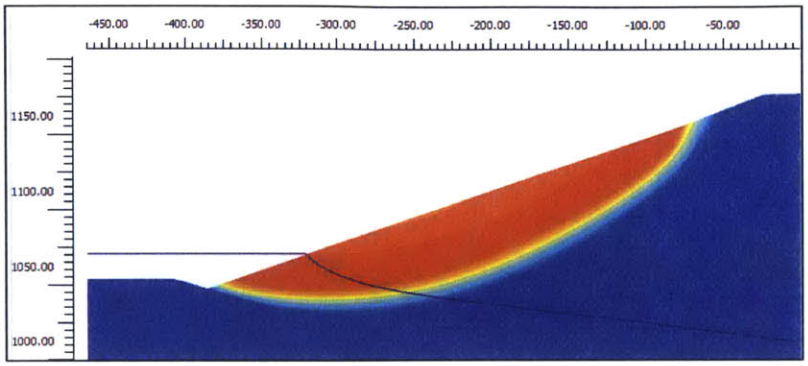

Figure C 29: Failure mechanism for 80 ft drawdown, 365 days.

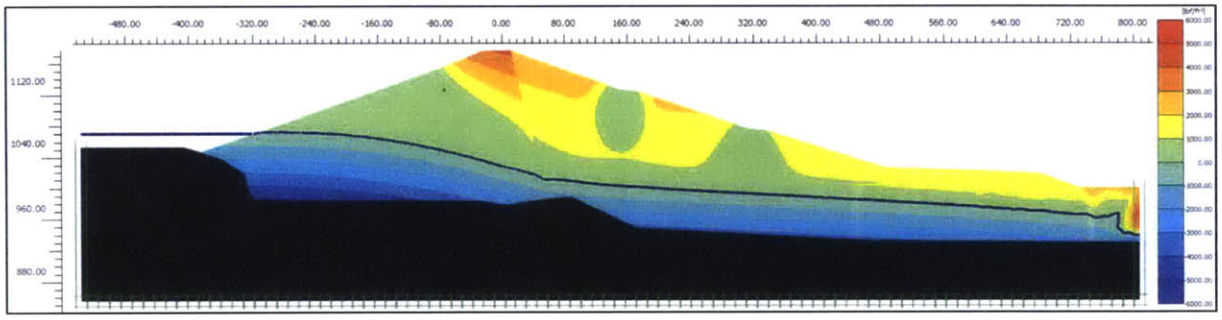

Figure C 30: Active pore pressure distribution for 80 ft drawdown, 365 days.

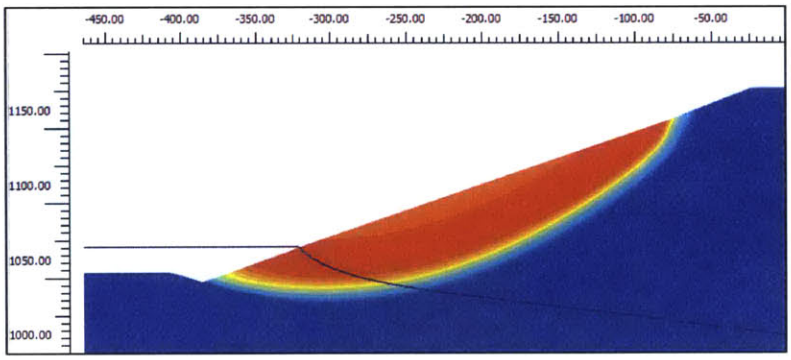

Figure C 31: Failure mechanism for 80 ft drawdown, 180 days.

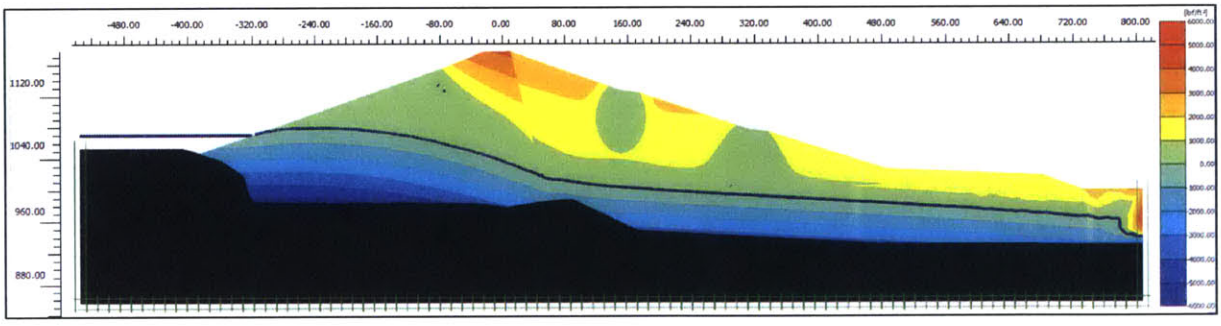

Figure C 32: Active pore pressure distribution for 80 ft drawdown, 180 days.

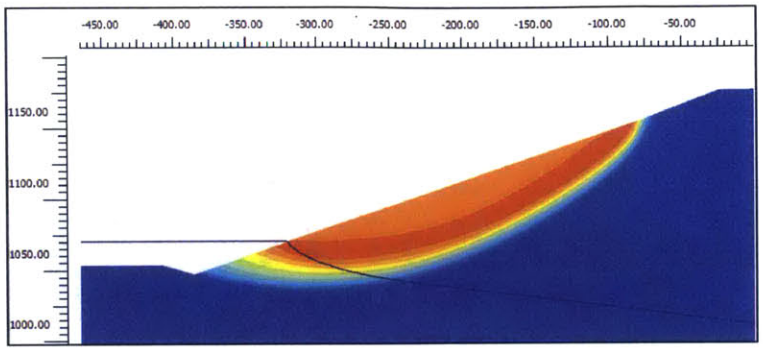

Figure C 33: Failure mechanism for 80 ft drawdown, 90 days.

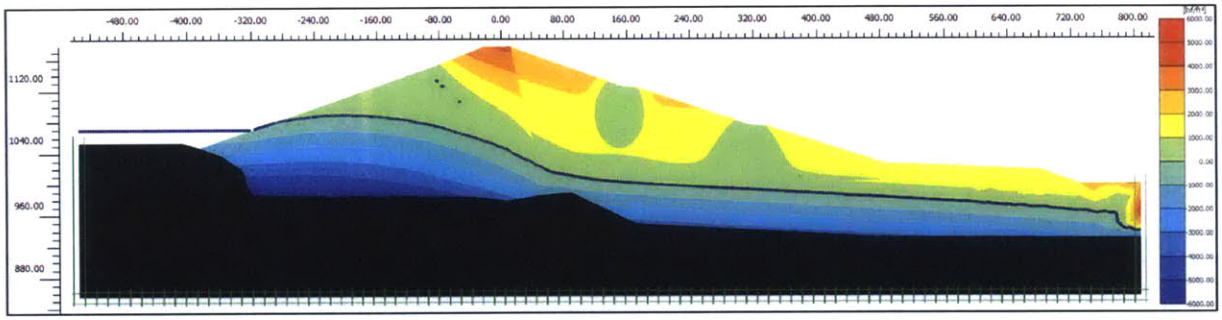

Figure C 34: Active pore pressure distribution for 80 ft drawdown, 90 days.

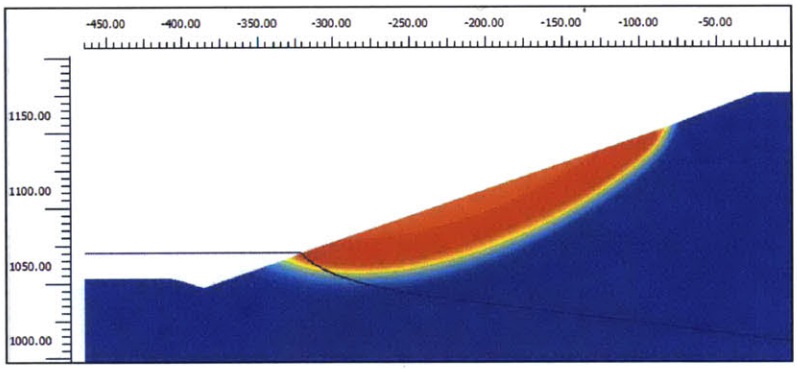

Figure C 35: Failure mechanism for 80 ft drawdown, 30 days.

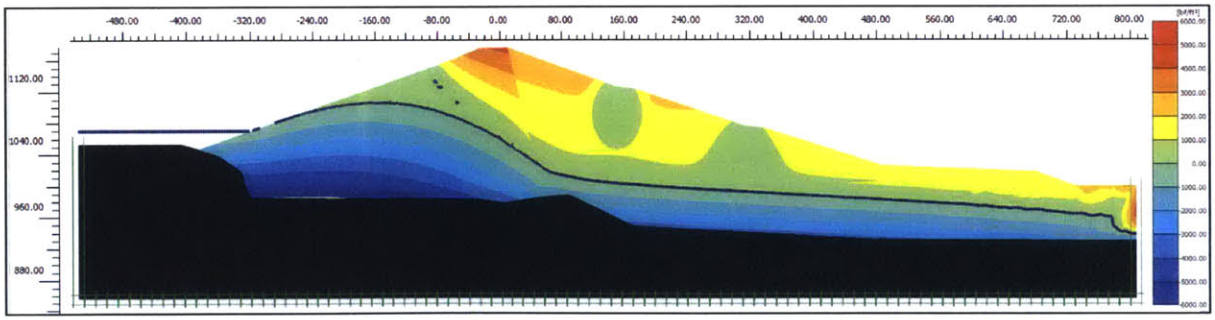

Figure C 36: Active pore pressure distribution for 80 ft drawdown, 30 days.

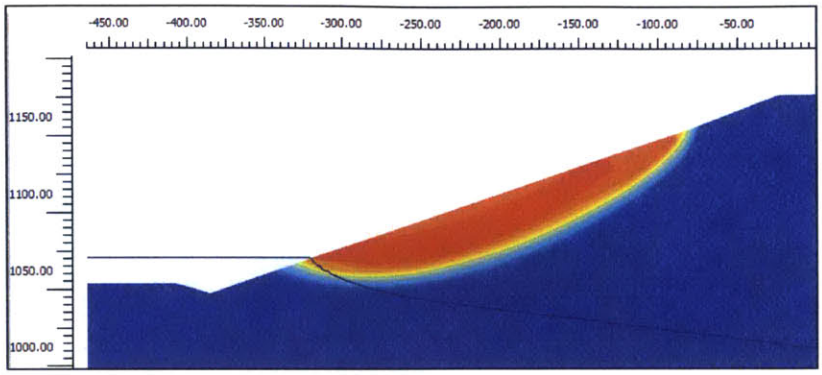

Figure C 37: Failure mechanism for 80 ft drawdown, 10 days.

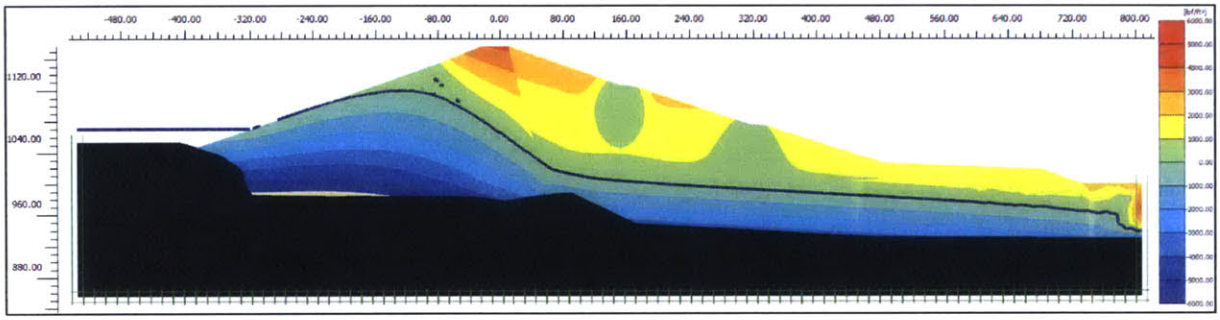

Figure C 38: Active pore pressure distribution for 80 ft drawdown, 10 days.

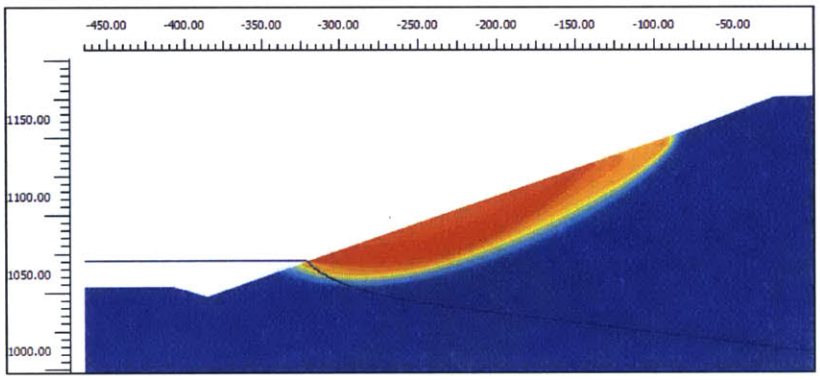

Figure C 39: Failure mechanism for 80 ft drawdown, 3 days.

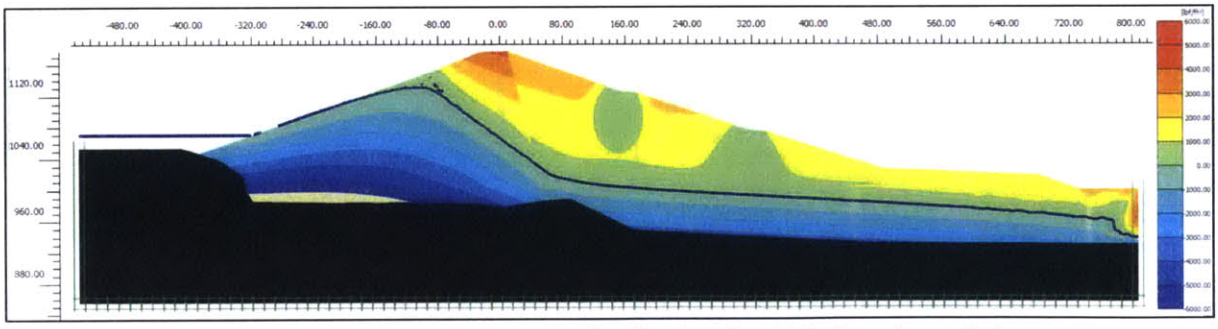

Figure C 40: Active pore pressure distribution for 80 ft drawdown, 3 days.

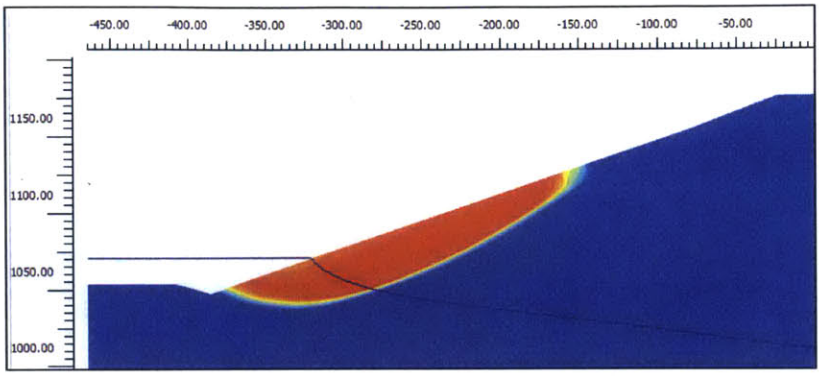

Figure C 41: Failure mechanism for 80 ft drawdown, 0.1 days.

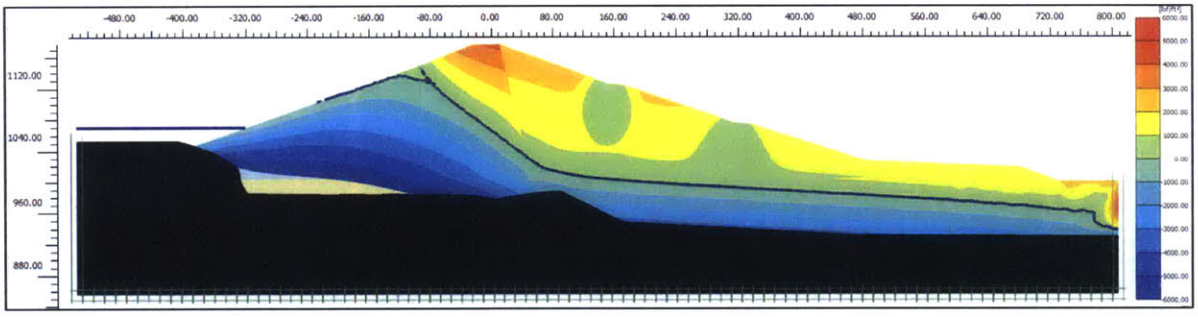

Figure C 42: Active pore pressure distribution for 80 ft drawdown, 0.1 days.

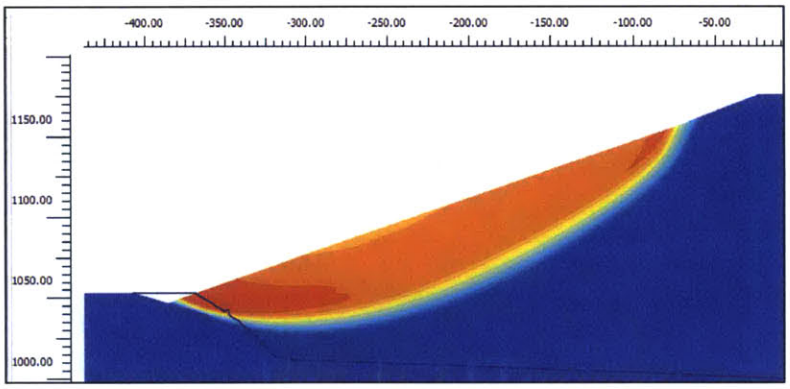

Figure C 43: Failure mechanism for 97 ft drawdown, 365 days.

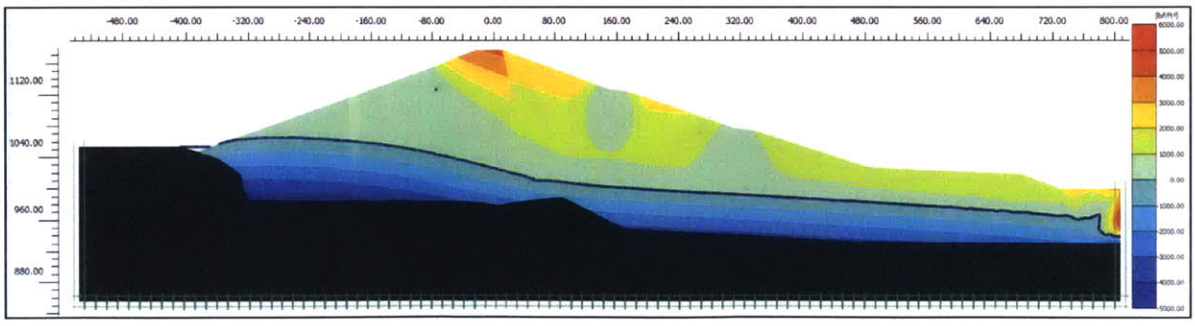

Figure C 44: Active pore pressure distribution for 97 ft drawdown, 365 days.

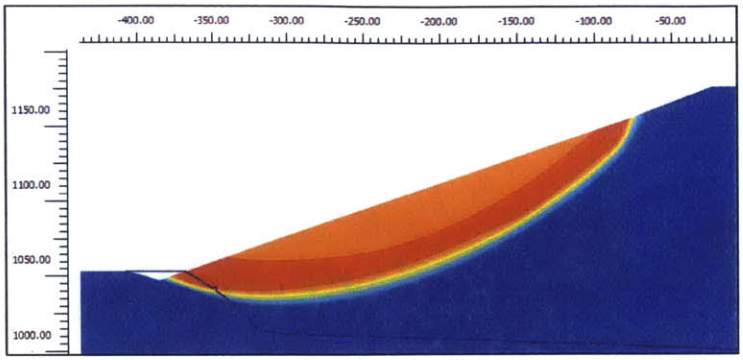

Figure C 45: Failure mechanism for 97 ft drawdown, 180 days.

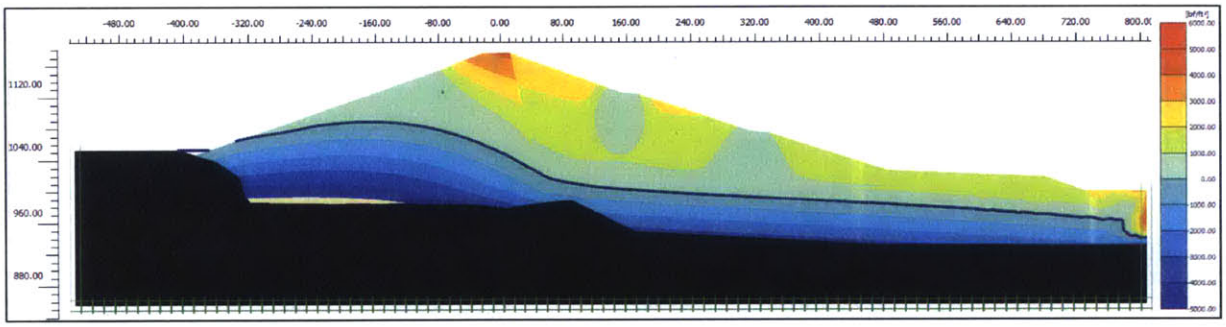

Figure C 46: Active pore pressure distribution for 97 ft drawdown, 180 days.

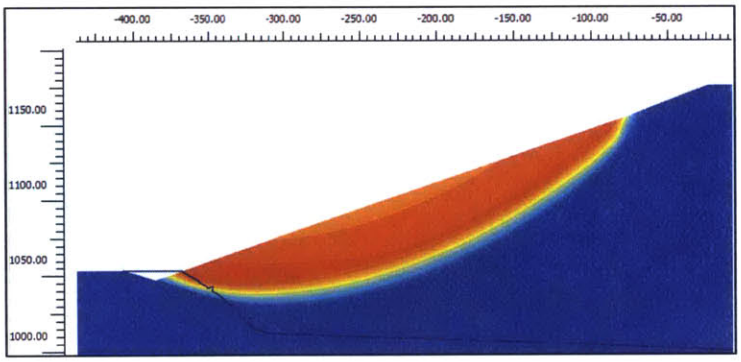

Figure C 47: Failure mechanism for 97 ft drawdown, 90 days.

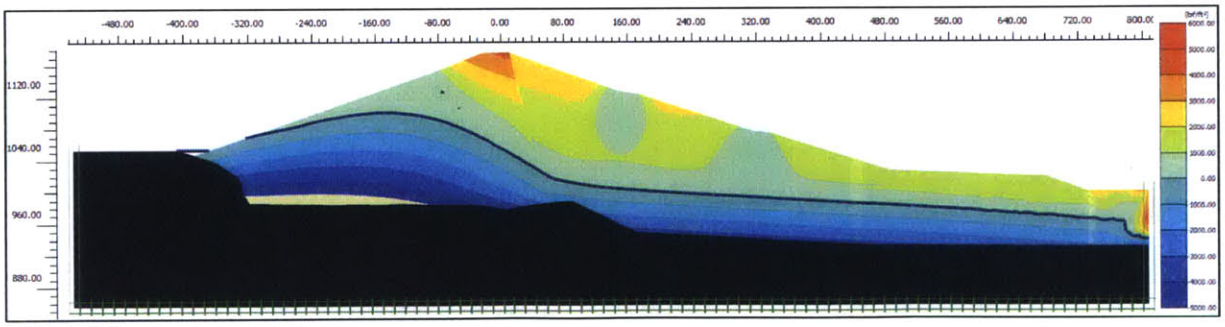

Figure C 48: Active pore pressure distribution for 97 ft drawdown, 90 days.

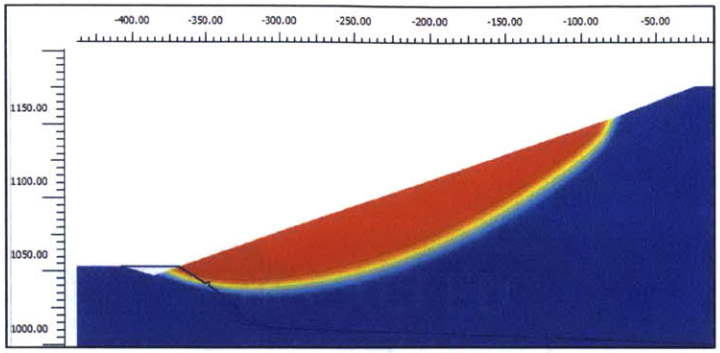

Figure C 49: Failure mechanism for 97 ft drawdown, 30 days.

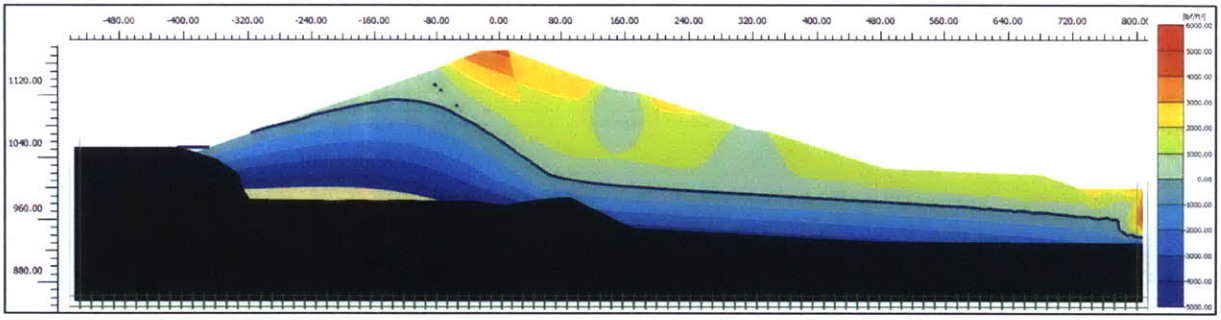

Figure C 50: Active pore pressure distribution for 97 ft drawdown, 30 days.

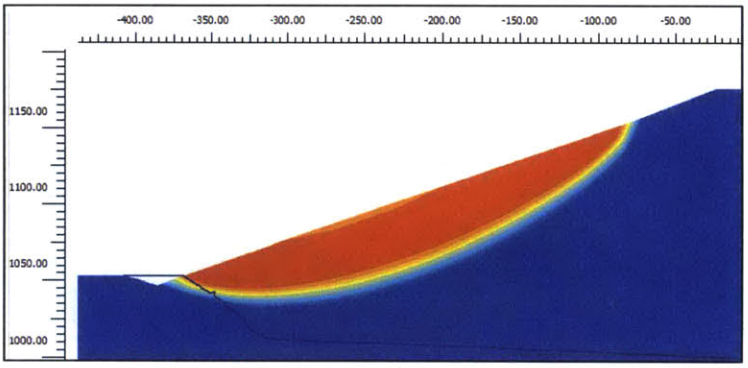

Figure C 51: Failure mechanism for 97 ft drawdown, 10 days.

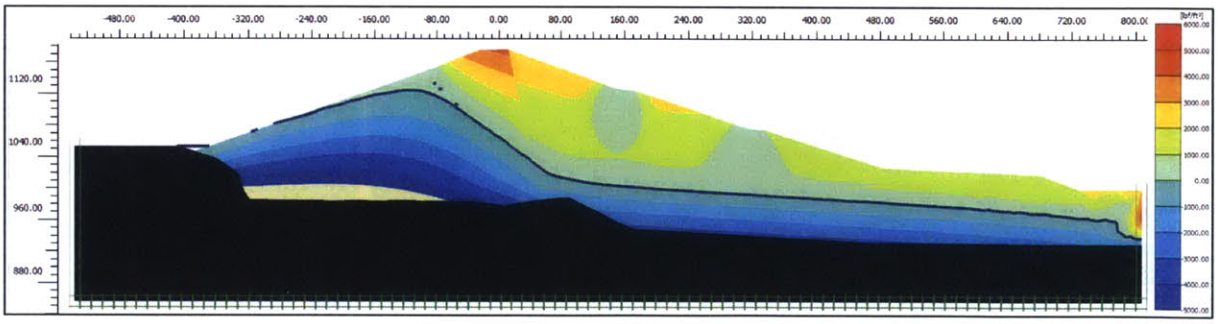

Figure C 52: Active pore pressure distribution for 97 ft drawdown, 10 days.

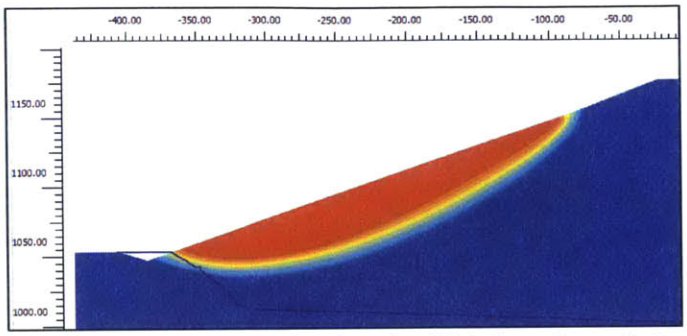

Figure C 53: Failure mechanism for 97 ft drawdown, 3 days.

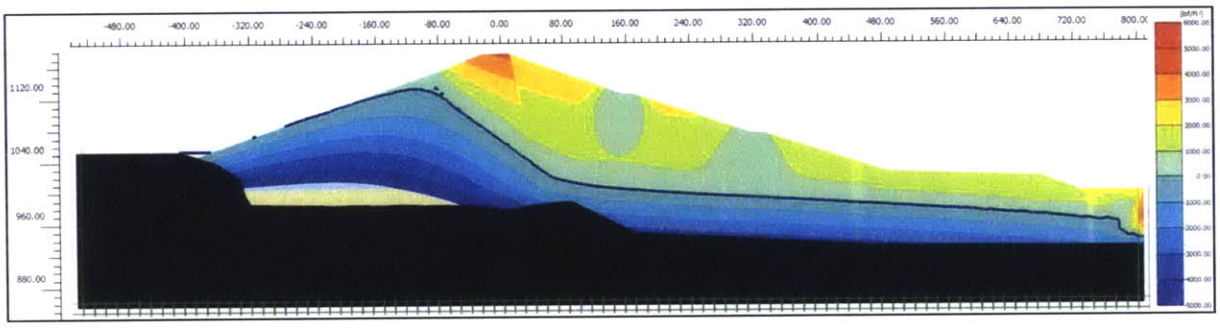

Figure C 54: Active pore pressure distribution for 97 ft drawdown, 3 days.

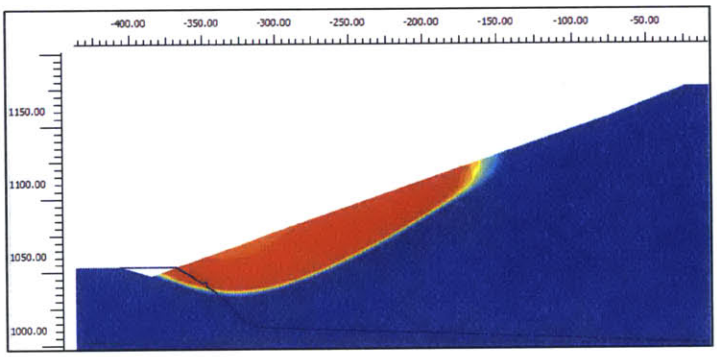

Figure C 55: Failure mechanism for 97 ft drawdown, 0.1 days.

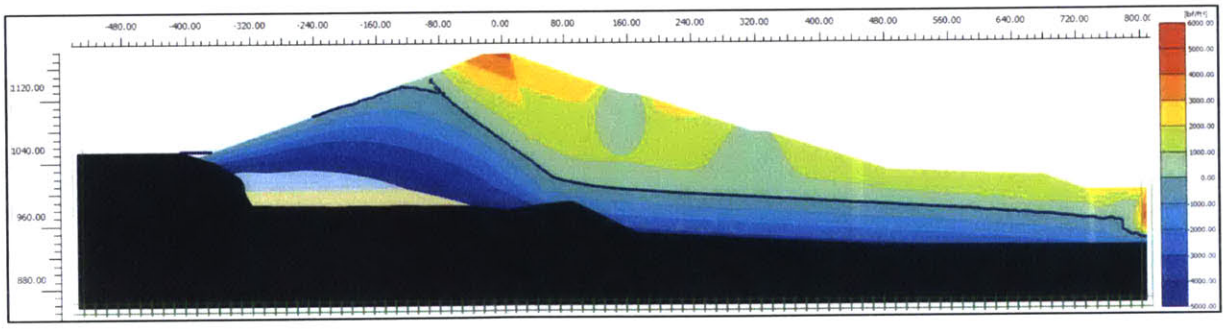

Figure C 56: Active pore pressure distribution for 97 ft drawdown, 0.1 days.